

SPIN-PHOTON ENTANGLEMENT AND QUANTUM OPTICS WITH
SINGLE QUANTUM DOTS

by

John R. Schaibley

A dissertation submitted in partial fulfillment
of the requirements for the degree of
Doctor of Philosophy
(Physics)
in The University of Michigan
2013

Doctoral Committee:

Professor Duncan G. Steel, Chair
Professor Paul R. Berman
Assistant Professor Hui Deng
Professor Theodore B. Norris

© John R. Schaibley 2013
All Rights Reserved

To my wife, Valerie

ACKNOWLEDGEMENTS

This work would not have been possible without the support of my colleagues, friends and family. First of all, I would like to thank my advisor, Professor Duncan Steel. I am very grateful for the opportunities he provided me, and without his guidance, I would not be here today. He is an advisor who always puts education and learning first, and for the rest of my career, I will remember this philosophy towards scientific research and mentoring.

I would like to thank Professors Paul Berman, Hui Deng and Ted Norris for serving on my committee. I am especially grateful for the theoretical mentorship that Professor Paul Berman has given me throughout my graduate career. His insight into atomic ensembles led to the theoretical detector model of Chapter 7, which gives theoretical justification to the experimental methods used to demonstrate a spin-photon entangled state. Professor Luming Duan has been a tremendous source of inspiration throughout my graduate career by motivating the spin-photon entanglement experiments and many of the future directions. In addition to my faculty mentors at Michigan, I have had the opportunity to work with several excellent scientists from other institutions. Professor Lu Sham has been an excellent theoretical collaborator, and a great source of help. In addition, I would like to thank Dr. Dan Gammon and Dr. Allan Bracker for providing the single quantum dot samples used in this work and for many useful discussions about quantum dot physics throughout the years.

I also would like to thank my graduate student mentors: Dr. Erik Kim, Dr. Katherine Truex, Dr. Xiaodong Xu and Dr. Bo Sun. When I was a young graduate student, they always answered my questions. Erik, Katherine and Bo were especially

helpful in teaching me many of the laboratory techniques that I used in this work, and passing on a solid theoretical understanding of the charged quantum dot system. I also have to acknowledge all the advice that I have received from Dr. Leon Webster, Dr. Vasudev Lal and Colin Chow throughout the years which has been very helpful to my work.

In addition, I have had the pleasure to mentor outstanding students during my graduate career. First off, I have to thank Alex Burgers for all of his hard work and dedication. He has been a real partner in many ways, staying up all night in the lab, and struggling through many of the challenges of my experiments with me. His attention to detail and patience for optimization has always impressed me, and I cannot thank him enough for all the help he has given me. I also had the opportunity to mentor Greg McCracken while he was undergraduate. Greg was a phenomenal undergraduate student, who wrote most of the computer code to analyze the time correlated single photon counting data, and was a critical member of our team. I would also like to thank all of the young students in the group: Cameron, Victoria, Uttam, Christine, Adam, Aaron, Wei, Midhat and Lu for all the lunches and discussions over the past months that have provided nice breaks from writing and kept me up to speed on the laboratory.

My family and friends have been a great source of support. I could not have done this without my wife, Valerie, who would always listen to my problems, and had a great ability cheer me up with her kindness and sense of humor. My parents, grandmother and sister have also been tremendous sources of support, who have strongly encouraged me to pursue my passions, and are always there for me when I need them. My colleague Mike Sloatsky, who started the physics program with me, has given me lots of advice throughout the years which was very helpful in my research, and has been a great companion outside of work. I would also like to thank Orestis, Xiaoran, David, Rachel, Jason, Adam, Jill, and Kaanan for all their support and friendship.

TABLE OF CONTENTS

DEDICATION	ii
ACKNOWLEDGEMENTS	iii
LIST OF FIGURES	vii
CHAPTER	
1. Optically Driven Quantum Dots for Quantum Information Applications	1
1.1 Brief History of Quantum Information Processing	1
1.1.1 Trapped Ion-Photon Interfaces	2
1.2 Optically Driven Quantum Dots	4
1.3 Scaling the Optically Driven Quantum Dot Spin Architecture	6
1.3.1 Coupling Quantum Dots with Local Interactions	7
1.3.2 Flying Qubits: Photons	8
1.4 Chapter Summary	10
2. Optical and Electronic Properties of InAs Quantum Dots	11
2.1 Review of Semiconductor Band Structure	11
2.2 Excitons in Bulk	16
2.3 Excitons in QDs	17
2.4 InAs Quantum Dot Structure and Characterization	20
2.5 Optical Transitions in Negatively charged QDs	24
2.6 Chapter 2 Summary	29
3. Fluorescence from Single Quantum Dots	30
3.1 Resonantly Driven Two-Level QD System	30
3.2 Experimental Setup and Results	32
3.3 Chapter 3 Summary	43
4. Time-Domain Measurement Techniques	44
4.1 Time-Correlated Single Photon Counting	44
4.2 Generating Fast Optical Pulses with Electro-Optic Modulators	51

4.3	Chapter Summary	63
5.	Transient Measurements and Quantum Optics with a Resonantly Driven Quantum Dot	64
5.1	Trion State Lifetime and Power Dependent Excitation	64
5.2	Time Dependent Rabi Oscillations	72
5.3	Photon Antibunching	77
5.3.1	Experimental results	85
5.4	Chapter Summary	89
6.	An Optically Driven QD Spin	90
6.1	Selection Rules with Magnetic Field in the Voigt Geometry	90
6.2	Spectroscopy on the Four-Level QD System	95
6.2.1	Steady-State Spectroscopy and Optical Pumping	96
6.3	Picosecond Qubit Rotations- Spin Rabi	100
6.3.1	Spin Rotation Experiments	106
6.4	Chapter Summary	111
7.	Spin-Photon Entanglement	113
7.1	A Quantum Dot Spin-Photon Entangled State	113
7.2	Theory of Frequency-Mismatched Spontaneous Emission	118
7.3	Spin-Photon Entanglement Experiment	124
7.3.1	Computational Basis Experiments	128
7.3.2	Rotated Basis Correlation	135
7.3.3	Spin-Photon Entanglement Results	137
7.4	Chapter Summary	140
8.	Conclusions and Future Directions	141
8.1	Results Summary	141
8.2	Applications of a Spin-Photon Entangled State	142
8.2.1	Quantum Teleportation: Three Qubit System	142
8.2.2	Spin-Spin Entanglement	145
8.3	Chapter Summary	149
	BIBLIOGRAPHY	151

LIST OF FIGURES

Figure

1.1	Distant entanglement between two ions can be heralded by coincident clicks on a detectors in an H.O.M. interferometer. The protocol requires intermediate ion-photon entanglement.	3
1.2	A single semiconductor QD can be charged with an electron. The spin of the electron can be used as a long lived quantum storage device which can be optically manipulated with coherent laser pulses through the QD's trion state. A single photon scattered by the QD can serve as a quantum communication link between QDs or provide a spin readout channel.	6
1.3	Two QD spins at different nodes of a quantum network can be coupled using intermediate spin-entangled photons.	8
1.4	When the $ T_x-\rangle$ state decays by spontaneous emission, the polarization state (H,V) of the single spontaneously emitted photon is entangled with the spin state ($ x+\rangle, x-\rangle$) of the QD. This type of entanglement can be used in a two QD protocol, as shown in Figure 1.1 for trapped ions, to herald entanglement between distant QDs.	9
2.1	A simplified direct bandgap semiconductor band structure showing the conduction band (CB), heavy hole (HH) band, light hole (LH) band, and split off (SO) band. For an intrinsic semiconductor, the Fermi energy is centered between the lowest conduction band and highest valence band. In bulk the HH and LH bands are degenerate at $k = 0$, however in a QD. Due to spin-orbit coupling, the SO band is energetically distant and is usually not considered while studying the HH and LH.	15
2.2	InAs islands form on top of a highly strained InAs wetting layer which grows on a GaAs substrate. After performing the indium flush technique the islands are capped with GaAs, forming the QD.	18
2.3	The sample structure showing the Schottky diode and GaAs heterostructure. The InAs QDs are located between two layers of intrinsic GaAs. The $n(\text{Si})$ -doped substrate provides electrons that can tunnel into the QD. An external bias voltage (V) is applied to deterministically charge the QD. A high numerical aperture (NA) aspheric lens is used to optically address single QDs.	21
2.4	A typical QD photoluminescence spectrum at 4 K. Here, a few QDs are excited by the laser spot, contributing multiple emission lines. . .	22

2.5	A bias dependent photoluminescence map showing the charging pattern of a single QD. The 6 meV jump in emission energy from the neutral exciton to the trion state is helpful in identifying the charge state. The X^{2-} state is also labeled. The other lines present on the PL map are from neighboring QDs that are also excited by the laser spot.	23
2.6	The four z -basis eigenstates of a negatively charged InAs. The ground states consist of a full valence band (VB) and single electron in the conduction band (CB) energy level. The lowest excited states consist of a singlet electron pair in the conduction band energy level and a heavy hole in the valence band.	26
2.7	Energy level diagram of the z -basis eigenstates of a negatively charged QD. It is composed of two degenerate two-level systems with selection rules that allow for excitation with circularly polarized light. The cross transitions (red) are not allowed.	28
3.1	The energy level diagram for a negatively charged InAs QD, composed of two degenerate two-level systems. $\sigma+$ ($\sigma-$) polarized light drives the transitions, so horizontally polarized light can be used to simultaneously couple to both of the transitions, while the vertically polarized QD photons can be directly detected.	33
3.2	Schematic diagram of the direct detection setup. The polarization of the excitation laser is set with a polarizer and Babinet-Soleil compensator. The laser is passed through a 1 : 1 compensation telescope before it is focussed onto the sample by a 0.68 NA aspheric lens. Light is collected with another 0.68 NA lens in the transmission geometry and passed through another 1 : 1 compensation telescope. The excitation laser is blocked with a polarizer set orthogonal to the transmitted beam. The QD fluorescence is focussed into a single mode fiber and detected with a single photon detector.	35
3.3	An example of a typical (distorted) VM absorption spectrum on a single trion in an apertured sample. Here large modulation is used so the signal should be modeled as a Lorentzian. The line shape distortion is believed to arise from reflections in the sample which mix the real and imaginary parts of the QD's optical response.	37
3.4	An example of a typical voltage modulation absorption spectrum on a single trion in an aperture-free sample. Large modulation is used so the line shape should be a Lorentzian. The solid line is a fit to a single Lorentzian with a line width of 450 MHz.	38
3.5	The lens/sample mount. Precision dowel rods keep the lenses aligned in two dimensions. 0-80 set screws are used to adjust the focus of the lenses.	39
3.6	An example of a Maltese cross pattern formed by a cross polarization setup and a high NA objective. Photo courtesy of Jieun Lee.	40

3.7	An example of a QD fluorescence intensity spectrum of a single trion state measured with the MPD-PDF detector. The solid line is a fit to a Lorentzian with a power-broadened line width of 611 MHz.	42
4.1	A typical TCSPC showing: a pulsed laser, a QD sample, a (SPAD) single photon detector and the timing electronics. In a traditional (TAC based) TCSPC setup, the signal from the SPAD starts the clock, and sync signal of a fast photodiode measuring the excitation laser pulses stops the clock.	46
4.2	Instrument response functions from the fast “PDF” detector (black) and high detection efficiency “ τ -SPAD” detector (red) measured with a TCSPC setup similar to Figure 4.1 by leaking some of the excitation laser onto the detector. The widths (FWHM) shown here are approximately 45 ps and 450 ps respectively. The detector “tails” arise from carriers created in the low field region of the detector.	48
4.3	Instead of a traditional TAC, the HH400 uses independent time-to-digital converters on both the signal and sync and records the event times relative to an internal clock. These times can then be subtracted digitally to perform a traditional start-stop TCSPC measurement.	50
4.4	(a) A simplified diagram of a waveguide LiNbO ₃ EOM. Light is coupled into the device with a PM fiber. The black lines with arrows show the optical path through the monolithic LiNbO ₃ structure. The light is split with a Y-junction into two paths. By applying an external voltage the phase imparted to the optical field in one arm can be varied relative to the other. The light in two paths is recombined, filtered with a polarizer and coupled out to another PM fiber. The dashed line shows the RF strip line that couples the traveling wave voltage through the device in the same direction as the propagating optical field. The simplified device depicted here is similar to a z-cut design, where the RF voltage mostly drives one arm (lower). In an x-cut device, the RF is coupled down the center of the device and drives the two arms anti-symmetrically.(b) A photograph of a z-cut EOM used in this work, showing the PM fibers, the RF input and DC bias pins. The device is about the size of a pencil.	53
4.5	An example of the measured output power of the x-cut EOM as a function of applied DC voltage. The output varies sinusoidally as expected. The π voltage is shown, where here $V_\pi \approx 3$ V. For pulsed operation, the EOM is locked to a minimum before pulses are applied to the RF input.	56
4.6	Examples of fast electronic pulses used to modulate the EOMs, showing three different pulse widths. The pulses are measured with an Agilent 86100a wide bandwidth oscilloscope.	58
4.7	The SPAD and TCSPC setup are used to measure the EOM generated pulses and maximize the EOM pulse output contrast. The pulses are attenuated so that the average count rate of the detector is $\approx 10^5$	60

4.8	Examples of EOM generated pulses showing three different pulse widths. The observed increased background for longer pulses comes from detector afterpulsing as explained in the text.	61
4.9	Calculated frequency chirps for 4 ns Gaussian pulse (red), and a 4 ns square pulse with 100 ps rise/fall time (blue). Since the chirp is proportional to the derivative of the voltage pulse, the chirp is most pronounced at the rise and fall of the square pulse.	62
5.1	The TCSPC setup used to perform transient measurements on the charged QD under pulsed excitation. Optical pulses are generated by an EOM which temporally gates a cw laser. Light from the QD is detected by a fast SPAD, and events are recorded using the HH400 picosecond event timer operating in integration mode. The excitation pulses are rejected using the cross polarization-fiber setup described in Chapter 3.	66
5.2	Time resolved QD emission under 250 ps pulse excitation with an integration time of 2 minutes. The black shows the signal when the QD is tuned onto resonance with the laser pulse using the DC-Stark effect. The red is the background level when the QD is tuned off resonance, showing the residual excitation pulse leaking onto the detector around 4.1 ns.	69
5.3	The QD emission (blue) following the 250 ps excitation pulse is fit with a single exponential decay function (red) to obtain a trion lifetime of $1/\gamma_2 = 640 \pm 25$ ps.	70
5.4	Transient fluorescence under 250 ps excitation for six different excitation powers. The onset of power dependent Rabi oscillations shows the nonlinear optical response of the QD. The inset shows the signal amplitude as a function of the square root of the power. The signal amplitudes are measured for nine different powers by integrating the fluorescence counts from 1 ns to 3 ns, after the excitation pulse has passed.	71
5.5	Normalized QD fluorescence under resonant 2 ns square pulse excitation is shown in red. The black trace shows the excitation pulse measured by the TCSPC setup leaking a small amount of the excitation pulse onto the detector. In both cases, the raw data are plotted so they are convolved with the SPAD's instrument response function.	73
5.6	The raw data (red) is deconvolved with the setup's instrument response function to give the deconvolved signal (blue). The high frequency oscillations present in the deconvolved data are an artifact from the deconvolution.	74
5.7	Time-dependent Rabi oscillations for four different excitation powers, plotted with the convolved fits of Equation 5.14 in red. P_0 corresponds to a peak power of approximately $3.4 \mu\text{W}$	75

5.8	Black: The Rabi frequency scales linearly with the square root of the excitation power as expected. Grey: The decoherence rate is also plotted against the square root of the excitation power, showing no sign of excitation induced dephasing. The grey bar shows the ideal case of $\gamma = \frac{1}{2}\gamma_2$ calculated from the $1/\gamma_2 = 640 \pm 25$ ps, where the thickness of the bar shows the error.	76
5.9	The cw QD fluorescence intensity as a function of the QD-laser detuning in the low power limit. The Lorentzian fit to the data gives a linewidth of 623 ± 25 MHz FWHM.	77
5.10	The HBT setup used to perform photon antibunching experiments on a single charged QD. A narrow bandwidth cw laser drives the charged QD. The QD resonance fluorescence is collected and sent to a 50-50 fiber beam splitter. τ -SPAD single photon detectors measure the light on the two outputs. The detection events are recorded with the HH400 picosecond event timer operating in “T2” mode.	82
5.11	A two-sided IRF shows the temporal response in a second order intensity correlation measurement. It is constructed by convolving a time reversed IRF from one detector with a forward time IRF from the other and symmetrizing the result. The resulting IRF width 630 ps FWHM.	86
5.12	Blue: Second order intensity correlation function for QD resonance fluorescence under cw excitation showing a clear antibunching dip at zero time delay. Green: Theoretical prediction from Equation 5.45 using the QD parameters measured in pulsed measurement. Red: The theoretical prediction (green curve) is convolved with the two-sided IRF (Figure 5.11) to show the expected signal. The blue line at 0.5 shows the single photon limit, and since the $g^{(2)}$ signal is below 0.5 at time zero, the QD is a single photon source.	88
6.1	Energy level diagram for the charged QD with an external magnetic field applied perpendicular to the growth geometry (Voigt direction), forming a four-level system. The ground states form the spin qubit and are split by the Zeeman frequency (Δ_e). The optically excited trion states are at a frequency, ω_0 , above the ground states which corresponds to a wavelength of approximately 950 nm for the QDs studied in this work. The trion states are split by the hole Zeeman frequency (Δ_h). The transitions are coupling with horizontally (H) and vertically (V) polarized light, where the i is a reminder of the relative phase between matrix elements.	92
6.2	Selection rules of a charged QD with a magnetic field applied in the Voigt geometry. The inner (outer) transitions are driven by horizontally- H (vertically- V) polarized light which are orthogonal, although the absolute orientation of these transitions can vary due to heavy-light hole mixing. When the laser is polarized at 45 degrees, all transitions can be excited.	94

6.3	Voltage modulation absorption of a charged QD in the co-tunneling region of the voltage existence range showing the absorption signal at zero field (blue) and the signal at 1.1 T (red) where the transitions are split by the magnetic field.	98
6.4	In the middle of the existence range, a single probe laser optically pumps the system so it becomes transparent (no absorption). A re-pumping laser can be added to recover the absorption by “frustrating” the optical pumping.	99
6.5	In the middle of the voltage existence range, the ground state is stable, and the four-level system undergoes optical pumping so it is transparent to a single probe laser beam (green). If the re-pumping beam is pumps one of the right transitions absorption	101
6.6	The electron spin can be optically manipulated by a step-wise two pulse sequence relying on intermediate trion population. Step-wise approaches generally exhibit lower fidelities due to fast decay in the excited state.	103
6.7	Energy level diagram depicting the two-photon resonance for a detuned stimulated Raman transition. The relevant frequencies are shown labeling the trion resonance (ω_0), the electron Zeeman frequency (Δ_e), the hole Zeeman frequency (Δ_h), and the laser detuning (δ).	104
6.8	Timing diagram for the spin-Rabi experiments. A 4 ns optical pumping pulse inializes the system to a pure state. A detuned 2 ps pulse driving the two-photon resonance rotates the spin state. The resulting spin population is read out by detecting a single scattered photon during the next 4 ns pulse.	107
6.9	(a) fluorescence histograms showing readout signal from the 4 ns pulse as a function of the applied rotation pulse power. The area under the curves in the “Readout” time region serves as a measure of the $ x+\rangle$ population. The noise around 2 ns comes primarily from imperfect background subtraction. (b) The integrated readout signals from data sets as shown in (a) are plotted versus the applied pulse power to observe power dependent spin-Rabi oscillations.	108
6.10	Timing diagram for a spin coherence measurement. The first $\pi/2$ pulse creates a superposition of x -basis states which undergos unitary evolution in time until the second pulse rotates the coherence into a x basis population that is read out by the 4 ns pulse. The time delay between the two $\pi/2$ -area pulses is varied to observe oscillations at the electron Zeeman frequency.	109
6.11	Two-pulse measurement using the pulse sequence of Figure 6.10 showing electron spin coherence. Oscillations are observed at the electron Zeeman frequency 7.35 GHz. The saw-tooth signal is believed to arise from the hyperfine interaction with the QD’s constituent nuclear ensemble. The author would like to acknowledge A. Burgers and U. Paudel for performing this measurement.	111

7.1	When the $ T_x-\rangle$ state decays, the spontaneously emitted photon is correlated with the resulting QD spin state.	114
7.2	Energy level diagram for the states involved in lambda system decay.	116
7.3	The spin-entangled photon is detected by a single photon detector, which we model as an ensemble of two-level detector atoms whose excited state rapidly decays to a avalanche or reservoir state of the detector. The source atom (QD) is taken to be at the origin, and the detector extends from x_0 to $x_0 + L_0$	118
7.4	Energy level diagram including the electron and hole Zeeman frequencies for the magnetic field used in this work. The electron Zeeman frequency is kept as small as possible, while keeping the hole/trion splitting large enough to use frequency selective excitation. The optical energy splitting is approximately 1.305 meV (10523.5cm^{-1}).	125
7.5	Fluorescence recorded as function of the excitation laser frequency showing the 7.35 GHz splitting between the two transitions of the right lambda system.	126
7.6	The experimental setup used in the spin-photon entanglement experiments. The QD is held in the magnetic optical cryostat at 7 K. Two cw lasers are modulated with EOMs to generate resonant 250 ps and 4 ns pulses. A mode-locked Ti:sapphire laser is used in the rotated basis measurements to rotate the spin state. The lasers are polarized before the cryostat with a combination of polarizer and quarter-wave plate. Light is collected in the transmission geometry. Another quarter-wave plate and polarizer are used to set the photon detection axis and to filter out the excitation lasers. In the rotated basis measurement, an etalon is used to further suppress the detuned pulses from the mode-locked laser. The QD light is split and sent to a pair of single photon detectors. Detection events are time-tagged with a picosecond event timer synchronized with the laser's repetition rate.	127
7.7	The spin is initialized with a 4 ns optical pumping pulse, and then excited with a 250 ps (π -area) pulse to the $ T_x-\rangle$ state which decays, emitting the spin-entangled photon. If an H photon is detected, the spin is projected to the $ x+\rangle$ state, so the probability of scattering a photon during the next 4 ns pulse (which now serves to readout the spin) is 1 . If no photon is detected, the probability of scattering a photon with the 4 ns readout pulse is 0.5	129
7.8	An example of a time-histogram of a typical computational basis measurement. The black (red) shows the signal (background) when the QD is tuned on (off) resonance with the DC Stark shift. The entangled photon is generated following the 250 ps (π -area) excitation pulse. Here, the readout photon is generated during the 4 ns pulse which re-initializes the system by optical pumping. The oscillations during the readout are Rabi oscillations at a frequency of $\approx 1\text{GHz}$	130

7.9	The conditional probabilities are normalized by comparing the number of entangled photon-readout photon correlations for the same shot of the experiment to the number of correlations for temporally distant (uncorrelated) shots of the experiment which correspond to a conditional probability of 0.5.	131
7.10	As an independent check, we perform a correlation measurement verifying that detection of an H photon is anti-correlated with measuring the spin in the $ x-\rangle$ state, by inserting an additional 250 ps spin readout pulse on V_2 that reads out the $ x-\rangle$ population after the photon is detected, but before the spin is re-initialized.	131
7.11	Anti-bunching for the excitation pulse and readout pulse showing a nonzero signal at time zero, arising from re-excitation due to off-resonant coupling of the pulses. This background is used to correct the raw spin-photon correlation data.	132
7.12	An example the raw and corrected computational basis correlation data which both show a clear positive correlation signal at time zero. The uncorrelated distant runs are used to normalized the conditional probabilities.	133
7.13	Normalized spin-photon correlation data for the $P(x+ H)$ and $P(x- H)$ measurements showing a correlation between detecting an H photon and measuring the spin in the $ x+\rangle$ state.	134
7.14	Normalized spin-photon correlation data for the $P(x+ V)$ and $P(x- V)$ measurements showing a correlation between detecting an V photon and measuring the spin in the $ x-\rangle$ state.	134
7.15	Timing diagram for the rotated basis measurements.	135
7.16	(a) Black: The theory (Equation 7.55 is convolved with the detector's instrument response function to show the form of the expected signal. Red: An exponential fit to the theoretical signal is used to normalize to a conditional probability. (b) Black: Theoretical signal after dividing out by the exponential fit. Red: A fit to the convolved normalized theory yields a fringe contrast of 0.4, which limits the maximum obtainable entanglement fidelity to 0.7.	137
7.17	(a) Black: Rotated basis correlation signal showing oscillations at the electron Zeeman frequency with an exponential envelope. Here the data are binned at 16 ps time bins and smoothed. The spike at 1.5 ns is the residual rotation pulse leak through which is not completely blocked by the rejection setup. Red: An exponential fit to the data is used to normalize the rotated basis conditional probabilities. (b) Black: after dividing out by the exponential envelope, we observe the coincidence signal whose fringe contrast is consistent with theoretical limit. Red: A sinusoidal fit is overlaid as a guide to the eye.	138

7.18	Black: Rotated basis correlation data used to extract the conditional probabilities. The raw data are time binned relative to the rotation pulse with 48 ps time bins and the exponential envelope is divided out. Red: The data are fit using the experimentally determined Zeeman frequency, 7.35 GHz. We fit to the first three periods where the signal to noise is the highest. The fringe contrasts are 0.40 ± 0.10 for $\sigma+$ and 0.38 ± 0.08 for $\sigma-$	139
7.19	Conditional probabilities for the computational (x) and rotated (z) basis measurements.	140
8.1	A single photon frequency qubit, generated by exciting a single neutral QD to a coherent superposition of its excited states, can be teleported to the QD spin state by measuring coincident detector clicks in a H.O.M. interferometer. The resulting spin state is then read out to verify that the state is transferred.	143
8.2	In a type-I protocol, the two QDs are weakly excited so that the probability of either being excited is much less than 1. If one detector registers a click, the QD spins are projected to an entangled state (Equation 8.7).	146
8.3	In a type-II protocol, both QDs are initialized to the $ T_x-\rangle$ state, which decay emitted two spin-entangled photons. Coincident detector clicks herald a spin-spin entangled state (Equation 8.8).	147
8.4	By moving to a QD molecule system a W system can be formed, which is composed of a central lambda system (red) and two cycling transitions (blue) which can provide a nondestructive readout the of spin populations. The kets label the spin configurations of the lower and upper QDs which form the molecule.	149

CHAPTER 1

Optically Driven Quantum Dots for Quantum Information Applications

In the last 20 years, the field of optically driven QDs has rapidly grown from the early stages of characterization to become one of the leading candidates for scalable quantum information applications. In this work, optically driven quantum dot (QD) spins are studied for quantum information applications. A single QD is charged with an electron whose spin state is used to encode quantum information. The QD spin can be coupled to photons through the QD's optically excited trion states [1, 2]. Photon states entangled with the QD spin can be used to mediate entanglement between QD spins providing the basis of a scalable quantum information architecture [3–5]. In this work, we apply quantum optics techniques to the study of QDs and demonstrate a QD spin-photon entangled state which is an important step towards realizing a scalable optically coupled QD spin architecture.

1.1 Brief History of Quantum Information Processing

Over the past few decades, there has been tremendous advancement in the ability to control individual quantum states. The invention of the laser and nonlinear optics in the 1960's led to rapid advances in optical science [6, 7]. Since then, the fields of atom trapping, quantum optics, and ultrafast optical science have evolved at a remarkable pace. These advancements led to the ability to trap and manipulate single atoms [8, 9]. Many attribute the field of quantum information processing to Richard Feynman, who explored the idea that a computer based on quantum mechanics could be more efficient than a classical computer [10]. Interest in quantum computing

was further motivated by the work of Deutsch [11] and the discovery of powerful quantum algorithms such as Grover’s search algorithm [12] and Shor’s factoring algorithm [13], which offer significant speedups over classical computing algorithms. The next theoretical breakthrough in quantum information science was the development of fault-tolerant quantum computing, showing that the computational errors, which are inherent in a real world quantum computer, could be controlled by implementing quantum error correction codes [14, 15]. In the 1990’s and 2000’s, experiments using trapped ions, nuclear spins in molecules, atomic gases, single photons, superconducting circuits, defect centers in crystals, and QDs demonstrated that a diverse range of material systems can be useful for quantum information applications [16]. A current goal in many of these systems is realizing a practical architecture suitable for scalable quantum information processing/computing [17], including using different physical systems to implement different parts of a hybrid quantum network [18].

1.1.1 Trapped Ion-Photon Interfaces

The charged QD system is a solid state analogue of a single trapped ion, so it is useful to review some of the recent results from the trapped ion community. In 1999, it was proposed that entanglement between distant ion qubits could be heralded using intermediate photon states [19]. In 2004, *Blinov et al* showed that the polarization state of a photon spontaneously emitted from a lambda system of a single trapped ion is entangled with the resulting hyperfine level [20]. In the following years, it was shown that two intermediate ion-photon entangled states can be used to herald entanglement between two distant ion qubits [5]. The approach relies on a probabilistic postselection protocol using Hong-Ou-Mandel interference [21,22], which utilizes interference between two indistinguishable photons. In the experiment, two ions are simultaneously excited, which then decay by spontaneous emission. The photon frequency is entangled with the hyperfine level so that,

$$|\psi_i\rangle = \frac{1}{\sqrt{2}}(|\uparrow\rangle_i|\omega_\uparrow\rangle_i - |\downarrow\rangle_i|\omega_\downarrow\rangle_i) \quad (1.1)$$

where $i = a, b$, as depicted in Figure 1.1.

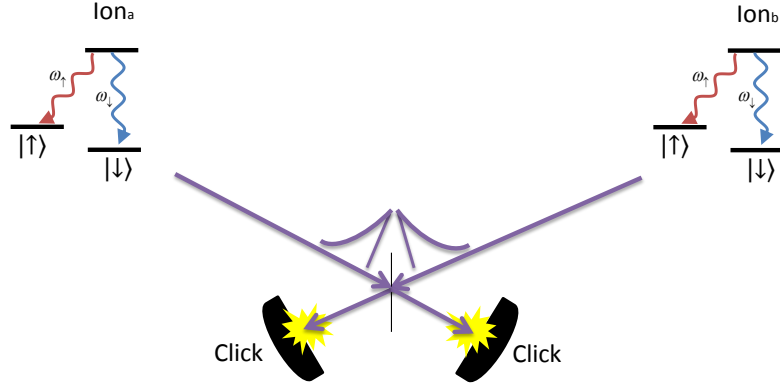


Figure 1.1: Distant entanglement between two ions can be heralded by coincident clicks on a detectors in an H.O.M. interferometer. The protocol requires intermediate ion-photon entanglement.

When these photons are mixed on a 50-50 beam splitter the resulting state is,

$$|\Psi_{a,b}\rangle = |\psi_a\rangle \otimes |\psi_b\rangle. \quad (1.2)$$

The two detectors simultaneously click only if the photons are in the antisymmetric state [22],

$$|\psi_{photon}\rangle = \frac{1}{\sqrt{2}}(|\omega_\uparrow\rangle_a |\omega_\downarrow\rangle_b - |\omega_\downarrow\rangle_a |\omega_\uparrow\rangle_b). \quad (1.3)$$

So that coincident detector clicks projects the state vector to $|\psi_{photon}\rangle$, which heralds an entangled state between the distant spins of the form [5],

$$\langle\psi_{photon}|\Psi_{a,b}\rangle = \frac{1}{\sqrt{2}}(|\uparrow\rangle_a |\downarrow\rangle_b - |\downarrow\rangle_a |\uparrow\rangle_b). \quad (1.4)$$

This heralded spin-spin entanglement is a useful resource for quantum information science since it provides a platform where the simplest quantum network (2 qubits) can be studied. The first step to achieving this distant spin-spin entanglement is verifying that the intermediate spin-photon state is entangled. Verifying that an InAs QD is capable of generating a spin-photon entangled state is the primary objective of this work.

1.2 Optically Driven Quantum Dots

Simultaneously with the invention of the laser in the 1960s, great advancement in semiconductor processing, such as molecular beam epitaxy (MBE) [23] and GaAs based optoelectronics led to new capabilities to control the quantum states of charge carriers in solids. Specifically, the realization of 2 dimensional quantum well, 1 dimensional quantum wire, and 0 dimensional QD structures allowed for tuning electronic states through confinement. The 0 dimensional QD is of particular interest for quantum information applications because its energy levels are discrete and can be used to encode quantum information.

There are two basic types of QDs: gate-defined QDs which are based on quantum well structures that use electronic gates to provide the in-plane confinement potential that can trap single carriers [24, 25], and semiconductor QDs which realize 3 dimensional electronic confinement through the QD's physical structure. Due to the relatively weak in-plane confinement in gate-defined QD, optical studies on QDs are usually limited to semiconductor QDs which we study here. Semiconductor QD systems generally fall into two categories: chemically synthesized colloidal (II-VI) QDs, and epitaxially grown (III-V) QDs usually based on GaAs heterostructure technology. In this work, we study single InAs/GaAs QDs, which are grown by molecular beam epitaxy. The QDs begin as nanometer sized islands of InAs which are formed by a self-assembly process while growing InAs on a GaAs substrate. These islands are then capped with GaAs to form the QD. Since the bandgap of GaAs is much larger than the bandgap of InAs, electrons and holes can be confined to the QD potential.

Due to this spatial confinement, it becomes possible to optically excite single excitons (electron-hole pairs) since the QD potential gives rise to an anharmonic energy level diagram. That is, since the size of the QD is smaller than the exciton Bohr radius, the energy to excite two excitons inside the QD is not twice the energy to excite one exciton. This anharmonic energy level spacing allows the QD to be thought of as a solid-state realization of single trapped atom. Early work in (GaAs) interface fluctuation QDs showed that this atomic like picture of a single QD exciton is valid [26]. In that system, Rabi oscillations, exciton-exciton entanglement, and 2 qubit

quantum gates were realized [27–29], showing that single QD excitons, manipulated by coherent optical laser pulses, are useful for quantum information science.

In 1998, Loss and DiVencenzo outlined a proposal using QDs for scalable quantum computing. In this proposal, they proposed using (electron) spins confined to QDs as quantum storage devices and outlined a list of criteria which must be realizable for a scalable quantum computing architecture, which are known as the *DiVencenzo Criteria* [24]. They are listed here in their original form in quotation along with a description of their meaning where appropriate:

1. “Identification of well-defined qubits”
2. “Reliable state preparation” -Ability to initialize the system to a pure state
3. “Low decoherence” -Coherence time much longer than the gate operation time
4. “Accurate quantum gate operations” -Universal set of quantum gates
5. “Strong quantum measurements” -Ability to read out specific qubit states

One of the primary challenges in any quantum information architecture is finding a physical system where the qubit can be manipulated and read out efficiently while simultaneously exhibiting long coherence times because it couples weakly to the environment. The exciton state of a single QD can be used to encode quantum information, however since the exciton is an excited state which radiatively decays in < 1 ns, they are short lived and have limited use in quantum information schemes, which require long coherence times relative to the gate operation time (typically 1 ps). By encoding the quantum information in the long lived spin state of a QD, one can realize a scalable qubit which exhibits “low decoherence” [24], relative to the gate operation time.

A single semiconductor QD can be charged with an electron to realize an optically coupled QD spin system as depicted in Figure 1.2. The charged QD system was studied in GaAs interface fluctuation QDs with some success [30], but due to the relatively weak in-plane confinement of carriers in GaAs QDs, it was determined that charged

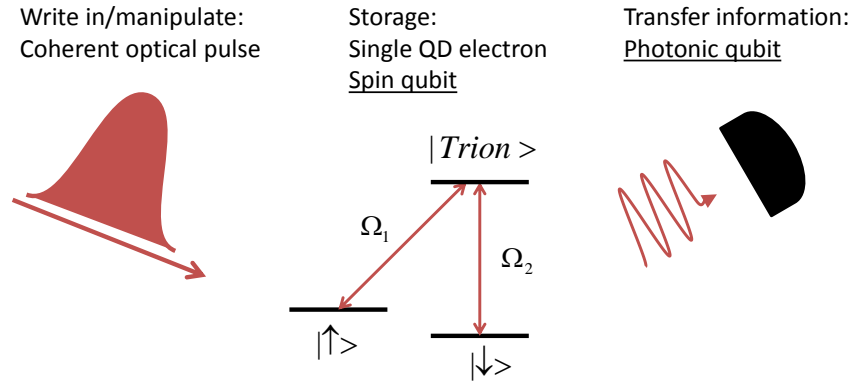


Figure 1.2: A single semiconductor QD can be charged with an electron. The spin of the electron can be used as a long lived quantum storage device which can be optically manipulated with coherent laser pulses through the QD’s trion state. A single photon scattered by the QD can serve as a quantum communication link between QDs or provide a spin readout channel.

self-assembled InAs/GaAs QDs are better candidates for quantum information applications [2, 31]. In the charged QD system, the ground state sublevels are composed of the two spin states of a single electron in the QD. The optically excited trion state of the QD is a negatively charged exciton: a three-particle system composed of two electrons and one hole. This forms a QD “lambda” system which can be thought of as the solid-state analogue of a single trapped ion, where the qubit is encoded in the long lived spin ground state, and the spin can be rapidly manipulated through the QD’s optically excited trion states. In the single charged QD system, all of the single qubit *DiVencenzo Criteria* have been realized [1, 2], and the current focus is on scaling the optically driven QD spin architecture to a multiple qubit system for practical quantum information applications.

1.3 Scaling the Optically Driven Quantum Dot Spin Architecture

A challenge in realizing a scalable architecture for quantum information applications is maintaining well defined single qubits that can be independently manipulated

and read out, while simultaneously mediating controlled interactions between qubits that allow for conditional gate operations, which are required to realize a universal set of quantum gates. In terms of quantum mechanics, these conditional gate operations generally require the ability to entangle specific qubits where the entanglement is used as a resource both for computation and error correction [16]. There are two leading approaches being explored for scaling the optically driven QD spin system: local interactions and flying (photon) qubits.

1.3.1 Coupling Quantum Dots with Local Interactions

Local interactions, (dipole-dipole, exchange, tunneling) between spatially adjacent QDs can be used to directly mediate interactions. However, controlling local interactions is challenging because self-assembled QDs usually nucleate randomly on the sample, where only the average areal density of QDs is tunable. Recently, there have been promising advances in realizing site-controlled QD growth by using electron beam or focussed ion beam techniques to deterministically induce a QD nucleation site by patterning the substrate before the QDs are grown [32, 33]. Although there has been tremendous progress in controlling QD nucleation sites, so far site-controlled QDs have exhibited significantly degraded optical properties compared to traditionally grown QDs, likely due to unstable trapped states associated with the patterning.

Another exciting approach relies on vertically stacking QDs to form “QD molecules” [34]. In this approach, after an InAs QD is capped with a GaAs layer, another layer of InAs is grown. The presence of the bottom QD induces a strain in the top layer which causes a second QD to preferentially nucleate above the bottom dot. The QDs are sufficiently close together that there can be significant wavefunction overlap between the electron and hole wavefunctions under certain conditions, which give rise to a “tunneling interaction.” By utilizing the tunneling interaction, conditional operations between spin qubits of distinct QDs is possible. Recently, entanglement between two electron spins confined to two QDs of a QD molecule has been demonstrated using the tunneling interaction, which is an important step towards a scalable

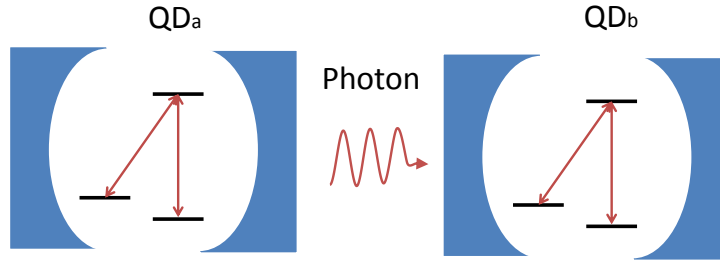


Figure 1.3: Two QD spins at different nodes of a quantum network can be coupled using intermediate spin-entangled photons.

QD spin system [35].

1.3.2 Flying Qubits: Photons

We pursue a scaling approach that relies on intermediate flying photonic qubits. The QD spin can be coupled to photons using the QD’s optically excited trion states, and since single photons are also capable as serving as qubits, they can be used to link spatially distant QD spins (Figure 1.3), where intermediate spin-photon entangled states could be used to mediate entanglement between distant QD spins.

In principle, a single photon scattered off one QD could be channeled to interact with another QD to mediate spin-spin entanglement, but in order for the fidelity of such an operation to be near unity, the QDs must be interfaced with an optical cavity that can strongly couple a QD transition to a particular field mode [3, 4]. Since the QD is embedded in a solid-state structure, an optical cavity (microdisk, micropillar, photonic crystal) can be fabricated around the QD by lithographic techniques offering the possibility of an optically coupled QD spin circuit. In this circuit, one can imagine a QD spin coupled to a field mode of a cavity at each node, and the nodes are linked together with integrated optical waveguides. In recent years, there has been tremendous progress in realizing a strongly coupled QD-cavity system [36–38], and the current focus is realizing a strongly couple QD spin-cavity system and the deterministic coupling between QD spins located at different nodes of a primitive QD

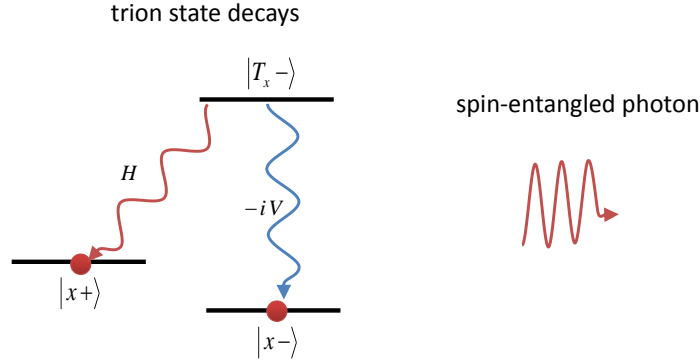


Figure 1.4: When the $|T_x-\rangle$ state decays by spontaneous emission, the polarization state (H,V) of the single spontaneously emitted photon is entangled with the spin state $(|x+\rangle,|x-\rangle)$ of the QD. This type of entanglement can be used in a two QD protocol, as shown in Figure 1.1 for trapped ions, to herald entanglement between distant QDs.

network [39–41].

Another approach uses two intermediate spin-photon entangled states to herald distant spin-spin entanglement. This would rely on a post-selection protocol similar the method demonstrated with trapped ions (Section 1.1.1). The benefit of this approach is that the entanglement is heralded by a measurement, so that distant spin-spin entanglement can be generated with near unity fidelity without requiring perfect coupling between the QD and a particular field mode. So it is possible to achieve high fidelity distant spin-spin entanglement without the use of a strongly coupled QD-cavity system. A limitation of the approach is that the heralding success rate decreases exponentially with the number of qubits, which will limit the practical size of the system, but still provides a useful platform for studying few qubit quantum networks.

Both of these approaches require the generation of a QD spin-photon entangled state, which is the primary focus of this thesis. In this work, we show that when the $|T_x-\rangle$ state of the QD decays by spontaneous emission, and light is collected along

the growth direction, a spin-photon entangled state of the form [42, 43],

$$|\Psi\rangle = \frac{|H\rangle|x+\rangle - i|V\rangle|x-\rangle}{\sqrt{2}}, \quad (1.5)$$

is generated, which is a maximally entangled state between the QD spin and the polarization state of the emitted photon. The entanglement is verified by performing correlation measurements between the QD spin and photon polarization in two bases. Developing the theoretical and experimental capabilities to execute such a measurement is the primary subject of this thesis. In addition to the spin-photon entanglement theory and experiment, various quantum optics measurements on single QDs are performed which further demonstrate the usefulness of optically driven QD spins for quantum information applications.

1.4 Chapter Summary

In this Chapter, the optically driven QD spin architecture is introduced, and a brief history of quantum information processing is given. Since an optically coupled QD spin is similar to a single trapped ion, recent progress in realizing a scalable ion-photon interface is reviewed to give context to some of the approaches pursued here. The primary focus of this work is demonstrating a QD spin-photon entangled state for scaling the QD spin architecture, which requires the development of quantum optics techniques and theoretical tools applied to the optically driven QD spin system.

CHAPTER 2

Optical and Electronic Properties of InAs Quantum Dots

GaAs, InAs and other direct band gap semiconductors have had tremendous impact in optical and electro-optical science and technology. Light emitting diodes, diode lasers and IR detectors are just a few of the practical devices that have emerged from these materials [44–46]. In addition to these applied technologies, semiconductor heterostructure science, based primarily on molecular beam epitaxy (MBE) [47], has led to the ability to engineer electronic wave functions in quantum well and QD structures. In more recent years, laser technologies based on semiconductor QDs have resulted in standard commercial products offering high stability operation at the $1.3\mu\text{m}$ telecom band [48]. Colloidal (II-VI) and epitaxial QDs also have potential applications in solar energy as tunable light absorbers [49]. Single QDs have been studied mainly for applications in quantum optics and quantum information science. They provide a very attractive system because their energy levels are atom-like, but unlike atoms, they can be tailored for specific applications [26]. In this chapter, we review some important electronic and optical properties of semiconductors, describe the InAs QD sample structure, present the energy eigenstates of a InAs charged QD, and review the optical selection rules for transitions between the energy levels.

2.1 Review of Semiconductor Band Structure

The optical and electronic properties of semiconductors are understood by studying the band structure of the materials. A basic property of crystalline materials is the existence of electronic energy bands that arise from the periodic nature of the

constituent atoms' potential. The simplest example of periodic potential gives rise to eigenstates known as Bloch states, which are extended states of the crystal. If the potential (V) is of the form,

$$V(\mathbf{r}) = V(\mathbf{r} + \mathbf{R}), \quad (2.1)$$

where \mathbf{R} is the spacing of the periodic potential, the resulting Bloch states are of the form,

$$\psi_{\mathbf{k}}(\mathbf{r}) = e^{i\mathbf{k}\cdot\mathbf{r}} u_{\mathbf{k}}(\mathbf{r}), \quad (2.2)$$

which is a plane wave envelope multiplied by $u_{\mathbf{k}}(\mathbf{r})$ which has the same periodicity as the potential. This general result is useful to keep in mind as we discuss the band structure of real semiconductors where the potential is composed of periodic lattice of atoms.

The electronic band structure of semiconductors can be calculated using various techniques [50]. One commonly used and instructive technique is known as the tight-binding method [51]. In the tight binding calculations, the wave functions of the constituent atoms' valence electrons are used as the basis states for the band structure calculation. The basic assumption is that these electrons are "tightly" bound so that there is limited overlap between the wavefunctions of neighboring atoms. Details of these calculations can be found in standard books on solid-state physics [46,50]. Here, we recall the approach and basic results following some of the notation in Singh [46]. In a tight-binding calculation, the Hamiltonian is taken to be of the form,

$$H = H_{atoms} + \epsilon(\mathbf{r}), \quad (2.3)$$

where H_{atoms} is the potential formed by the bare atoms, and $\epsilon(\mathbf{r})$ is a perturbation to this potential. The states are taken to be of the form,

$$\Psi_{\mathbf{k}}(\mathbf{r}) = \sum_{\mathbf{R}} e^{i\mathbf{k}\cdot\mathbf{R}} \phi(\mathbf{r} - \mathbf{R}), \quad (2.4)$$

where we sum over unit cell (\mathbf{R}), and $\phi(\mathbf{r})$ is expanded as a sum of the bare atomic states ψ_n such that,

$$\phi(\mathbf{r}) = \sum_n^N a_n \psi_n(\mathbf{r}), \quad (2.5)$$

where N is the number of atomic orbitals used. To find the expansion coefficients (a_n), we use the Schrödinger equation,

$$H\Psi_{\mathbf{k}} = E(\mathbf{k})\Psi_{\mathbf{k}} \quad (2.6)$$

and the orthonormality of the atomic wavefunctions to generate a system of N coupled equations. The terms involving integrals over ϵ and between different atomic sites are usually left as fitting parameters that are determined experimentally. Typically only a few of the atomic states are used as the basis states. Solving this system one can find N dispersion relations ($E(\mathbf{k})$), which make up the band structure.

For III-V semiconductors like InAs and GaAs, the crystal structure is zinc-blende, which is composed of two displaced face-centered cubic lattices. The outermost valence electrons of the constituent atoms (Ga, In and As) are s and p states. There is one s molecular orbital and three p orbitals (p_x, p_y, p_z), which are known as the sp^3 basis states. Using these as the basis states, a typical wavefunction for calculating a tight binding band structure is of the form,

$$\Psi_{\mathbf{k}}(\mathbf{r}) = \sum_{\mathbf{R}} \sum_{m=1}^4 \sum_{j=1}^2 A_{mj}(\mathbf{k}) \phi(\mathbf{r} - \mathbf{r}_j - \mathbf{R}) e^{i\mathbf{k} \cdot \mathbf{R}}, \quad (2.7)$$

where m indexes the sum over the four sp^3 basis states for each atom and j indexes the two atoms in each unit cell. \mathbf{R} is the sum over unit cells. Equations 2.6 and 2.7 can be used to determine the band structure up to several fitting parameters which are usually determined experimentally [46, 51]. Keeping this theoretical framework in mind, we now discuss some properties of the band structure.

A typical (undoped) semiconductor band structure consists of many energy bands, with the Fermi level falling between two bands. Because of this, we are usually interested in two of the energy bands: the “conduction” band that is directly above the Fermi level, and the “valence” band which is below the Fermi level. The energy difference between the lowest point in conduction band and the highest point in the valence band is called the bandgap. Since the translational symmetry of the system is given by the crystal structure, the physical momentum of electrons in a solid is usually not a useful quantity to consider. Instead, we use the crystal momentum

where charge carriers have an effective mass, m^* , which is given by the curvature of the bands. Electrons in the conduction band behave similarly to free electrons with the effective mass m_e^* . If an electron is missing from the valence band, it behaves as if there is positive charge carrier, known as a hole, with an effective mass m_h^* .

A semiconductor's optical properties, determined by the band structure, are typically organized into two categories. In *direct* bandgap semiconductors like GaAs and InAs, the conduction band minimum and valence band maximum occur for the same momentum (\mathbf{k}) (Figure 2.1). In *indirect* bandgap semiconductors like silicon and germanium, the conduction band minimum does not align with the valence band maximum. An important difference between a direct and indirect semiconductor's optical properties is the ability for electrons and holes to recombine radiatively. Due to energy and momentum conservation, optical transitions have to be vertical ($\Delta k = 0$) since optical photons carry negligible momentum. Excited electrons and holes rapidly relax down to the band edge, so carriers in direct bandgap semiconductors can radiatively recombine (since the transition is vertical), emitting photons, whereas in indirect bandgap semiconductors this process is highly suppressed due to the misalignment of the band edges ($\Delta k \neq 0$). This is why silicon usually can not be used for light emitting diodes and lasers. Since we are interested in efficient coupling of photons into and out of the semiconductor states, we will be concerned with direct bandgap semiconductors.

To understand the selection rules of optical transitions between energy bands, we need to understand the angular momentum states of electrons and holes. Unlike an electron bound in an atom that has continuous three dimensional rotational symmetry, an electron in a crystal is subject to the discrete rotational symmetries of the crystal's point group. Since angular momentum conservation comes about from rotational symmetry, angular momentum is not a "good" quantum number in a crystal. However, we can still associate the band edge states with angular momentum states. Electrons in the conduction band are *s* like, associated with the orbital angular momentum ($\mathbf{L} = 0$), and holes in the valence band are *p* like ($\mathbf{L} = 1$). This representation with atomic angular momentum states is valid because the irreducible

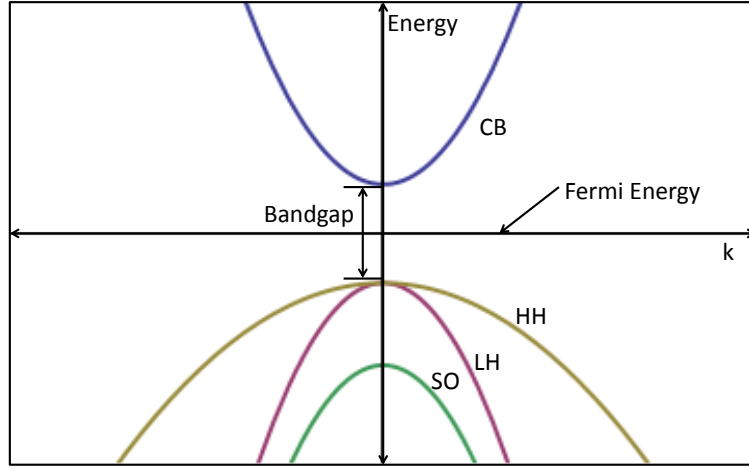


Figure 2.1: A simplified direct bandgap semiconductor band structure showing the conduction band (CB), heavy hole (HH) band, light hole (LH) band, and split off (SO) band. For an intrinsic semiconductor, the Fermi energy is centered between the lowest conduction band and highest valence band. In bulk the HH and LH bands are degenerate at $k = 0$, however in a QD. Due to spin-orbit coupling, the SO band is energetically distant and is usually not considered while studying the HH and LH.

representations of the band edge states transform under rotations like the s and p atomic orbitals. In the tight binding picture described above, this can also be seen as the conduction (valence) band edge states being composed of the s (p) constituent atomic basis states.

Electrons are spin $1/2$ particles. Since the valence band states are p like ($\mathbf{L} = 1$), we must consider the spin-orbit interaction which couples the spin (\mathbf{S}) and orbital (\mathbf{L}) angular momentum states. The Hamiltonian for this interaction is

$$H_{SO} = \lambda \mathbf{L} \cdot \mathbf{S}, \quad (2.8)$$

where λ is a constant.

Including the spin-orbit Hamiltonian, the new eigenstates are most easily found by re-writing the interaction in terms of the total angular momentum, $\mathbf{J} = \mathbf{L} + \mathbf{S}$,

so that,

$$H_{SO} = \lambda \frac{\mathbf{J}^2 - \mathbf{L}^2 - \mathbf{S}^2}{2}, \quad (2.9)$$

The spin-orbit interaction splits the hole eigenstates into three bands. They are called the heavy hole $|HH\rangle = |j = 3/2, m_j = \pm 3/2\rangle$, the light hole $|LH\rangle = |j = 3/2, m_j = \pm 1/2\rangle$ and the split off hole $|SO\rangle = |j = 1/2, m_j = \pm 1/2\rangle$, where the growth direction (z) sets quantization axis. One should note that the conduction (valence) band states are purely s (p) only at the Γ ($k = 0$) point. Away from the Γ point, the interaction between these states can be calculated using the Kohn-Luttinger Hamiltonian [52]. A simplified band structure for a direct band gap semiconductor is shown in Figure 2.1. In bulk, the heavy hole and light hole are degenerate at the Γ point; however, in a QD, these eigenstates are split by confinement and strain.

2.2 Excitons in Bulk

Incident optical radiation with energy at or above the band gap can excite electrons into the conduction band leaving behind holes in the valence band. There is an attractive Coulomb interaction between the negatively charged electron and the positively charged hole given by,

$$V_C = -\frac{e^2}{4\pi\epsilon r}, \quad (2.10)$$

where e is the electron charge, ϵ is the permittivity, and r is the separation of the electron and hole. For most semiconductors, this interaction can be treated as a perturbation to the band structure. The resulting bound electron-hole state is called an exciton and can be calculated using the Schrödinger equation with effective mass theory. The resulting exciton envelope solutions are similar to the hydrogen atom problem, but one should be careful with this analogy since the exciton is not a ground state of the system. The exciton is an excited state of the system, and it decays by radiatively recombining, resulting in a full valence band and no electrons in the conduction band. So in this sense, the problem is a better analogy to positronium,

the bound state between an electron and a positron. Excitons are usually classified as Frenkel, which typically have small Bohr radius ($a_0 \approx 0.1 - 1$ nm) and high binding energy ($E_B \approx 100 - 1000$ meV), or Wannier-Mott which have larger Bohr radius ($a_0 \approx 10 - 100$ nm) and low binding energy ($E_B \approx 1 - 10$ meV). In high ϵ semiconductors, like GaAs (and InAs), this interaction is fairly weak ($E_B \approx 5$ meV) so the excitons are Wannier-Mott. Since kT at room temperature is 26 meV, usually excitons in these materials are directly observable only at low temperature.

2.3 Excitons in QDs

A QD can be thought of as a three-dimensional square well which spatially confines electrons and holes. If the size of the QD is sufficiently small (relative to the exciton Bohr radius), the system becomes effectively zero-dimensional yielding a discrete energy states. Here, we study single self-assembled InAs/GaAs QDs (see Figure 2.2). Semiconductor QDs are made of a small band gap semiconductor (InAs) which is surrounded in all three dimensions by a large band gap semiconductor (GaAs) that gives rise to the spatial confinement of electrons and holes. The room temperature bandgaps of bulk InAs and GaAs are 0.35 eV and 1.42 eV respectively. The InAs QDs we study are approximately 2.8 nm tall and 20 nm in diameter that is small compared to typical exciton Bohr radii for bulk InAs and GaAs, which are 40 nm and 10 nm respectively [53]. Unlike bulk semiconductors where excitons are extended Bloch states of the crystal, the confinement in a QD leads to localized excitons, and it becomes possible to isolate a single exciton, since the strong Coulomb interaction between localized excitons leads to an anharmonic energy level structure. So if one exciton is created at $\hbar\omega$, the two exciton state (biexciton) occurs at a shifted energy $\hbar\omega + \Delta$, where Δ is the binding energy between excitons.

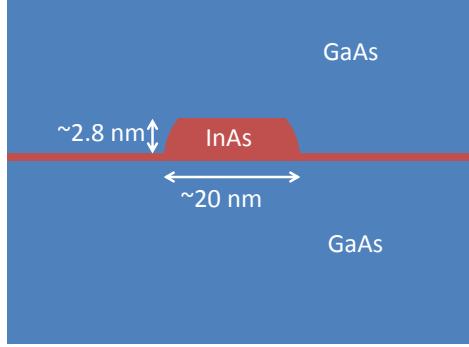


Figure 2.2: InAs islands form on top of a highly strained InAs wetting layer which grows on a GaAs substrate. After performing the indium flush technique the islands are capped with GaAs, forming the QD.

There are various methods for calculating QD wavefunctions, including effective mass theory, 8-band $\mathbf{k}\cdot\mathbf{p}$, and pseudopotential theory to name a few methods [54–56]. The basic result can be understood within the effective mass approximation treating electrons and holes separately. We start with the time independent Schrödinger equation,

$$\left(\frac{-\hbar^2}{2m_e} \nabla^2 + V_{\text{periodic}}(\mathbf{r}) + V_{QD}(\mathbf{r}) \right) \psi(\mathbf{r}) = E \psi(\mathbf{r}), \quad (2.11)$$

where, m_e is the free electron mass, V_{periodic} is the periodic part of the potential arising from the crystal, and V_{QD} the potential from the QD, associated with a larger (nm) length scale. Using effective mass theory, we can write,

$$\left(\frac{-\hbar^2}{2m^*} \nabla^2 + V_{QD}(\mathbf{r}) \right) \chi_{\text{env}}(\mathbf{r}) = E_{\text{env}} \chi_{\text{env}}(\mathbf{r}), \quad (2.12)$$

where m^* is the effective mass and instead of a standard Bloch wavefunction, the wavefunctions for carriers confined to QDs are of the form,

$$\psi(\mathbf{r}) = \chi_{\text{env}}(\mathbf{r}) u_0(\mathbf{r}) \quad (2.13)$$

where $\chi_{env}(\mathbf{r})$ is the envelope function and $u_0(\mathbf{r})$ is the rapidly varying periodic part of the wavefunction which is s like for electrons and p like for holes. One can solve Equation 2.12, subject to the QD confining potential, separately for electrons and holes to find the envelope wavefunctions. The naming conventions for the envelope and periodic parts of the wavefunction are similar, and should not be confused. For both electrons and holes, the lowest energy envelope wavefunctions are symmetric, and are called the “ s shell” envelope wavefunctions in analogy with the ground state of hydrogen, and the first excited states are called the “ p shell” envelope wavefunctions since they have odd parity.

The self-assembled InAs/GaAs QDs studied in this thesis are grown by molecular beam epitaxy (MBE) in the Stranski-Krastanov (SK) growth mode along the 001 crystal axis. InAs is deposited on a GaAs substrate, and the 7% lattice mismatch between the InAs and GaAs causes islands of InAs to form on top of an InAs wetting layer. Naively considering the bulk InAs bandgap, one might assume that excitons in InAs QDs would emit light at 0.35 eV. However, the QD structure modifies this energy in two interrelated ways: quantum confinement from the InAs/GaAs band gap mismatch, and strain from the InAs/GaAs lattice mismatch. The quantum confinement effects that arise from the band gap mismatch can be qualitatively understood in analogy to a three-dimensional square well potential, where the bound state energies are found to increase with decreasing well size. This square well picture is useful, but not complete. Since the InAs/GaAs QD growth process relies on the mismatch between the InAs and GaAs lattice constants, we have to consider the effect of strain on the QD’s electronic structure. The band structure (and resulting bandgap) is related to the semiconductor’s lattice constant, where a smaller (larger) lattice constant results in a higher (lower) bandgap. In the growth process, the InAs begins to grow coherently: the first few atomic layers adapt to the GaAs substrate’s lattice constant forming the (≈ 0.5 nm thick) wetting layer. As more InAs is deposited, the lattice constant begins to relax to its bulk value. After a critical thickness, the QDs form and are then capped with GaAs, so we can picture the effective lattice constant of the InAs varying between the layers of GaAs, as each InAs layer adapts to the neigh-

boring lattice. This distortion of the InAs lattice results in a built-in strain which shifts the QD energy. These effects result in the energy of an interband QD transition being determined by four major components,

$$E_{total} = E_{bandgap} + E_B + E_{confinement} + E_{strain}, \quad (2.14)$$

where E_B is the binding energy of the exciton. For the InAs QDs studied in this thesis, $E_{total} \approx 1.3$ eV. The contributions of $E_{confinement}$ and E_{strain} are approximately equal, and given that the $E_{bandgap} + E_B \approx 0.35$ eV, the QD energy is largely determined by the QD potential. In the self-assembly process, the location of each QD and the size/shape of each QD is random. Since the energy eigenstates are strongly dependent on the QD potential, an ensemble of QDs is inhomogeniously broadened over approximately 100 meV.

It should also be noted that temperature also affects these energies, which can be qualitatively understood in terms of the lattice constant changing with temperature. In this thesis, all experiments are performed under 10 K, which corresponds to a thermal energy of ≈ 0.9 meV. The confinement of carriers in the QD is strongest in the growth (z) direction (≈ 300 meV), and tens of meV in the transverse (x, y) directions, so the carriers are stable in the QD below 10 K ($k_bT \approx 0.9$ meV).

2.4 InAs Quantum Dot Structure and Characterization

When InAs QDs are first grown, they are approximately 20 nm in diameter and 5-10 nm tall, which when capped with GaAs results in QDs that emit radiation in the near infrared ($\approx 1.1\mu\text{m}$). In order to study the QDs with Ti:sapphire lasers and silicon detectors, the QD growth process is modified by a growth interruption technique known as the indium flush technique [57]. Here, after the QDs are grown, ≈ 3 nm of GaAs is deposited onto the wetting layer and the temperature is raised. The exposed InAs evaporates, effectively removing the top of the InAs QD. The QD is capped with GaAs resulting in a pancake-shaped InAs QD, which emits in the 900 – 1000 nm range [57].

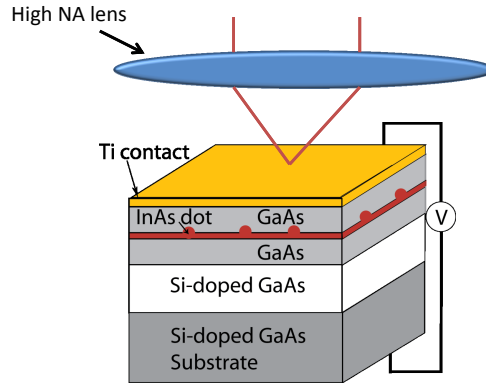


Figure 2.3: The sample structure showing the Schottky diode and GaAs heterostructure. The InAs QDs are located between two layers of intrinsic GaAs. The $n(\text{Si})$ -doped substrate provides electrons that can tunnel into the QD. An external bias voltage (V) is applied to deterministically charge the QD. A high numerical aperture (NA) aspheric lens is used to optically address single QDs.

The QDs are grown in a Schottky diode heterostructure shown in Figure 2.3, and consists of a $\approx 10^{18}\text{cm}^{-3}$ n -doped GaAs substrate, 40 nm intrinsic GaAs, 2.8 nm InAs, 280 nm intrinsic GaAs, and a 5 nm Ti layer which forms the top contact of the Schottky diode. The structure is designed for stable charging of the QD with electrons from the n -doped substrate (Naval Research Lab sample number: R081105). Forward biasing the diode raises the Fermi level so that electrons can tunnel into the QD. The Coulomb blockade effect allows for deterministic charging of the QD with single electrons, giving the charge configuration a macroscopic voltage existence range. The charge state of the QD is identified through bias dependent photoluminescence (PL) spectroscopy [58]. Electrons and holes are optically injected into the bulk material with a high energy laser (typically 500 – 900 nm). Some of these carriers non-radiatively relax to the low energy states of the QD where they can recombine, emitting radiation at the QD resonance energy. The QD PL is dispersed by a single grating spectrometer and detected by a cooled (CCD). A typical PL spectrum is shown in Figure 2.4.

By taking PL spectra as a function of applied sample bias, we are able to observe

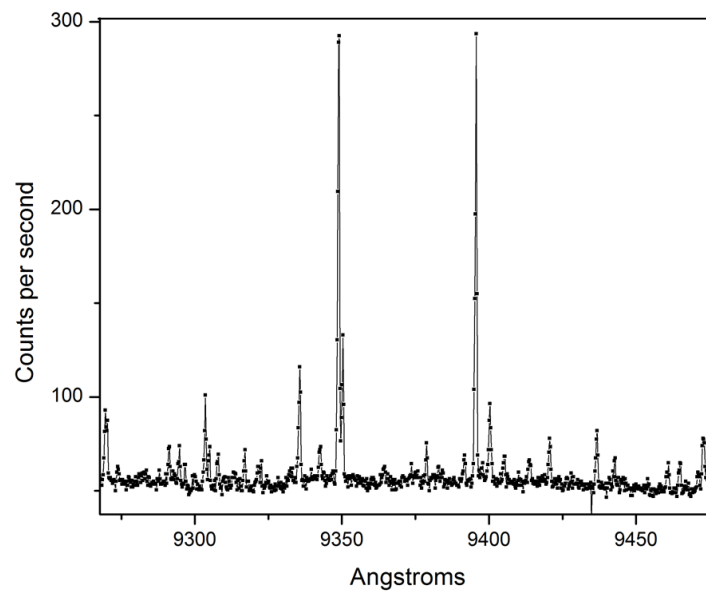


Figure 2.4: A typical QD photoluminescence spectrum at 4 K. Here, a few QDs are excited by the laser spot, contributing multiple emission lines.

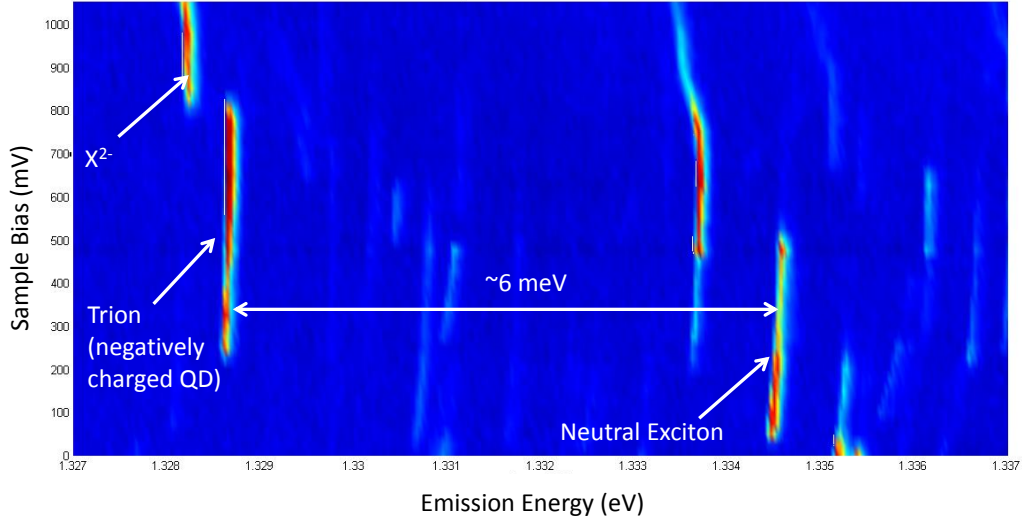


Figure 2.5: A bias dependent photoluminescence map showing the charging pattern of a single QD. The 6 meV jump in emission energy from the neutral exciton to the trion state is helpful in identifying the charge state. The X^{2-} state is also labeled. The other lines present on the PL map are from neighboring QDs that are also excited by the laser spot.

steps in the charging pattern which we can associate with a particular charge state of the QD (see Figure 2.5). The charge configuration which we discuss is the negatively charged exciton (called a trion) which is composed of two electrons and one heavy hole. These states are identified in bias dependent PL by a characteristic 6 meV jump in emission energy.

For many quantum information applications, it is useful to isolate a three-level “lambda” system where information can be stored in the long lived ground state sub-levels, and the system can be rapidly manipulated through the optically excited state. In order to realize this system with an InAs QD, we charge the QD with a single electron, and use the spin state of the electron as the qubit. The charged QD’s trion state can be used for optical coupling of the spin qubit.

2.5 Optical Transitions in Negatively charged QDs

In order to understand optical transitions in a negatively charged QD, we review some basic concepts from time dependent perturbation theory. The quantum mechanical description of light matter interactions begins with the time dependent Schrödinger equation for a charged particle, with mass (m) and charge (q) in an electromagnetic field,

$$i\hbar\psi'(t) = H_{e+m}\psi(t) \quad (2.15)$$

where,

$$H_{e+m} = \frac{|(\mathbf{P} - q\mathbf{A}/c)|^2}{2m} + q\phi, \quad (2.16)$$

where \mathbf{A} is the vector potential and ϕ is the static potential, and P is the canonical momentum. This $\mathbf{P} \cdot \mathbf{A}$ Hamiltonian can be re-formulated and instead written in terms of the dipole moment operator $\boldsymbol{\mu} = -e\mathbf{r}$ and the applied electric field \mathbf{E} such that,

$$H_{e+m} = H_0 - \boldsymbol{\mu} \cdot \mathbf{E}, \quad (2.17)$$

where $H_0 = \frac{P^2}{2m} + V_{periodic}(\mathbf{r}) + V_{QD}(\mathbf{r})$, so that the QD wavefunctions are eigenstates of H_0 , and the $\boldsymbol{\mu} \cdot \mathbf{E}$ term allows for transitions between these eigenstates.

We will typically consider the case where the applied electric field is taken to be a time varying classical field of the form,

$$\mathbf{E}(t) = \mathbf{E} \cos(kz - \omega t), \quad (2.18)$$

which is a traveling wave propagating opposite the sample's growth direction (z) where $\omega/2\pi$ is the frequency of the applied field and \mathbf{E} is the amplitude.

In order for an optical dipole transition to be allowed, the matrix element between two states $|i\rangle$ and $|j\rangle$

$$\langle j | \boldsymbol{\mu} \cdot \mathbf{E} | i \rangle \quad (2.19)$$

must be nonzero.

For the negatively charged QD, the ground state of the system is composed of a single electron in the lowest conduction band energy level which has angular momentum $|1/2, \pm 1/2\rangle$, with the notation $|j, m_j\rangle$. The lowest excited state of the system is the trion state composed of two conduction band electrons in a spin singlet and one heavy hole in the valence band. Since the electrons are in a singlet state, the angular momentum state of the trion is determined by the heavy hole state associated with $|3/2, \pm 3/2\rangle$. In a QD, the light hole state ($|1/2, \pm 1/2\rangle$) is not degenerate, but does contribute to a light hole heavy hole mixing effect, which results in a rotation of the optical selection rules [59], which we will come back to in Chapter 6. We will consider electric dipole transitions between the electron spin ground state and the heavy hole trion state. Since the growth direction (z) sets the quantization axis, we write the QD electron ground states as

$$\psi_{\pm z} = \chi_{s,c}(\mathbf{r}_e)|1/2, \pm 1/2\rangle, \quad (2.20)$$

where the $\chi_{s,c}(\mathbf{r})$ represents the envelope wavefunction, and the subscript labels that it is s shell and for a conduction (c) band state.

Similarly for the heavy hole trion we have,

$$\begin{aligned} \psi_{\pm tz} &= \chi_{s,v}(\mathbf{r}_h)|3/2, \pm 3/2\rangle \\ &\otimes \chi_{s,c}(\mathbf{r}_{e1})\chi_{s,c}(\mathbf{r}_{e2})\frac{1}{\sqrt{2}}(|1/2, +1/2\rangle_1|1/2, -1/2\rangle_2 - |1/2, -1/2\rangle_1|1/2, +1/2\rangle_2), \end{aligned} \quad (2.21)$$

The envelope wavefunctions for $\psi_{\pm z}$ and $\psi_{\pm tz}$ are included for completeness. Since all the envelope wavefunctions are s shell, they do not dramatically affect the selection rules because the overlap integral between any of these envelope wavefunctions is approximately 1. We have also written out the singlet state of the trion's electron pair, even though it will not affect the calculation of the selection rules. To simplify the problem, the states that we will use to calculate the optical selection rules are,

$$|z\pm\rangle = |1/2, \pm 1/2\rangle, \quad (2.22)$$

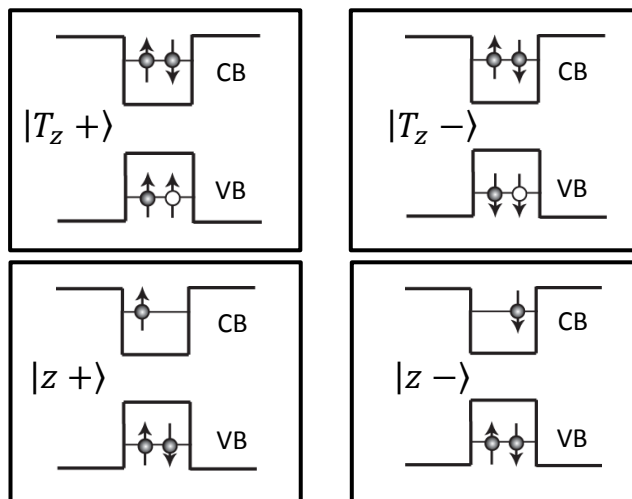


Figure 2.6: The four z -basis eigenstates of a negatively charged InAs. The ground states consist of a full valence band (VB) and single electron in the conduction band (CB) energy level. The lowest excited states consist of a singlet electron pair in the conduction band energy level and a heavy hole in the valence band.

and

$$|T_z \pm\rangle = |3/2, \pm 3/2\rangle. \quad (2.23)$$

For the remainder of this work, we will refer to these as the z -basis states (see Figure 2.6).

Since the irreducible representations of the electron and valence band edge states transform the same way as the atomic orbitals, we can derive the optical selection rules for transitions between eigenstates using the Wigner-Eckart theorem. This requires writing the interaction in terms of irreducible spherical tensors. We review some of the formalism and then apply the Wigner-Eckart theorem to find the charged QD selection rules.

We recall the complex spherical unit vectors,

$$\hat{\epsilon}_{+1} = -\frac{1}{\sqrt{2}} (\hat{x} + i\hat{y}) \quad (2.24)$$

$$\hat{\epsilon}_{-1} = \frac{1}{\sqrt{2}} (\hat{x} - i\hat{y}) \quad (2.25)$$

$$\hat{\epsilon}_0 = \hat{z} \quad (2.26)$$

$$(2.27)$$

where a vector $\mathbf{A} = A_x \hat{x} + A_y \hat{y} + A_z \hat{z}$ can be represented as,

$$\mathbf{A} = \sum_{q=-1,0,1} (-1)^q A_q \hat{\epsilon}_{-q} \quad (2.28)$$

and,

$$\mathbf{A} \cdot \mathbf{B} = \sum_{q=-1,0,1} (-1)^q A_q B_{-q} \quad (2.29)$$

Using this, the position operator, $\mathbf{r} = r$ can be written,

$$\mathbf{r} = r \sum_{q=-1,0,1} (-1)^q C_q^{(1)} \hat{\epsilon}_{-q} \quad (2.30)$$

where $C_m^{(l)} = \left(\frac{4\pi}{2l+1}\right) Y_{l,m}$, is the Racah tensor and the $Y_{l,m}$ are the spherical harmonics.

Similarly we can write the field as,

$$\mathbf{E} = \sum_{q=-1,0,1} (-1)^q E_q \hat{\epsilon}_{-q} = -E_{-1} \hat{\epsilon}_{+1} + E_0 \hat{\epsilon}_0 - E_{+1} \hat{\epsilon}_{-1} \quad (2.31)$$

Using Equation 2.29, the $\boldsymbol{\mu} \cdot \mathbf{E}$ dot product becomes

$$\boldsymbol{\mu} \cdot \mathbf{E} = -er \sum_{q=-1,0,1} (-1)^q C_q^{(1)} E_{-q} = -er \left(-C_{-1}^{(1)} E_{+1} + C_0^{(1)} E_0 - C_{+1}^{(1)} E_{-1} \right) \quad (2.32)$$

We recall that the Wigner-Eckart theorem gives,

$$\langle n' j' m'_j | r C_q^{(1)} | n j m_j \rangle = \langle n' j' || r C^{(1)} || n j \rangle \langle j 1, m_j q | j' m'_j \rangle, \quad (2.33)$$

where $\langle j 1, m_j q | j' m'_j \rangle$ is a Clebsch-Gordan (CG) coefficient, and $\langle n' j' || r C^{(1)} || n j \rangle$ is the reduced matrix element. The CG coefficient is zero unless, $m'_j = q + m_j$ and

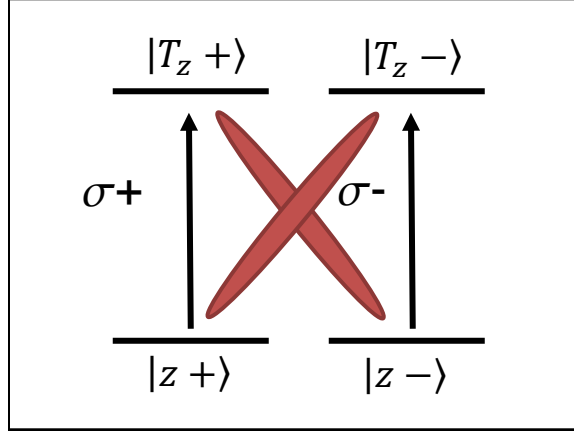


Figure 2.7: Energy level diagram of the z -basis eigenstates of a negatively charged QD. It is composed of two degenerate two-level systems with selection rules that allow for excitation with circularly polarized light. The cross transitions (red) are not allowed.

$|j - 1| \leq j' \leq j + 1$. To find the allowed optical transitions, we consider the matrix elements of Equation 2.32 with the z -basis states. For example, the matrix element between $|z+\rangle$ and $|T_z+\rangle$ is,

$$\begin{aligned} \langle T_z+ | \boldsymbol{\mu} \cdot \mathbf{E} | z+\rangle = \\ - e \left(-\langle T_z+ | rC_{-1}^{(1)} | z+\rangle E_{+1} + \langle T_z+ | rC_0^{(1)} | z+\rangle E_0 - \langle T_z+ | rC_{+1}^{(1)} | z+\rangle E_{-1} \right) \end{aligned} \quad (2.34)$$

where we have taken the dipole approximation. Applying the Wigner-Eckart theorem, the only nonzero term is, $\langle T_z+ | rC_{+1}^{(1)} | z+\rangle E_{-1}$. By looking at Equation 2.31, we find that E_{-1} corresponds to the \hat{e}_{+1} spherical unit vector. We can relate this to the polarization state of the field by recalling that circularly polarized light is defined as,

$$\sigma_{\pm} = \mp \hat{e}_{\pm 1} = \frac{1}{\sqrt{2}} (\hat{x} \pm i\hat{y}) \quad (2.35)$$

So, we find that $\sigma+$ polarized light excites the transition from $|z+\rangle$ to $|T_z+\rangle$. Similarly, $\sigma-$ polarized light excites the transition from $|z-\rangle$ to $|T_z-\rangle$, and

$$\langle T_z- | \boldsymbol{\mu} \cdot \mathbf{E} | z+\rangle = \langle T_z+ | \boldsymbol{\mu} \cdot \mathbf{E} | z-\rangle = 0. \quad (2.36)$$

These selection rules are summarized in Figure 2.7, where the cross transitions are not allowed. In later chapters, we will apply an external magnetic field which mixes these

z -basis and forms a lambda type system. The lambda system will allow for optical manipulation of the electron spin ground state, and the creation of a spin-photon entangled state.

2.6 Chapter 2 Summary

In this chapter, we summarized some important properties of direct bandgap semiconductors. Self-assembled InAs QDs were introduced and the sample structure presented. We found that the energy level structure of a charged QD is composed of two degenerate two-level systems. In the next two chapters, we will use this system to develop the experimental capabilities required for quantum optics measurements and the spin-photon entanglement experiment.

CHAPTER 3

Fluorescence from Single Quantum Dots

In quantum information applications of optically driven QD spins, photons are used to map information into and out of the QD spin state. A simple way to read information out of the spin state is to apply a narrow bandwidth pulse to the QD which maps one of the spin state populations into an excited state population which can then decay, emitting a single photon which is detected by a single photon detector. Furthermore, the spontaneously emitted photon from the QD's trion state is entangled with the resulting spin ground state [20, 42, 43, 60–62], and can be used to herald entanglement between distant QD spins [5]. These quantum information applications require the ability to directly detect the photons emitted from a single QD when driven on or near resonance. In this chapter, the theory of a driven two-level system is presented and related to the fluorescence signal. The experimental realization of resonance fluorescence is described in detail.

3.1 Resonantly Driven Two-Level QD System

A two-level system is coupled by an allowed optical dipole transition. When this system is driven by a nearly resonant excitation field, it scatters photons into a solid angle of 4π . In this thesis, all “absorption” experiments are performed with a coherent driving field from a narrow bandwidth cw laser. The scattered field can be homodyned with the transmitted laser field to give an absorption signal. Alternatively, the light scattered by the two-level system can be directly detected if the excitation field can be sufficiently rejected. Fluorescence intensity spectrum of the two-level system can be

obtained by tuning the frequency of the driving field through the resonance, revealing a Lorentzian profile at the natural line width.

“Resonance fluorescence” (RF) is often studied with a monochromatic excitation field tuned exactly on resonance [63, 64]. The frequency spectrum of QD resonance fluorescence, and the first and second order correlation functions have been studied previously [65–67]. The results qualitatively agree with theoretical predictions, however, deviations from the ideal two-level resonance fluorescence theory indicate the influence of QD’s environment. These deviations are usually attributed to spectral wandering arising either from charge fluctuations from trapped surface states near the QD causing an effective Stark-shift, or the hyperfine interaction with the QD’s constituent ($\approx 10^5$) nuclear spins which cause an effective Zeeman-shift that fluctuates in time. In this chapter, we limit the discussion to the fluorescence intensity which is proportional to the system’s excited state population [68],

Here, we use a semi-classical approach, taking the driving field to be an sinusoidal classical field following *Berman and Malinovsky* [68]. The system is modeled as a closed two-level system with an allowed electronic dipole transition. The Hamiltonian for the system in the rotating-wave approximation is given by,

$$\mathbf{H}(t) = \frac{\hbar}{2} \begin{pmatrix} -\omega_0 & \Omega_0^*(t)e^{i\omega t} \\ \Omega_0(t)e^{-i\omega t} & \omega_0 \end{pmatrix}, \quad (3.1)$$

where ω_0 is the resonance frequency, and ω is the field frequency. The Rabi frequency is $\Omega_0 = \mu E_0/\hbar$, where μ is the dipole moment of the optical transition, and E_0 is the driving field’s amplitude.

We move to a field interaction picture, where the density matrix is now represented as, $\tilde{\rho} = e^{-i\frac{\omega t}{2}\sigma_z} \rho e^{i\frac{\omega t}{2}\sigma_z}$, and the Hamiltonian is now,

$$\tilde{\mathbf{H}}(t) = \frac{\hbar}{2} \begin{pmatrix} -\delta & \Omega_0^*(t) \\ \Omega_0(t) & \delta \end{pmatrix}, \quad (3.2)$$

where $\delta = \omega_0 - \omega$ is the detuning. The density matrix evolves in time according to the master equation,

$$i\hbar\tilde{\rho}/dt = [\tilde{\mathbf{H}}, \tilde{\rho}] + \text{relaxation terms}, \quad (3.3)$$

which yields the following equations of motion,

$$\dot{\tilde{\rho}}_{11}(t) = -i\chi^*(t)\tilde{\rho}_{21}(t) + i\chi(t)\tilde{\rho}_{12}(t) + \gamma_2\tilde{\rho}_{22}(t) \quad (3.4)$$

$$\dot{\tilde{\rho}}_{22}(t) = i\chi^*(t)\tilde{\rho}_{21}(t) - i\chi(t)/2\tilde{\rho}_{12}(t) - \gamma_2\tilde{\rho}_{22}(t) \quad (3.5)$$

$$\dot{\tilde{\rho}}_{12}(t) = -(\gamma - i\delta)\tilde{\rho}_{12}(t) - i\chi^*(t)[\tilde{\rho}_{22}(t) - \tilde{\rho}_{11}(t)] \quad (3.6)$$

$$\dot{\tilde{\rho}}_{21}(t) = -(\gamma + i\delta)\tilde{\rho}_{21}(t) + i\chi(t)[\tilde{\rho}_{22}(t) - \tilde{\rho}_{11}(t)], \quad (3.7)$$

where γ is the decoherence rate, γ_2 is the excited state decay rate and $\chi = \Omega_0/2$. These equations can be solved algebraically in steady state by setting the time derivatives equal to zero. The excited state population is [68],

$$\rho_{22} = \frac{\frac{2\gamma}{\gamma_2}|\chi|^2}{\gamma^2 + \delta^2 + \frac{4\gamma}{\gamma_2}|\chi|^2}. \quad (3.8)$$

The fluorescence intensity is related to ρ_{22} in steady state with,

$$\text{Intensity}(\chi, \delta) = \rho_{22}(\chi, \delta)\gamma_2\eta\tau, \quad (3.9)$$

where η is the detection efficiency of the experimental setup and τ is the integration time.

Further details on the theory of resonance fluorescence spectrum and the coherence properties of the scattered radiation can be found in quantum optics textbooks [68–71]. For now, this result is sufficient to explain the fluorescence signal of a single charged QD.

3.2 Experimental Setup and Results

As described in Chapter 2, an effective two-level system is formed by a negatively charged InAs QD which is composed of two degenerate two-level systems (Figure 3.1). A linearly polarized excitation laser can drive both transitions, and the scattered photons can be detected on axis by placing an orthogonal polarization analyzer before the detector. A trion state is identified through bias dependent photoluminescence, and voltage modulation absorption spectroscopies as described previously [58, 59, 72, 73]. The primary challenge in resonant direct detection experiments is separating the light

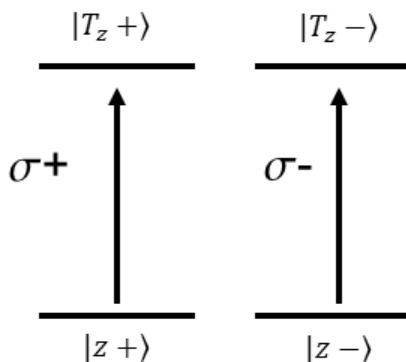


Figure 3.1: The energy level diagram for a negatively charged InAs QD, composed of two degenerate two-level systems. $\sigma+$ ($\sigma-$) polarized light drives the transitions, so horizontally polarized light can be used to simultaneously couple to both of the transitions, while the vertically polarized QD photons can be directly detected.

scattered or emitted from the QD from the excitation lasers used to drive the QD transition since spectral filtering cannot be used. The remaining standard rejection techniques include: spatial filtering through alignment or use of an iris/aperture, temporal filtering by time gating the detection either electronically or optically, and polarization filtering by cross polarizing the detection axis from the excitation axis. All of these techniques are combined to achieve adequate rejection in the demonstration of spin-photon entanglement. For continuous wave (cw) experiments presented in this chapter, a carefully designed crossed polarization setup provides sufficient rejection.

In order to achieve efficient mode matching between the incident laser field and the QD's dipole, the area of the focussed beam spot should roughly be the same size as the cross-sectional area of the optical-dipole transition [74]. For the QD's transition, whose dipole exhibits minimal decoherence, this corresponds to $\approx 1 \mu\text{m}$, which corresponds to a near diffraction limited spot on the QD, since the wavelength is $\approx 950 \text{ nm}$. In order to achieve this, previous experimental designs utilized an aluminum mask with micron-sized apertures effectively working in the near field. Polarization measurements on these samples showed that the metallic apertures dramatically dis-

torted the polarization integrity and limited the polarization rejection to $\approx 100\times$. Since polarization and spatial filtering are required to isolate the QD fluorescence from the laser pulses in an RF experiment, an alternative approach is used. A pair of aspheric lenses mounted to either side of the sample package focus and collect light. This approach has the advantage of significantly improving the polarization integrity of the transmitted beam, so that polarization rejection alone can be used to achieve rejection exceeding $10^6\times$. In addition, since high numerical aperture (NA) lenses are used, a much smaller beam spot diameter ($1-2\ \mu\text{m}$) is realizable on the sample which allows for substantially lower input powers to realize the same effective field on the QD.

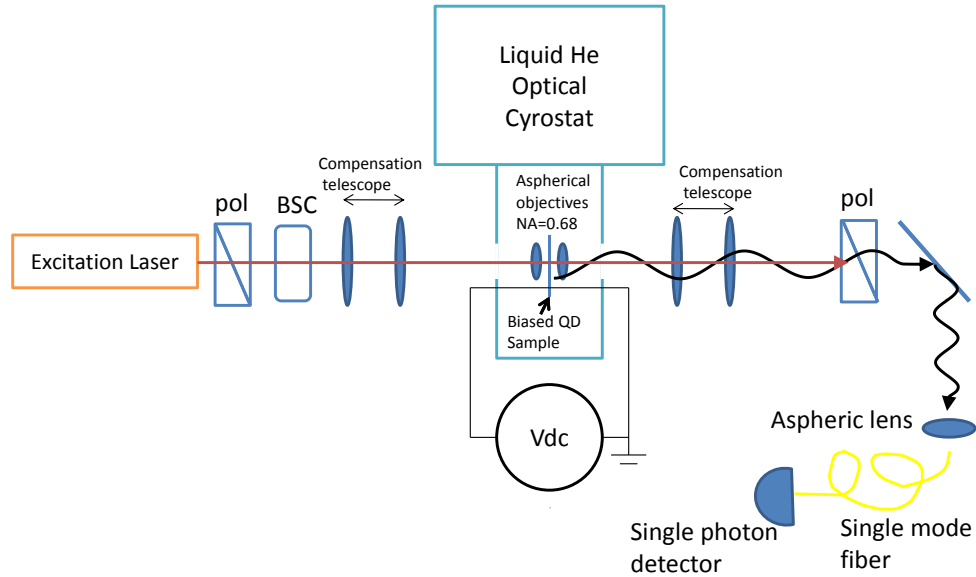


Figure 3.2: Schematic diagram of the direct detection setup. The polarization of the excitation laser is set with a polarizer and Babinet-Soleil compensator. The laser is passed through a 1 : 1 compensation telescope before it is focussed onto the sample by a 0.68 NA aspheric lens. Light is collected with another 0.68 NA lens in the transmission geometry and passed through another 1 : 1 compensation telescope. The excitation laser is blocked with a polarizer set orthogonal to the transmitted beam. The QD fluorescence is focussed into a single mode fiber and detected with a single photon detector.

Voltage modulation (VM) absorption experiments are performed by applying a square wave (typ. 1 kHz) modulation voltage across the Schottky diode which Stark shifts the QD resonance allowing for the use of phase sensitive detection using a lockin amplifier [72]. For this sample structure (Chapter 2), typical Stark shifts for trion resonances are on the order of 1 Volt per wavenumber. VM absorption experiments are usually performed either in the “small” (≈ 20 mVpp) or “large” (≈ 200 mVpp) modulation regimes. For small modulation, the modulation amplitude is smaller than the trion state’s line width, which results in a derivative line shape. For the “large” modulation regime, where the modulation amplitude is larger than the trion state’s line width, the resulting line shape should be the same as the unmodulated profile. More details on the VM technique can be found in previous theses [59, 73].

In previous sample designs where $\approx 1 \mu\text{m}$ metallic apertures were used to perform single QD absorption spectroscopy, dramatic line shape distortions and line broadening were frequently observed (Figure 3.3). Other groups have reported similar results, and some attribute the distortion to a non-linear Fano effect caused by the excited state coupling to a 2D continuum in the sample structure [75]. These effects have also been explained as non-trivial interference effects from internal sample reflections where the real and imaginary part of the QD’s optical response are mixed [76]. Moving to the “aperture-free” samples and using high NA lenses, we find that these line shape distortions vanish almost completely (Figure 3.4). This dramatically simplifies the characterization of the QD state since previously one had to search for a “good” QD state with minimal line shape distortion before more complicated experiments (often relying on the ability to fit to the line shape) could be performed. On the aperture-free samples, QD resonances typically exhibit absorption line widths of 400-600 MHz.

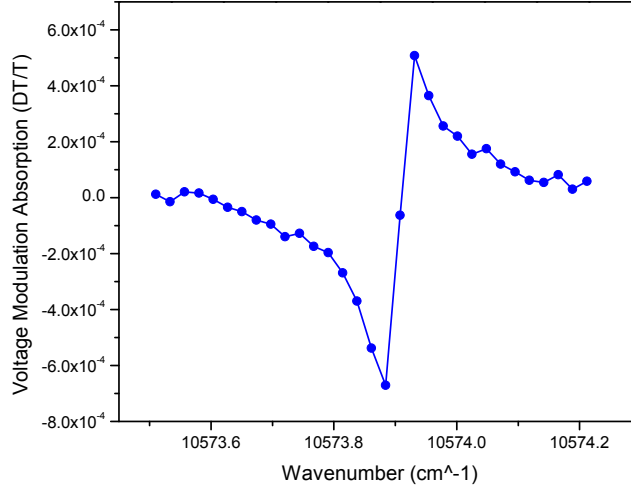


Figure 3.3: An example of a typical (distorted) VM absorption spectrum on a single trion in an apertured sample. Here large modulation is used so the signal should be modeled as a Lorentzian. The line shape distortion is believed to arise from reflections in the sample which mix the real and imaginary parts of the QD’s optical response.

The aspheric lenses are aligned at room temperature by approximately collimating the back reflection of a collimated input beam (950 nm) from the front of the sample and then collimating the transmitted beam. The best performance has been achieved when the back reflected beam at room temperature is slightly diverging. A good test of the alignment is the magnitude of the single QD VM absorption signal (DT/T). For a typical cw VM absorption experiment, the incident power is typically 100 nW. When aligned properly, the transmitted power is 10 – 15% of the incident power. The transmitted beam is focussed onto a Hamamatsu S8890-15 avalanche photodiode (APD) with a ≈ 10 cm lens. When the APD biased at 50 – 100 \times gain (typically 450 V), it is operating in its linear regime and has a photosensitivity of $\approx 30 - 65$ A/W. The photocurrent is shunted across a 10 k Ω resistor, to yield a voltage in the range of 1-10 mV. A VM absorption signal (DT/T) of $1 - 2 \times 10^{-3}$ is indicative that the lenses and sample are well-aligned. A typical “aperture-free” VM absorption signal is shown in Figure 3.4.

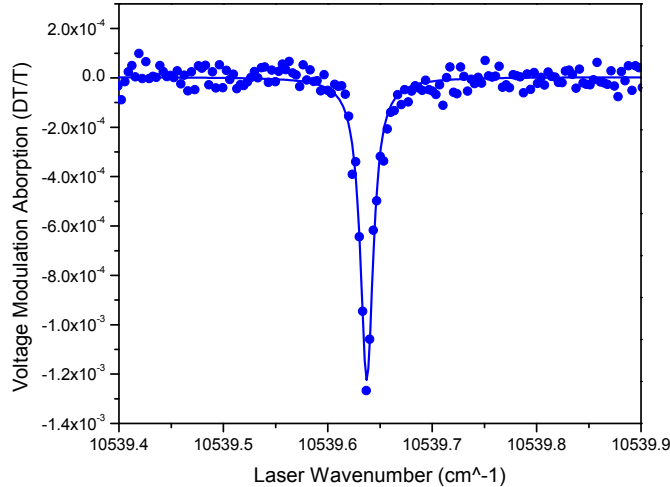


Figure 3.4: An example of a typical voltage modulation absorption spectrum on a single trion in an aperture-free sample. Large modulation is used so the line shape should be a Lorentzian. The solid line is a fit to a single Lorentzian with a line width of 450 MHz.

The basic setup for observing single QD RF is shown in Figure 3.2. Its primary components are: a cw laser, an input polarizer, an optical cryostat holding the sample, a polarization analyzer, a fiber coupled single photon detector, and a photon counter. The laser is a narrow (< 1 MHz) bandwidth tunable Ti:sapphire ring laser (Coherent 899-21) operating between $\approx 890 - 980$ nm. For the InAs QDs studied here, the QD resonances are typically 950 nm. The laser is horizontally (H) polarized by a high quality (10^6 extinction ratio) calcite polarizer (Glan-Thompson) before it is focussed onto the front (titanium side) of the sample by a 0.68 NA aspherical lens (Thorlabs 352330-B), which is mounted onto the sample package with custom made lens holder (Figure 3.5). The transmitted light is collected by a 0.68 NA aspherical lens on the back of the sample. The transmitted beam is then passed through a polarization retarder (Babinet-Soleil Compensator or quarter-wave plate) which is used to correct for birefringence in the windows, lenses and sample. A high extinction ratio (thin film) polarization analyzer that is set to pass vertically (V) polarized light rejects the excitation laser, but due to the circularly polarized selection rules of the charged

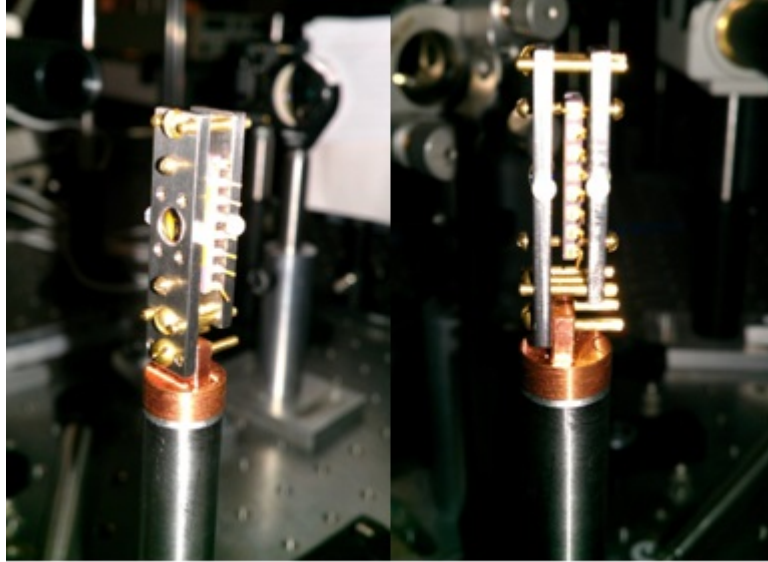


Figure 3.5: The lens/sample mount. Precision dowel rods keep the lenses aligned in two dimensions. 0-80 set screws are used to adjust the focus of the lenses.

QD, half of the collected RF still passes. The fluorescence is coupled into a single mode fiber (SM800, ≈ 0.12 NA) with an under filled 0.16 NA aspheric lens (Thorlabs C260TME-B) and detected by a single photon avalanche detector (SPAD).

It is important to note that using a single mode fiber is crucial for achieving this application. After the polarization analyzer, the excitation laser is only attenuated by $\approx 10^4\times$, which is not sufficient for RF measurements. The mode of the transmitted laser has a four-lobed cross structure known as a “Maltese cross” (see Figure 3.6). This pattern arises due to polarization aberrations that occur on the curved surface of the high NA lenses since s and p polarizations acquire different phases at the interfaces. The net effect of these aberrations has been studied and results in a transmitted mode that is almost exactly orthogonal to the Gaussian input mode of the single mode fiber [77,78]. The advantage is that the collected QD fluorescence can be collected over a relatively large solid angle (≈ 0.68), but the remaining excitation laser leak through cannot couple to the fiber due to its spatial mode structure. Of course, these polarization aberrations will also limit the polarization purity of the QD fluorescence to $\approx 10^{-4}$, which reduces the achievable fidelity of a spin-photon

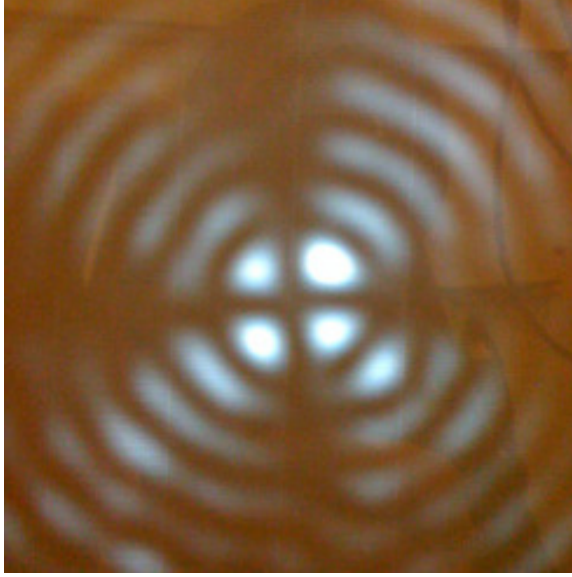


Figure 3.6: An example of a Maltese cross pattern formed by a cross polarization setup and a high NA objective. Photo courtesy of Jieun Lee.

entangled state. These polarization aberrations are not the dominant limitations on the fidelity (currently $\approx 10^{-2}$), but they can in principle be corrected for with an appropriate lens system [78].

Here, a brief summary of the alignment procedure for fluorescence experiments is given. The alignment of the excitation laser to the QD is peaked by maximizing the VM absorption signal (DT/T). The laser power is then increased to 1 mW, and the polarization analyzer is then set to pass the excitation laser. This beam is then coupled into a single mode fiber with a power meter, 60% is typically achievable if the aspheres are well aligned. The polarizer and retarder are then adjusted against each other to zero the reading on the power meter. The excitation power is then lowered to 200 nW incident (≈ 20 nW transmitted, $\approx 10^{11}$ photons per second) and the collection fiber is connected to the SPAD. The QD can be tuned off resonance using the DC Stark effect, and the remaining laser leak through can be rejected by servoing the analyzer and retarder. Typically this is done until the excitation laser is not visible over the dark counts (10-50 cps). Reasonable higher powers can be used to increase the sensitivity. When the QD is tuned back into resonance using

the bias, the RF counts are clearly visible in the range of 5 kcps using the Micro Photon Devices (MPD) “PDF series” SPAD and 50 kcps using the Picoquant τ -SPAD, corresponding to detection efficiencies (η) on order of 5×10^{-6} and 5×10^{-5} respectively. This procedure assumes that the (QD-aligned) transmitted laser is a good approximation for the output mode of the QD’s dipole transition, which is not exact. At this stage, one might try to increase the RF signal by peaking the alignment of the collection optics. Changes to the alignment will slightly change the polarization and therefore reduce the rejection, so the QD fluorescence will quickly get swamped by excitation laser leak through. To overcome this, the sample is voltage modulated, and the output of the SPAD is sent to a lockin amplifier locked to the modulation frequency. The unmodulated background does not contribute to the lockin reading, so the RF signal can be peaked. After peaking, the polarization optics have to be reset to minimize the laser leak through, but the RF signal is now optimized. Once the collection alignment is optimized, further spatial rejection of the excitation lasers can be obtained by adjusting the excitation laser alignment to excite the QD at a slight angle relative to the detection axis. This is accomplished most easily by walking the excitation laser alignment with two steering optics while monitoring the DT/T VM absorption signal to insure that the excitation laser remains aligned to the QD. An example of a typical fluorescence spectrum is shown in Figure 3.7, with a fit to the Lorentzian profile as predicted by Equations 3.8,3.9.

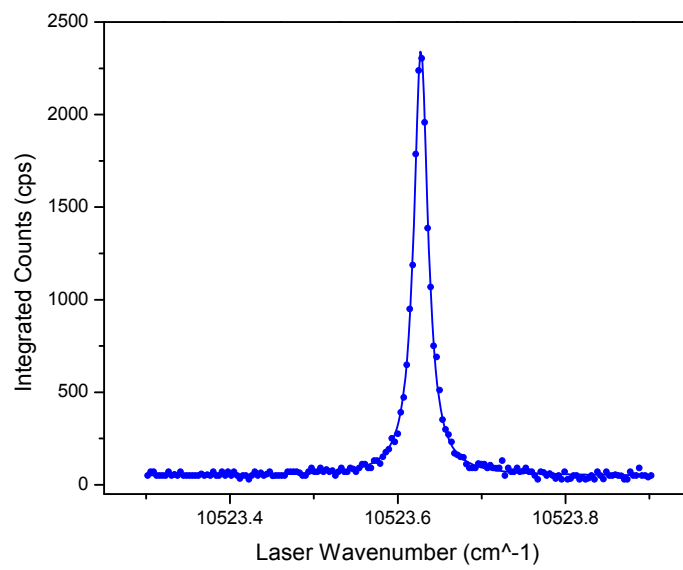


Figure 3.7: An example of a QD fluorescence intensity spectrum of a single trion state measured with the MPD-PDF detector. The solid line is a fit to a Lorentzian with a power-broadened line width of 611 MHz.

3.3 Chapter 3 Summary

In this chapter, the basic theory of a driven two-level system is reviewed using the density matrix formalism. Single QD absorption measurements are reviewed, highlighting the differences in typical QD line shapes observed on “apertured” and “aperture-free” samples. The experimental apparatus used to measure single QD fluorescence is described in detail. Finally, direct detection of the QD fluorescence is experimentally realized and the line shape is found to be a Lorentzian consistent with the theoretical prediction.

CHAPTER 4

Time-Domain Measurement Techniques

In Chapter 3, we developed the techniques allowing for direct detection of QD fluorescence under resonant cw excitation. In the next chapter, the QD is investigated by transient measurements of the QD fluorescence under resonant excitation, which will serve as the foundation for quantum information applications which are executed in the time domain. For these time domain measurements, we use a technique known as time-correlated single photon counting to measure single photons emitted from the QD. We also need to develop techniques to generate high quality narrow band optical pulses, which are capable of spectrally isolating specific QD transitions. In this chapter, we introduce these techniques which are used for the remainder of this work.

4.1 Time-Correlated Single Photon Counting

Time-correlated single photon counting (TCSPC) is a well-established spectroscopy technique, that was first developed to observe the time dependence of scintillation intensity [79]. In optical science, TCSPC is typically used to determine fluorescence lifetimes of excited molecular states by (indirectly) obtaining a measure of the fluorescence intensity as a function of time. Here, we present a brief description of the technique, but further information can be found in books dedicated to TCSPC [80].

The purpose of TCSPC is to measure the decay rates of an excited system. In this work, we consider the case of exciting a single charged QD, which is modeled as an effective two-level, although the method is often applied to ensembles of complex

molecules which can have multiple decay rates. The sample is typically excited with a short pulse (relative to the excited state lifetime) that is periodic in time at some repetition period (T_{rep}). The light emitted from the sample is collected with a lens and then detected with a photodetector. With an ensemble of molecules, which can generate a large fluorescence intensity, one could consider directly detecting this emission with a normal photodetector whose photocurrent is linearly proportional to the incident intensity. This photocurrent could be recorded as a function of time with an oscilloscope triggered off the excitation laser. This method can be used to perform fluorescence lifetime measurements, but it has significant limitations for weak signals or fast decay rates, due to electronic noise and bandwidth.

The TCSPC method overcomes these challenges by using single photon detectors, which output a large electronic pulse that can be triggered by a single incident photon. These electronic pulses are sent to timing electronics which measure the arrival time relative to the excitation laser pulse. The detection events are time binned in a histogram, and after the experiment is repeated many times, the histogram yields a measure of the fluorescence intensity as a function of time. The crucial aspect of TCSPC is that although the pulse width and rise/fall times can be relatively long, (≈ 20 ns and ≈ 1 ns respectively), the uncertainty in the pulse arrival time can be as low as ≈ 30 ps for state of the art systems. This uncertainty is called the *timing resolution* or *timing jitter* of a TCSPC setup. The timing resolution is usually measured by leaking a low intensity of the short (≈ 1 ps) excitation pulse onto the detector. This effectively gives the $\delta(t)$ -function response of the system and is referred to as the instrument response function (IRF). The width (FWHM) of the IRF gives the timing resolution of the TCSPC setup. In principle, the signal can be deconvolved with the IRF to further reduce the timing uncertainty of a measurement, but in practice, these methods are limited by the signal-to-noise ratio.

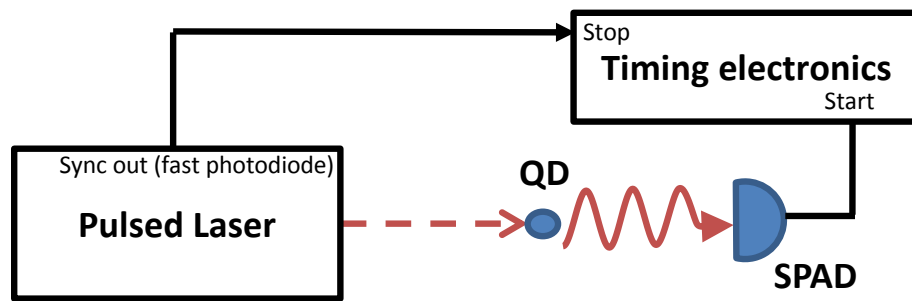


Figure 4.1: A typical TCSPC showing: a pulsed laser, a QD sample, a (SPAD) single photon detector and the timing electronics. In a traditional (TAC based) TCSPC setup, the signal from the SPAD starts the clock, and sync signal of a fast photodiode measuring the excitation laser pulses stops the clock.

The system's timing resolution is usually limited by the timing jitter of the detector. In this work, we use silicon single photon avalanche detectors (SPADs), which are avalanche photodiodes designed to operate reverse biased above the breakdown voltage. A useful review of modern single photon detectors has been published recently by R. Hadfield [81]. In a SPAD, a single photon can create an electron-hole pair in the detector's active region. The high reverse bias imparts sufficient energy onto the electron and hole so that they can excite more carriers leading to an "avalanche" effect. In this avalanche mode, a single photon can produce a large milliamp photocurrent pulse composed of $\approx 10^{15}$ electrons. A limitation of the technology is that the exact amplitude (height) of the pulses is somewhat random and is not dependent on the number of photons in a given pulse, so that 1 photon pulse incident the detector generates the same electric pulse as a 1000 photon pulse hitting the detector. It should be noted that recent technological advances have begun to overcome this limitation [81,82]. The output pulses are amplified to match the "NIM pulse" standard which is a negative (typically -800 mV) pulse into 50Ω . After a pulse is created, the SPAD requires some time to reset before it can detect another photon. This reset time is called the detector's dead time, and is controlled by a quenching circuit. This dead time sets the maximum count rate a detector can handle. SPADs also exhibit an effect known as afterpulsing, where after the dead time, there is a nonzero probability for the detector to fire another (false) pulse. In SPAD design, dead time and afterpulsing probability are deeply related since the probability of afterpulsing goes down with a longer dead time. SPADs also produce dark counts, which are caused by the thermal excitation of carriers, and increase with larger area detectors and higher temperature. Dark counts are suppressed by using detectors with small active areas ($20 - 150 \mu\text{m}$) and by cooling them with integrated thermo-electric coolers.

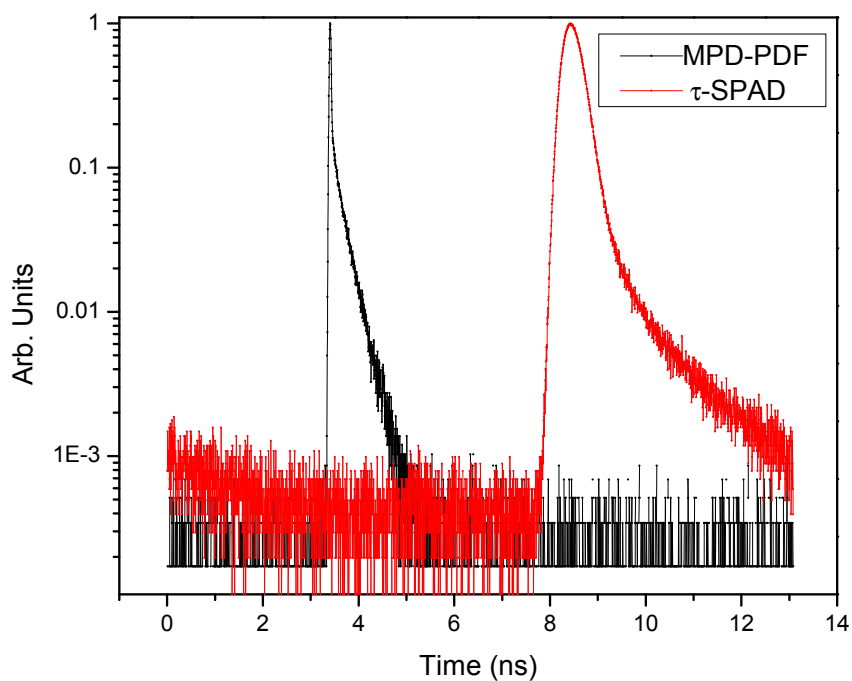


Figure 4.2: Instrument response functions from the fast “PDF” detector (black) and high detection efficiency “ τ -SPAD” detector (red) measured with a TCSPC setup similar to Figure 4.1 by leaking some of the excitation laser onto the detector. The widths (FWHM) shown here are approximately 45 ps and 450 ps respectively. The detector “tails” arise from carriers created in the low field region of the detector.

The thickness of the SPAD’s active region affects the detection efficiency and the timing resolution. A thick active region is more likely to absorb a photon, which increases the detection efficiency, but this also increases the timing jitter of the detector because the depth at which the carriers are created affects the timing of the output pulse. In this thesis, we use two different models of SPADs: a fast timing SPAD (Micro Photon Devices- PDF model) and a high detection efficiency SPAD (Picoquant τ -SPAD model). The PDF detector is coupled with a single mode fiber (SMF-28, FC/PC connector) and has a timing jitter of $\approx 40 - 50$ ps (FWHM) with a detection efficiency of $\approx 2\%$ at 950 nm. The τ -SPAD detector has a $150 \mu\text{m}$ active area, a timing jitter of ≈ 450 ps (FWHM) with a detection efficiency of $\approx 20\%$ at 950nm. Both detectors have low dark counts < 25 cps and afterpulsing probability of $1 - 3\%$. The detector dead times are both approximately $50 - 70$ ns which yields a maximum count rate of approximately 10 Mcps. The instrument response functions for the PDF and τ -SPAD are shown in Figure 4.2. The IRFs are not temporally symmetric, and show a relatively slow “tail.” The tail arises from carriers that are created in the low field region of the detector which slowly drift into the high field region before they can trigger an avalanche. Since the fluorescence signals are convolved with this asymmetric IRF, the raw data can appear distorted or stretched out towards positive time. Nevertheless, the narrow FWHM of the IRF dominates the useful timing resolution of the detector.

The major components of a traditional TCSPC experiment are a: pulsed laser, sample, single photon detector, fast photodiode, constant fraction discriminator (CFD), time-to-amplitude converter (TAC), analog digital converter, and computer to collect and analyze the data. There are many high performance CFDs and TACs available as NIM modules from companies like Ortec. The fast photodiode monitors the laser pulses that excite the sample, which we call the sync. The emission from the sample is then detected by the single photon detector that generates electronic pulses which are time-correlated with the detection time of the photon. These pulses are sent over coaxial cable to a CFD which effectively normalizes the amplitude of the pulse, since this amplitude varies from run to run. The normalized pulses go to

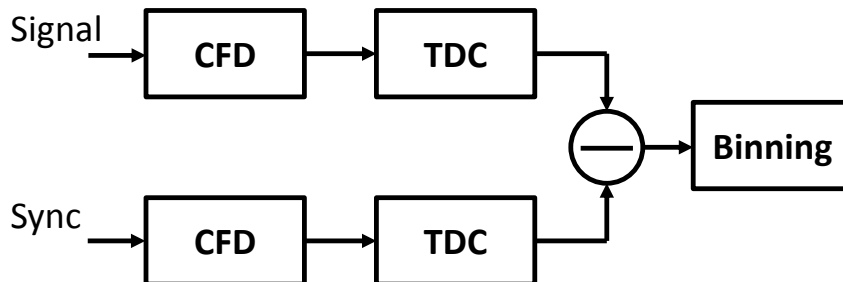


Figure 4.3: Instead of a traditional TAC, the HH400 uses independent time-to-digital converters on both the signal and sync and records the event times relative to an internal clock. These times can then be subtracted digitally to perform a traditional start-stop TCSPC measurement.

the “start” input of the TAC. An edge of the electric pulse triggers the TAC, which linearly ramps a voltage until the edge of a “stop” pulse from the sync stops the ramping. The final voltage is a measure of the relative time between the excitation pulse and the single photon detection event. These values are digitized and recorded over many cycles by a computer which time bins the events to build a histogram. Like the single photon detector, the TAC electronics also have a reset time, which is usually on the order of $1 \mu\text{s}$. Time delays are usually inserted by delay generators or simply by introducing additional lengths of coaxial cable. Most electrical components are impedance matched to the 50Ω standard, and usually use BNC, LEMO, or SMA connectors. The most common coaxial cable is RG-58/U which is a 50Ω cable.

In this work, we use a Picoquant HydraHarp 400 (HH400) model multichannel picosecond event timer for TCSPC measurements. This instrument is based on a modern approach replaces the TAC with time-to-digital converters (TDCs) that independently measure the event times relative to an internal clock. The signal event (start) and the sync (stop) each have their own CFD and TDC so the events can be “time-tagged.” To perform a traditional TCSPC measurement, the difference be-

tween the start and stop is calculated digitally and then time binned (Figure 4.3). The time-tagging allows for correlations between different experimental runs to be measured, and the independent channels gives the flexibility to scale the system to multiple input channels [83]. This digital approach also allows for improved linearity and long term stability over analog TACs. An additional benefit of this method is that arbitrary time delays can be inserted digitally instead of requiring external delay boxes or cables. The inputs of the instrument are 50Ω terminated and designed to measure standard -800 mV NIM pulses. All input channels have independent CFDs. There are two timing inputs and one “sync” channel, which is usually used to measure the excitation laser pulse train, but all three channels can be used as timing channels if desired. The instrument triggers on the falling edge of the pulse and accepts pulses 0.5-30 ns in width and requires the pulse rise/fall time to be less than 2 ns. The timing resolution of the TDCs is < 12 ps RMS, the reset time is < 80 ns, and the maximum count rate is 12.5×10^6 cps. The instrument has several modes of operation. In this Chapter 5, we will use the HH400 in “integration” mode to bin counts as a function of time relative to the excitation pulse, and “T2” mode where the detection events from two channels are time-tagged. For the spin-photon entanglement experiment in Chapter 7, the “T3” mode is used, which utilizes the HH400’s multichannel capability to time-tag events from two independent channels relative the excitation pulse, requiring all three channels.

4.2 Generating Fast Optical Pulses with Electro-Optic Modulators

The lifetime of the optically excited QD trion state is approximately 1 ns. In order to observe the transient response of the QD, the QD must be excited with optical pulse short compared to this lifetime. These pulses are typically generated by a pulsed laser such as a mode-locked Ti:sapphire laser which outputs short pulses in the range of $\approx 0.1 - 100$ ps at a repetition rate of $\approx 70 - 100$ MHz. For the Coherent MIRA laser used in later chapters, the laser is operated in the picosecond mode putting out ≈ 2 (autocorrelation intensity width 2 – 3 ps) pulses at 950 nm

with a repetition rate of 76.5 MHz. Assuming a hyperbolic secant squared pulse shape, these pulses have approximately 156 GHz (0.65 meV) of bandwidth. For many quantum information application of QDs, multiple tailored laser pulses are used to spectrally address specific transitions that can be as close as 2 – 3 GHz, requiring narrow bandwidth optical pulses with stable center frequencies. Narrow bandwidth pulses could be generated by splitting a short pulse (large bandwidth) into several paths and using optical pulse shaping (diffraction gratings or etalons) to generate different pulse widths at different center frequencies. These shaped pulses could then be delayed relative to each other using mechanical delay lines, and recombined to form the various required pulse sequence. This technique has the advantage that one laser can potentially generate all the required pulses, but it requires significant optical complexity, and one is limited to the 156 GHz bandwidth of the source pulse.

In this work, we take a different approach. Instead of filtering a short picosecond pulse, we begin with a narrow bandwidth cw laser, and then time gate this laser with a high speed electro-optic modulator (EOM). The cw field could be generated by a cw Ti:sapphire ring laser or a narrow bandwidth diode laser.

The EOMs used here are intensity modulators from EOSPACE, which vary the intensity of transmitted light as a function of an applied voltage. They are based on the strong electro-optic response of lithium niobate (LiNbO_3), where a voltage across the crystal changes the index of refraction, allowing for phase modulation of a transmitted field. The EOM is a monolithic waveguide structure that forms a Mach-Zehnder interferometer (Figure 4.4). Light is coupled into the EOM with a polarization maintaining (PM) single mode fiber with the polarization aligned to the fiber’s slow axis (usually aligned with the notch on the FC/APC connector). We use high polarization contrast ratio (25 dB) PM850 (Panda) fiber from OZ Optics (part number: PMJ-3A3A-850-5/125-3-3-1-ER=25). The light coupled into the EOM is then split into two arms with a Y-junction. The phase applied to the field in one (or both) of the arms is controlled by the voltage to the device. The two paths are recombined with another Y-junction and passed through an integrated polarizer which improves the modulator performance by rejecting the unwanted polarization.

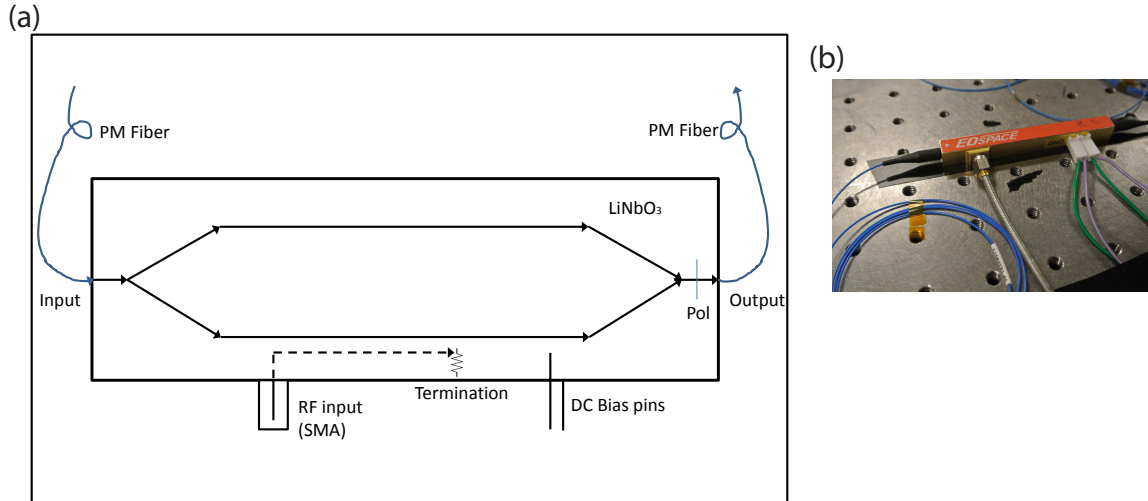


Figure 4.4: (a) A simplified diagram of a waveguide LiNbO_3 EOM. Light is coupled into the device with a PM fiber. The black lines with arrows show the optical path through the monolithic LiNbO_3 structure. The light is split with a Y-junction into two paths. By applying an external voltage the phase imparted to the optical field in one arm can be varied relative to the other. The light in two paths is recombined, filtered with a polarizer and coupled out to another PM fiber. The dashed line shows the RF strip line that couples the traveling wave voltage through the device in the same direction as the propagating optical field. The simplified device depicted here is similar to a z-cut design, where the RF voltage mostly drives one arm (lower). In an x-cut device, the RF is coupled down the center of the device and drives the two arms anti-symmetrically. (b) A photograph of a z-cut EOM used in this work, showing the PM fibers, the RF input and DC bias pins. The device is about the size of a pencil.

The light is coupled out of the modulator and into another PM fiber. By applying a time dependent voltage to the EOM, one can generate arbitrary optical intensity waveforms.

There are two common configurations of these intensity modulators which are named based off the direction of the (LiNbO_3) crystal axis: x-cut and z-cut. x-cut modulators are commonly used for long distance communications at telecom wavelengths. The x-cut design allows for phase modulation of both arms, which results in the ability to generate optical pulses with minimal (almost zero) chirp. x-cut modulators can be designed for operation at the QD wavelength (typically 950 nm), however, the photorefractive effect at this wavelength severely limits their usefulness

as it dramatically reduces the modulation contrast for even low (1 mW) input powers. This photorefractive “damage” comes from long lived photo-excited charges that get trapped in the LiNbO₃. The device can recover from this photorefractive damage by slowly cycling the EOM between 50 – 60 C and room temperature a few times. The EOM can be permanently damaged if high power is accidentally coupled into the device along the wrong polarization axis mostly because the integrated polarizer is absorptive. Because of the low power handling and contrast performance of the x-cut modulators, in later chapters, we utilize z-cut EOMs, which are able to achieve high contrast modulation for much higher input powers (10-20 mW). However, in a z-cut EOM, the phase modulation is mostly applied to one arm of the Mach-Zehnder as depicted in Figure 4.4. This asymmetric phase modulation gives rise to a chirp in the intensity modulated output. To understand the origin of the chirp, we review the basic theory of EOM operation following the analysis in *Rogers et al.* [84].

The external voltage $V(t)$ applied to the modulator is an RF traveling wave that is coupled into the modulator with an SMA connector. This traveling wave voltage propagates along the waveguide structure modulating the LiNbO₃ index and is terminated on the end of the EOM with a resistor. Depending on the design of the EOM, the applied voltage can partially phase modulate both arms of the EOM. We start by defining a voltage-to-phase parameter for each of the two arms of the EOM, β_1 and β_2 . Now, the transmitted optical field is the sum of the fields from the two arms which has the form [84],

$$E(t) = E_1(t) + E_2(t) = \frac{1}{2}E_0 \left(e^{i[\omega t + \beta_1 V(t) + \phi_1]} + e^{i[\omega t + \beta_2 V(t) + \phi_2]} \right), \quad (4.1)$$

where ω is the optical frequency, ϕ_1 and ϕ_2 are the DC phases of the two arms, and E_0 is the input amplitude. An external DC bias is applied to the device using to set the state phase difference $\phi_1 - \phi_2$. The total time dependent output phase $\phi(t)$ is given by [84],

$$\phi(t) = \frac{1}{2} ((\beta_1 V(t) + \phi_1) + (\beta_2 V(t) + \phi_2)), \quad (4.2)$$

and the output phase difference is

$$\Delta\phi(t) = \frac{1}{2} ((\beta_1 V(t) + \phi_1) - (\beta_2 V(t) + \phi_2)), \quad (4.3)$$

which allows us to re-write the output field as,

$$E(t) = E_0 \cos(\Delta\phi(t)) e^{i(\omega t + \phi(t))}. \quad (4.4)$$

We find that the output power is therefore,

$$P(t) = P_0 \cos^2(\Delta\phi(t)). \quad (4.5)$$

where $P_0 \propto I_0 = \frac{1}{2} n \epsilon_0 c |E_0|^2$. We see that as $\Delta\phi$ is varied from 0 to $\pi/2$, we can achieve intensity modulation, and we define this voltage as $V_\pi = \pi(\beta_1 - \beta_2)$, which is typically on order of 1.5 – 4 V. Due to insertion loss and other losses in the EOM, for a given input power P_{in} , there is a lower maximum output power P_{max} . For the z-cut devices, $P_{max} \approx 0.25 \times P_{in}$; and for the x-cut, $P_{max} \approx 0.1 \times P_{in}$.

As mentioned earlier, the DC bias sets the static phase difference between the two arms of the EOM, which establishes the operating point of the EOM see Figure 4.5. Typically, we set the EOM to minimize the output power with the DC voltage, and then apply RF via the SMA connector to perform intensity modulation. Unfortunately, this DC set point drifts in time due to charges that accumulate in the modulator, so the DC voltage has to be continually adjusted to keep the transmission minimized. This is performed by sampling part of the EOM output with a photodiode and using a feedback controller to maintain the lock. Since we are locking to a minimum, this is accomplished by applying a small AC dither voltage (typically 1 kHz) to the DC voltage pins, which can be detected with a lockin amplifier before it is fed into the input of an integrating feedback controller. The output of the feedback controller is summed with the set voltage and applied to the DC input pins of the EOM. Integrated circuit boards are available from YY Labs, Inc (Fremont, CA) that are specifically designed to lock these EOMs. YY Labs models, mini-MBC-3 and mini-MBC-4 are used to lock the x-cut and z-cut EOMs respectively. These EOM controller boards have been customized to allow for manual fine tuning of the lock point which is crucial to achieving high pulse contrast.

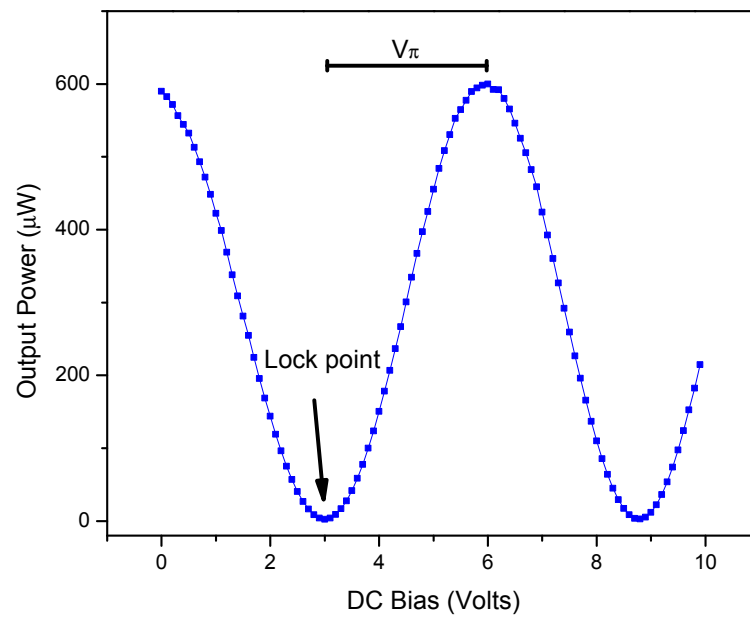


Figure 4.5: An example of the measured output power of the x-cut EOM as a function of applied DC voltage. The output varies sinusoidally as expected. The π voltage is shown, where here $V_\pi \approx 3$ V. For pulsed operation, the EOM is locked to a minimum before pulses are applied to the RF input.

The output contrast P_{max}/P_{min} is defined here as the ratio of the maximum output power to the minimum output power for the same input power P_{in} . The output contrast can be measured by monitoring the output power on a power meter while adjusting the DC voltage applied to the EOM pins (Figure 4.5). The output contrast is a very important in experiments because a low contrast results in an effective cw field leaking through the EOM. Since this cw field is always on, it can drive surprisingly large unintended dynamics by exciting the QD. In the x-cut EOM, extinction ratios of 25 dB are achievable, with 30 dB being possible over short periods (typ. 1 hour) before photo-refractive damage occurs. The z-cut modulators used in later chapters are high contrast EOMs which are capable of achieving 50 dB output contrast by utilizing an additional fine tuning pin (for a total of two DC voltages).

The fast RF voltage pulses are generated by a two-channel fast pulse generator from Picosecond Pulse Labs (Model 12010). It is capable of high repetition rate (800 MHz), fast rise/fall times (< 100 ps), pulse widths below 250 ps, and can output up to 2.5 V into 50Ω . The instrument is programable with fully adjustable pulse: width, amplitude, delay, repetition rate, or it can be externally triggered. Pulse patterns can also be programmed using software. The pulse rise time is not adjustable, so long pulses have a square shape. The electronic pulses can be shaped using external rise time filters to generate Gaussian-like pulses. An important feature of the pulse generator is that it has minimal overshoot/undershoot or ringing, and its output is very flat when the pulses are off. Some examples of electronic pulses generated with this generator are shown in Figure 4.6. The pulses are usually sent directly to the EOM with 50Ω coaxial cable. In some experiments, it is useful to split the output of the generator with an impedance matched RF splitter (Picosecond Pulse Labs model 5331), introduce temporal delay with different lengths of cable, and then recombine the pulses with a impedance matched combiner. High quality -6 dB attenuators are inserted at each input to reduce reflections. These amplitude shaped pulses must then be amplified with a Picosecond Pulse Labs model 8001 (12 GHz bandwidth) amplifier before they are sent to the input of the EOM.

Typically, we are interested in generating ≈ 1 ns pulses at a repetition rate of ≈ 76

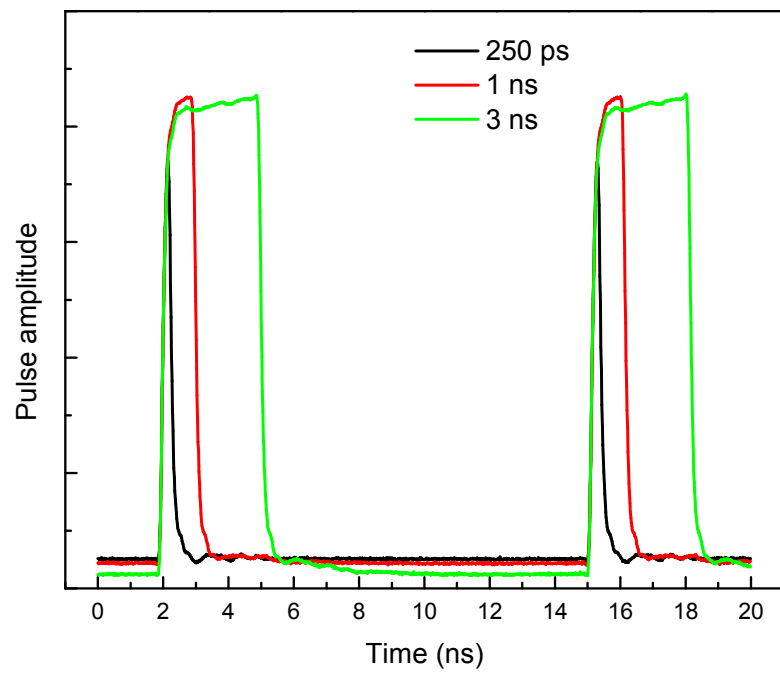


Figure 4.6: Examples of fast electronic pulses used to modulate the EOMs, showing three different pulse widths. The pulses are measured with an Agilent 86100a wide bandwidth oscilloscope.

MHz with the EOMs. The z-cut modulators can handle 10 – 20 mW of (950 nm) input power without any sign of photorefractive damage, which exhibits itself most prominently as a degradation of the EOM’s contrast ratio. A small amount (1 – 5%) of the EOM’s output is sampled with a beam splitter and sent to a photodiode in the YY Labs controller. The high contrast YY Labs controller for the z-cut modulator has two photodiodes with different sensitivities which must be balanced properly to achieve optimal performance. The control box searches for a minimum by varying the bias of the EOM’s DC pins. Once this DC lock point is found, pulses can be applied to the RF input (SMA jack) of the modulator. However, once the pulses are applied, the lock point must be tuned to maximize the pulse contrast. We can monitor these pulses with relatively high dynamic range by leaking a small amount of the light onto the PDF SPAD and using the HH400 TCSPC setup, operating in the “oscilloscope” mode. The HH400 provides a continually refreshing intensity vs. time (semi-log) plot at ≈ 1 Hz which allows us to fine tune the YY Labs controller lock point to maximize the pulse contrast. Typically, this is performed at a count rate of 10^5 cps. The afterpulsing from the PDF SPAD (3%) limits the measurable contrast ratio to ≈ 30 dB for low duty cycle pulses (250 ps at 76 MHz) and ≈ 20 dB for higher duty cycle pulses (4 ns at 76 MHz) because it contributes a false background to the TCSPC measurement (Figure 4.8). However, by carefully maximizing the pulse contrast using this method, we reliably achieve contrast ratios near the EOM’s limit. This can be verified by measuring the QD’s time resolved emission signal, since the nonlinear response of the QD can be used to effectively increase the dynamic range of the measurement.

As mentioned earlier, an important feature of the z-cut modulator is that its output has a chirp. From Equations 4.1 and 4.2, we can see that the time dependent phase gives rise to this chirp (time-dependent frequency) where [84],

$$\omega(t) = \frac{d\phi(t)}{dt} = \frac{1}{2}(\beta_1 + \beta_2)\frac{dV(t)}{dt}. \quad (4.6)$$

We see that this is proportional to the rate of change of the voltage and the relative values of β_1 and β_2 . For an x-cut modulator design, $\beta_1 \approx -\beta_2$, so there is essentially

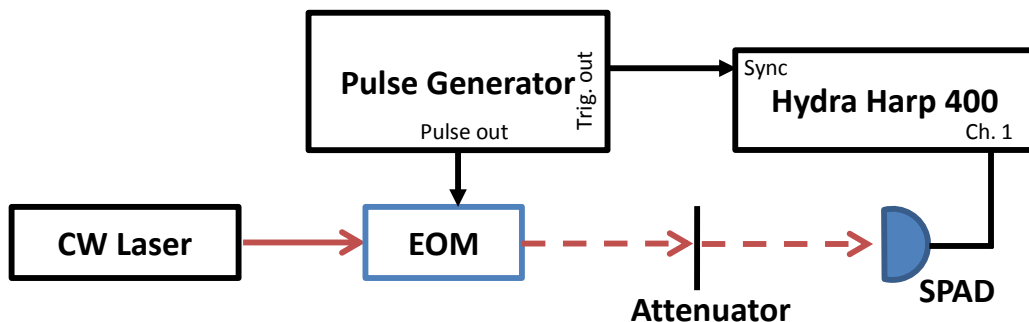


Figure 4.7: The SPAD and TCSPC setup are used to measure the EOM generated pulses and maximize the EOM pulse output contrast. The pulses are attenuated so that the average count rate of the detector is $\approx 10^5$.

zero chirp. However, for a standard z-cut design, $\beta_1 \neq -\beta_2$, which results in a nonzero chirp. This is characterized by the “ α_0 chirp parameter”, such that

$$\alpha_0 = \frac{\beta_1 + \beta_2}{\beta_1 - \beta_2} \quad (4.7)$$

where for the case of an applied voltage pulse, we have

$$\omega(t) = \frac{\pi}{2} \alpha_0 \frac{1}{V_\pi} \frac{dV(t)}{dt}. \quad (4.8)$$

For the z-cut modulators used in this work, $\alpha_0 = 0.7$.

The chirp should be considered while designing experiments using the z-cut EOM generated pulses since it effectively increases the bandwidth of the optical pulse. This is potentially problematic because this bandwidth could lead to unintended excitation of other transitions. In this work, we generate square pulses with the EOM, so these instantaneous frequency components are isolated to the rise and fall of the pulse (see Figure 4.9). Given pulses have a rise time of roughly 100 ps, we can approximate the

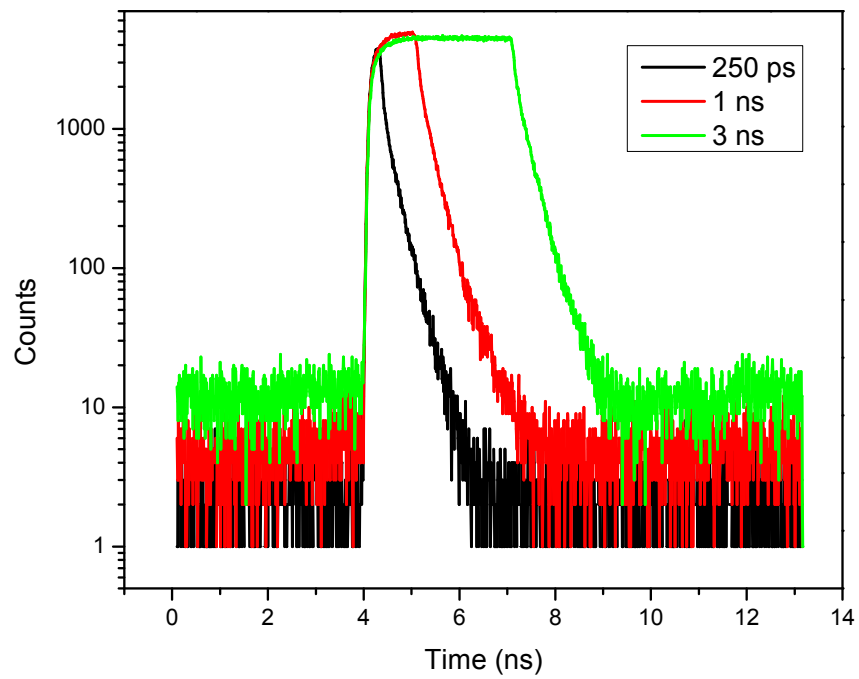


Figure 4.8: Examples of EOM generated pulses showing three different pulse widths. The observed increased background for longer pulses comes from detector afterpulsing as explained in the text.

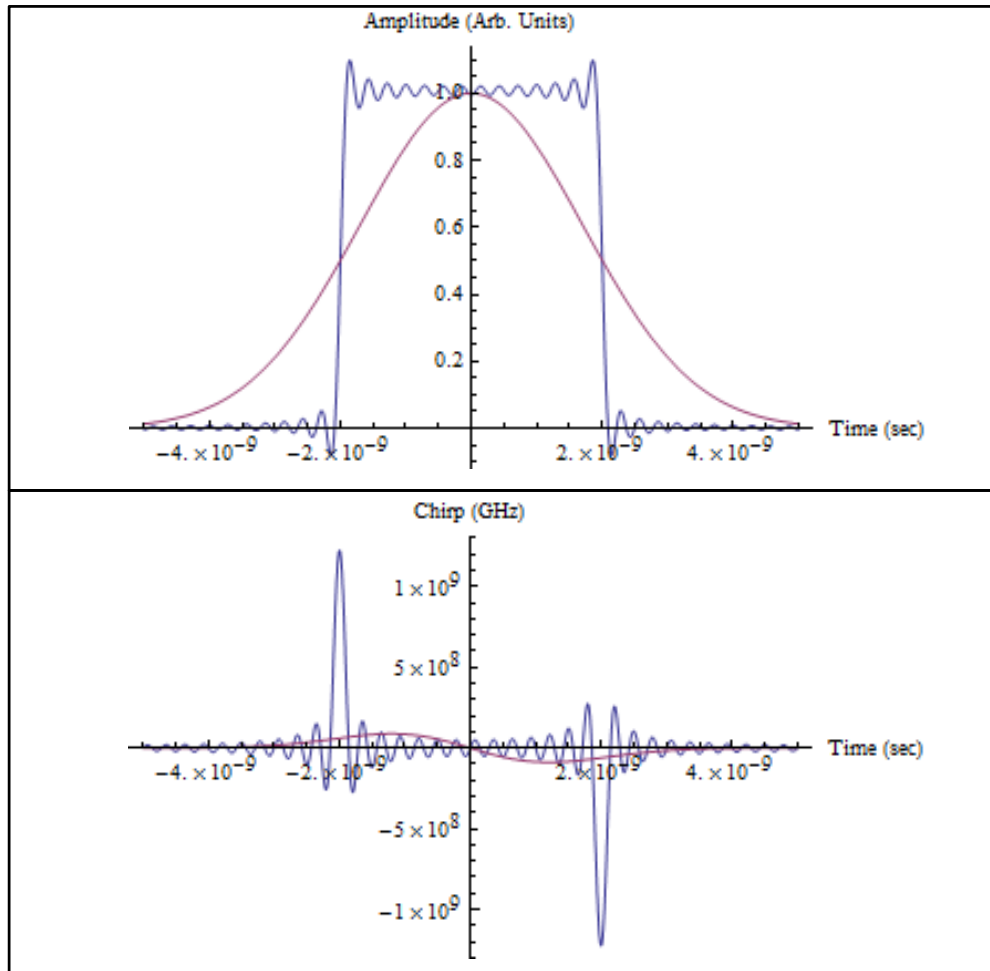


Figure 4.9: Calculated frequency chirps for 4 ns Gaussian pulse (red), and a 4 ns square pulse with 100 ps rise/fall time (blue). Since the chirp is proportional to the derivative of the voltage pulse, the chirp is most pronounced at the rise and fall of the square pulse.

maximum magnitude chirp ($\delta\omega$) as,

$$\frac{\delta\omega}{2\pi} = \frac{1}{4} \cdot 0.7 \cdot \frac{1}{100 \text{ ps}} \leq 1.75 \text{ GHz}. \quad (4.9)$$

The calculated chirps for a 4 ns Gaussian pulse and 4 ns square pulse with 100 ps rise time are shown in Figure 4.9, and we see that the maximum chirp amplitude for the square pulse is ≈ 1.2 GHz. For longer pulses, the chirp is only significant for ≈ 200 ps of the total 4 ns pulse width. Density matrix simulations of a three- and four-level system, excited by a 4 ns square chirped pulse, show that the effect that the chirp has on exciting other transitions is small (few percent) as long as the level splittings are greater than 2 – 3 GHz. For shorter pulses, ≈ 200 ps FWHM, the chirp amplitude is significant for the entire pulse, so it should be seriously considered when the pulses from the z-cut EOM are driving coherent processes like power dependent Rabi oscillations. In Chapter 5, the (zero chirp) x-cut EOM is used exclusively. In Chapters 6-7, we use the z-cut EOMs to generate a short 250 ps pulses to excite trion population, and a long 4 ns to perform optical pumping. The chirp is included in later density matrix calculations, but due to the specific applications of these pulses, the chirp does not influence the results significantly.

4.3 Chapter Summary

In this chapter, we have summarized the experimental techniques required to perform quantum optics measurements. In Chapter 5, these techniques will to be used to study the transient response of optically driven QDs and observe photon antibunching under cw excitation. The fundamentals of the TCSPC technique used in this work, and some important characteristics of single photon detectors are reviewed. The basic operational theory and application of the lithium niobate EOMs used to generate narrow bandwidth optical pulses are presented. In Chapter 7, these techniques are applied to verify a QD spin-photon entangled state, and in future, these techniques will serve as resources for implementing various quantum information applications interfacing photons and QD states.

CHAPTER 5

Transient Measurements and Quantum Optics with a Resonantly Driven Quantum Dot

Realizing a scalable optically driven QD spin architecture requires the ability to map quantum information between nodes of a QD spin network. In this work, we are pursuing an approach which utilizes intermediate photon qubits to carry quantum information between spatially distant QD spins [3, 39]. This approach requires a spin-photon interface, allowing for coherent mapping between a QD spin state and a photon state, while maintaining the ability to perform local operations on the QD spin state. In Chapter 3, we developed the capability to directly detect QD fluorescence under resonant cw excitation. We now apply the TCSPC technique and use the EOM generated optical pulses of Chapter 4 to observe the transient emission of an excited QD trion state. These techniques are applied to the two-level charged QD system to measure the trion lifetime, observe Rabi oscillations, and perform a photon anti-bunching measurement. These experiments will serve as the foundation for future quantum information applications, which are executed in the time domain.

5.1 Trion State Lifetime and Power Dependent Excitation

We begin by studying the transient fluorescence of a charged QD after it is excited by a resonant optical pulse. In this chapter, we model the QD as an effective two-level system, as described in Chapter 2. The ground state of the charged QD is defined to be the lower state with population ρ_{11} , and the optically excited trion state is defined to be the upper state with population ρ_{22} . First, the lifetime of the trion

state is measured, and then the nonlinear response under coherent pulsed excitation is verified by measuring the amplitude of the transient emission signal as a function of excitation pulse power. For convenience, we recall that the equations of motion for a two-level system in the field interaction picture, under resonant excitation $\delta = 0$, are given by,

$$\dot{\rho}_{11}(t) = -i\chi^*(t)\tilde{\rho}_{21}(t) + i\chi(t)\tilde{\rho}_{12}(t) + \gamma_2\rho_{22}(t) \quad (5.1)$$

$$\dot{\rho}_{22}(t) = i\chi^*(t)\tilde{\rho}_{21}(t) - i\chi(t)\tilde{\rho}_{12}(t) - \gamma_2\rho_{22}(t) \quad (5.2)$$

$$\dot{\tilde{\rho}}_{12}(t) = -\gamma\tilde{\rho}_{12}(t) - i\chi^*(t)[\rho_{22}(t) - \rho_{11}(t)] \quad (5.3)$$

$$\dot{\tilde{\rho}}_{21}(t) = -\gamma\tilde{\rho}_{21}(t) + i\chi(t)[\rho_{22}(t) - \rho_{11}(t)], \quad (5.4)$$

where γ is the decoherence rate, γ_2 is the excited state decay rate, and $\chi(t) = \Omega_0(t)/2$ is half of the time dependent Rabi frequency. The spontaneous emission (for a homogenous medium) rate is,

$$\gamma_2 = \frac{\omega^3 n |\mu|^2}{3\pi\epsilon_0 \hbar c^3}, \quad (5.5)$$

where ω is the transition frequency, n is the index, and μ is the transition dipole moment. From previous measurements, the lifetime of the trion state is known to be ≈ 1 ns [85], which is consistent with a dipole moment of ≈ 25 D (Debye), where $1\text{D} \approx 3.34 \times 10^{-30}$ C m.

Trion lifetime measurements are performed by exciting the system with resonant pulses which are shorter than the expected 1 ns lifetime. We indirectly measure the emission intensity as a function of time using the TCSPC method described in Chapter 4. Since we are directly detecting the signal, the emission intensity is proportional to the excited state population ($Intensity(t) \propto \rho_{22}(t)$). Specifically, we consider a step-wise excitation pulse of the form,

$$\chi(t) = \chi_0[\Theta(t) - \Theta(t - t_0)] \quad (5.6)$$

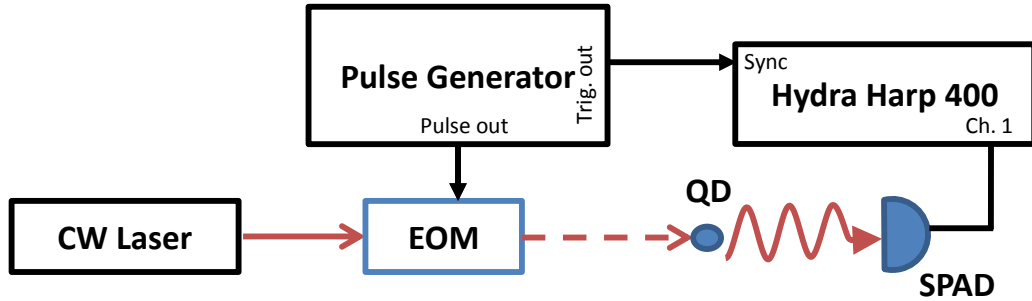


Figure 5.1: The TCSPC setup used to perform transient measurements on the charged QD under pulsed excitation. Optical pulses are generated by an EOM which temporally gates a cw laser. Light from the QD is detected by a fast SPAD, and events are recorded using the HH400 picosecond event timer operating in integration mode. The excitation pulses are rejected using the cross polarization-fiber setup described in Chapter 3.

where the step function ($\Theta(t)$) forms a pulse which is “on” from $t = 0$ to $t = t_0$. So that for times after the excitation pulse has passed, $\chi(t) = 0$, and we find

$$\rho_{22}(t) = \rho_{22}(t_0)e^{-\gamma_2(t-t_0)}, \quad (5.7)$$

which is the the expected exponential decay. A formal relationship between the emission intensity to the excited state population can be derived using the source-field approach [68] which we use later in Section 5.3.

The time resolved fluorescence is recorded using the TCSPC setup shown in Figure 5.1. The excitation pulses are generated by an x-cut EOM temporally gating a cw Ti:sapphire laser (Coherent 899-21). The laser is tuned on resonance (10539.85 cm^{-1}) by maximizing the cw fluorescence signal counts before pulses are generated. Here, horizontally polarized 250 ps pulses excite the trion population, and we use the cross polarization-fiber setup described in Chapter 3 to separate the QD emission from

the excitation pulses. The QD emission is detected with the fast SPAD (MPD-PDF model) with timing jitter ≈ 48 ps. The experiment is performed at a repetition rate of 76 MHz, set by the pulse generator. Photon detection events are recorded with the (HH400) picosecond event timer relative to the sync signal of the pulse generator. The HH400 is operated in integration mode which time bins the detection events.

The semi-classical theory of a coherently driven two-level system is well established [68,86]. In the limit of a strong resonant cw driving field and no decay, the system undergoes Rabi oscillations where the excited state population is,

$$\rho_{22}(t) = \sin^2\left(\frac{\Omega_0 t}{2}\right). \quad (5.8)$$

where we see that the excited state population oscillates in time at the Rabi frequency $\Omega_0 = \mu E_0 / \hbar$.

Rabi oscillations are useful in quantum information applications because they can be used to coherently manipulate the state, serving to rotate the qubit. In order to perform the rotation rapidly, the Rabi oscillations are usually driven with short pulses of fixed pulse width [27,85,87]. From Equation 5.8, we see that Rabi oscillations can also be observed for a fixed pulse width by varying the Rabi frequency, which is proportional to the square root of the applied pulse power.

We now estimate the pulse power required to excite a significant trion population ($\rho_{22}(t_0) \approx 1$). We recall that the pulse area (A), is given by,

$$A = \int_{-\infty}^{\infty} \Omega_0(t) dt \quad (5.9)$$

Assuming a square pulse with width (τ_p),

$$A = \Omega_0 \times \tau_p = \frac{\mu E_0}{\hbar} \tau_p, \quad (5.10)$$

we can find required pulse amplitude to achieve a π rotation ($\rho_{22}(t_0) = 1$), assuming $\mu \approx 25$ D

$$E_0 = \frac{\pi \hbar}{\mu \tau_p} \approx 15.9 \text{ kV/m}, \quad (5.11)$$

for $\tau_p = 250$ ps, which corresponds to a peak intensity of

$$I_0 = \frac{1}{2} n \epsilon_0 c |E_0|^2 \approx 1.2 \times 10^6 \text{ W/m}^2, \quad (5.12)$$

for ≈ 3.5 . Given that the focussed laser beam diameter is estimated to be $\approx 2\mu\text{m}$ on the sample, the required peak power is $P_0 \approx 3.7 \times 10^{-6}$ W. For a 250 ps pulse at 76 MHz repetition rate, this yields an average power of $P_{av} \approx 70$ nW. In practice, the π -power is determined experimentally by measuring the fluorescence signal amplitude as a function of pulse power (see Figure 5.4), but this provides a starting place for the experiments.

In order to estimate the magnitude of the emission signal, we have to consider the repetition period ($T_{rep} = 13.2$ ns), the integration time ($T_{int} = 120$ s), the detection efficiency ($\eta = 5 \times 10^{-6}$), and the bin size ($T_{bin} = 8$ ps), which spreads the counts over the lifetime ($1/\gamma_2 \approx 1$ ns). The repetition period is sufficiently long so that we can assume that each run of the experiment is independent. The time bin size is usually chosen to be a few times smaller than the timing resolution of the TCSPC setup. The integration time is chosen to obtain reasonably high signal to noise. Since this is a photon counting experiment, the noise should follow a Poisson distribution, where for each time bin, we have N counts with a standard deviation of $\pm\sqrt{N}$. If we assume that the excitation pulse, fully drives the system to the excited state ($\rho_{22}(t_0) \approx 1$), then the average number of counts per time bin is given by,

$$\text{Counts per time bin} \approx \eta \frac{1}{T_{rep}} \frac{T_{bin}}{1/\gamma_2} T_{int}. \quad (5.13)$$

which results in approximately 360 counts per time bin using the numbers above. The corresponding statistical signal-to-noise ratio (SNR) is approximately 19:1 per time bin.

The raw data for typical trion fluorescence signal is shown in Figure 5.2 and is in good agreement with the predicted exponential profile and signal level. Since the lifetime (640 ps) is much longer than the systems timing resolution (48 ps), deconvolution with the instrument response function is not necessary. By (Stark) tuning the QD transition off resonance with the excitation laser using the sample bias, a background measurement is recorded which shows the baseline. The background includes dark counts and the residual excitation pulse leak through which is not fully rejected by the polarizer/fiber setup. The ratio of the integrated signal to background

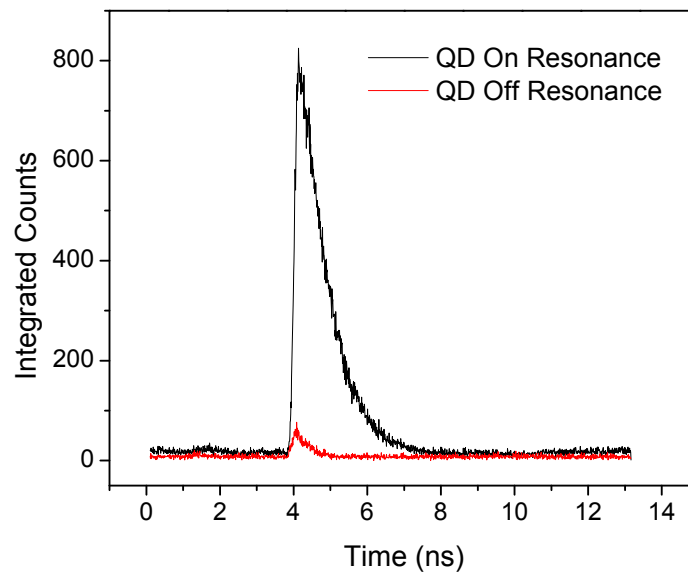


Figure 5.2: Time resolved QD emission under 250 ps pulse excitation with an integration time of 2 minutes. The black shows the signal when the QD is tuned onto resonance with the laser pulse using the DC-Stark effect. The red is the background level when the QD is tuned off resonance, showing the residual excitation pulse leaking onto the detector around 4.1 ns.

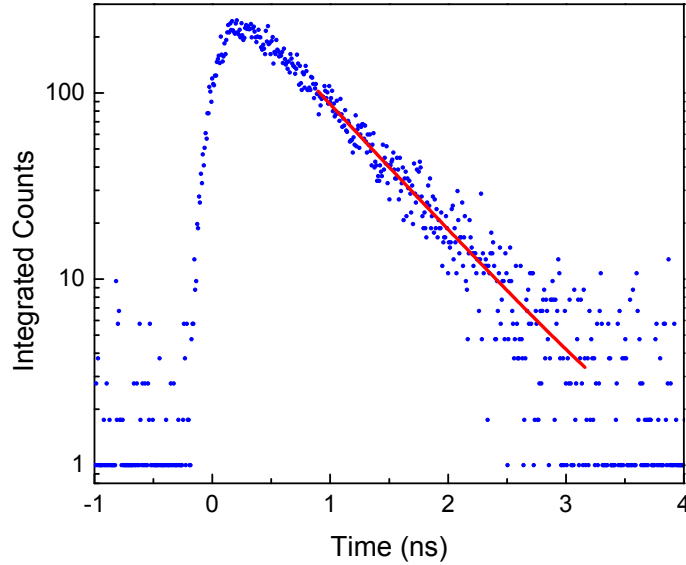


Figure 5.3: The QD emission (blue) following the 250 ps excitation pulse is fit with a single exponential decay function (red) to obtain a trion lifetime of $1/\gamma_2 = 640 \pm 25$ ps.

in the 3 ns to 6 ns time window is approximately 20:1, indicating that if a photon is measured in this window, there is a 95% probability that it is QD emission. For the remainder of this chapter, the off resonant background is subtracted from the fluorescence signal. To observe the single exponential nature of the QD emission after the excitation pulse, the data is plotted on a semi-log scale (Figure 5.3). The data are background subtracted, all values less than 1 are set to 1, and a single exponential is fit to the data. For this QD, the trion lifetime is found to be $1/\gamma_2 = 640 \pm 25$ ps.

In order to verify the nonlinear nature of the QD, time-resolved QD fluorescence measurements are performed as a function of excitation power. We fit to a section of the emission signal after the excitation pulse, and use this as a measure of the excited state population at $t = t_0$. We are able to observe the onset of power dependent Rabi oscillations (Figure 5.4), which scale properly with the square root of the pulse power. The measurement yields a π -power of $P_{inc} = 40 \mu\text{W}$ (average power of 760 nW), where these are the incident powers measured in front of the cryostat. Taking into account the transmission through the cryostat windows and sample, we estimate

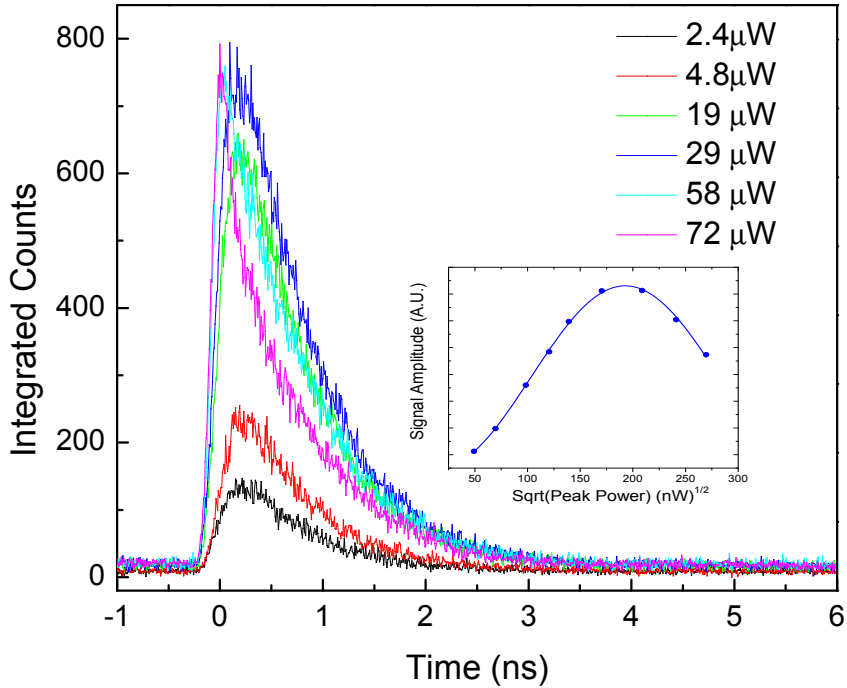


Figure 5.4: Transient fluorescence under 250 ps excitation for six different excitation powers. The onset of power dependent Rabi oscillations shows the nonlinear optical response of the QD. The inset shows the signal amplitude as a function of the square root of the power. The signal amplitudes are measured for nine different powers by integrating the fluorescence counts from 1 ns to 3 ns, after the excitation pulse has passed.

that the peak power incident on the QD is $\approx 10.8 \mu\text{W}$.

The experimentally determined π -power indicates that the trion dipole moment is approximately 15 D, which is about a factor of two smaller than the predicted dipole moment from the decay rate (Equation 5.5). It should be noted that the value for focussed laser beam diameter ($2 \mu\text{m}$) used to calculate the Rabi frequency is only an estimate and could be the source of a systematic error. It should also be noted that in the calculation of the spontaneous emission rate (Equation 5.5), the photon density of states is assumed to be spatially homogeneous, which is only an approximation for a QD within a GaAs heterostructure, and could explain the discrepancy. Since the π -power can be measured, we use the experimentally obtained values for the remainder

of this work.

5.2 Time Dependent Rabi Oscillations

In the previous section, the QD is driven with resonant 250 ps pulses which are shorter than the excited state lifetime. Using these pulses, the trion lifetime is determined, and the onset of power dependent Rabi oscillations is observed. Since the optical pulses are generated by EOMs, the pulse width can be increased to generate square pulses of controllable width (see Chapter 4). Using these square pulses, we are able to observe Rabi oscillations as a function of time by temporally resolving the trion fluorescence using the TCSPC setup [88]. Since the fluorescence intensity is proportional to the excited state population, the measurement shows that the excited state population undergoes real time dependent oscillations that are not destroyed by decoherence. Using this method, the Rabi frequency of an applied pulse can be determined with a single 1 – 2 minute measurement. By using the lifetime extracted from the short pulse measurements, one can determine the decoherence rate of the optical transition. Similar oscillations can be observed under cw excitation by performing correlation ($g^{(2)}(\tau)$) measurements on the resonance fluorescence from a single QD [66]; however, since they are second order intensity correlation experiments, they are experimentally demanding since the success rate scales like the detection efficiency squared which is usually much less than 1.

If a system starts in its ground state $\rho_{11}(0) = 1$, the excited state population of a resonantly driven two-level system is given by the Rabi solution (Equation 5.8) in the absence of decay. If decay is included, analytic solutions to the density matrix equations of motion can still be found if the system is driven on resonance [86, 89]. The excited state population is given by,

$$\rho_{22}(t) = \frac{\Omega_0^2/2}{\Omega_0^2 + \gamma\gamma_2} \left(1 - [\cos(\lambda t) + \frac{\gamma + \gamma_2}{2\lambda} \sin(\lambda t)] e^{-\frac{1}{2}(\gamma + \gamma_2)t} \right), \quad (5.14)$$

where

$$\lambda = \sqrt{\Omega_0^2 - \frac{(\gamma - \gamma_2)^2}{4}}, \quad (5.15)$$

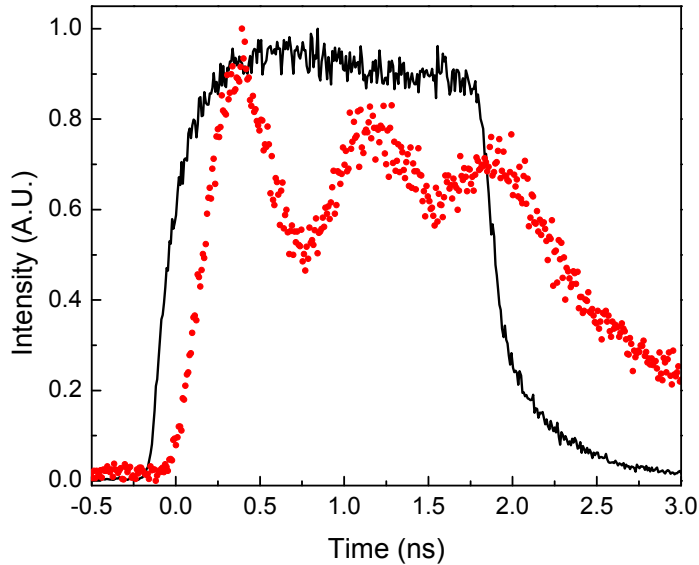


Figure 5.5: Normalized QD fluorescence under resonant 2 ns square pulse excitation is shown in red. The black trace shows the excitation pulse measured by the TCSPC setup leaking a small amount of the excitation pulse onto the detector. In both cases, the raw data are plotted so they are convolved with the SPAD’s instrument response function.

recalling that γ is the decoherence rate and γ_2 is the excited state decay rate. We are able to see that the excited state population has two terms oscillating at λ with different weights that are out of phase. The oscillations are damped with an exponential envelope whose decay rate is the average of the decoherence rate and the population decay rate. Even though this result is well known [86,89], it might be somewhat non-intuitive. To understand the physics, it is useful to consider the Bloch sphere picture of a driven two-level system. The Bloch vector begins pointing along the negative z -axis. When a driving field is turned on, the Bloch vector begins oscillating about the x -axis, spending equal time along the y - and z -axis which decay with rates γ and γ_2 respectively.

Experiments are performed on the same QD trion state as in Section 5.1 and using the same TCSPC setup. By increasing the pulse width to 2 ns, we are able to obtain a measure of the excited state population and observe the time dependent

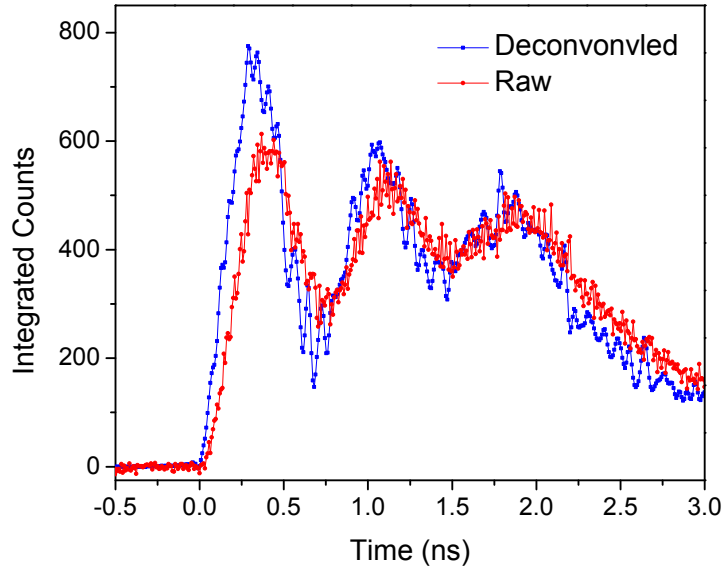


Figure 5.6: The raw data (red) is deconvolved with the setup’s instrument response function to give the deconvolved signal (blue). The high frequency oscillations present in the deconvolved data are an artifact from the deconvolution.

Rabi oscillations (Figures 5.5,5.7). We again use the fast SPAD with 48 ps timing resolution, as in Section 5.1, but since we now are interested in Rabi oscillations that can evolve faster than the excited state decay lifetime (640 ps), the signal must be deconvolved with the instrument response function (see Chapter 4). The deconvolution is performed with a standard linear deconvolution package using Tikhonov regularization [90]. An example of the (background subtracted) raw data and the deconvolved data are shown in Figure 5.6.

From Equation 5.14, we see that the $\rho_{22}(t)$ is dependent on the Rabi frequency, the decoherence rate and the population decay rate. By fitting the deconvolved data to Equation 5.14 and using the (640 ps) lifetime determined by short pulse measurements, we can extract the decoherence rate γ and Rabi frequency (Ω_0), which are the only two physical fitting parameters. The fits are convolved with the system’s IRF and plotted with the raw (background subtracted) data. The measurement is repeated for seven excitation powers, four of which are shown in Figure 5.7.

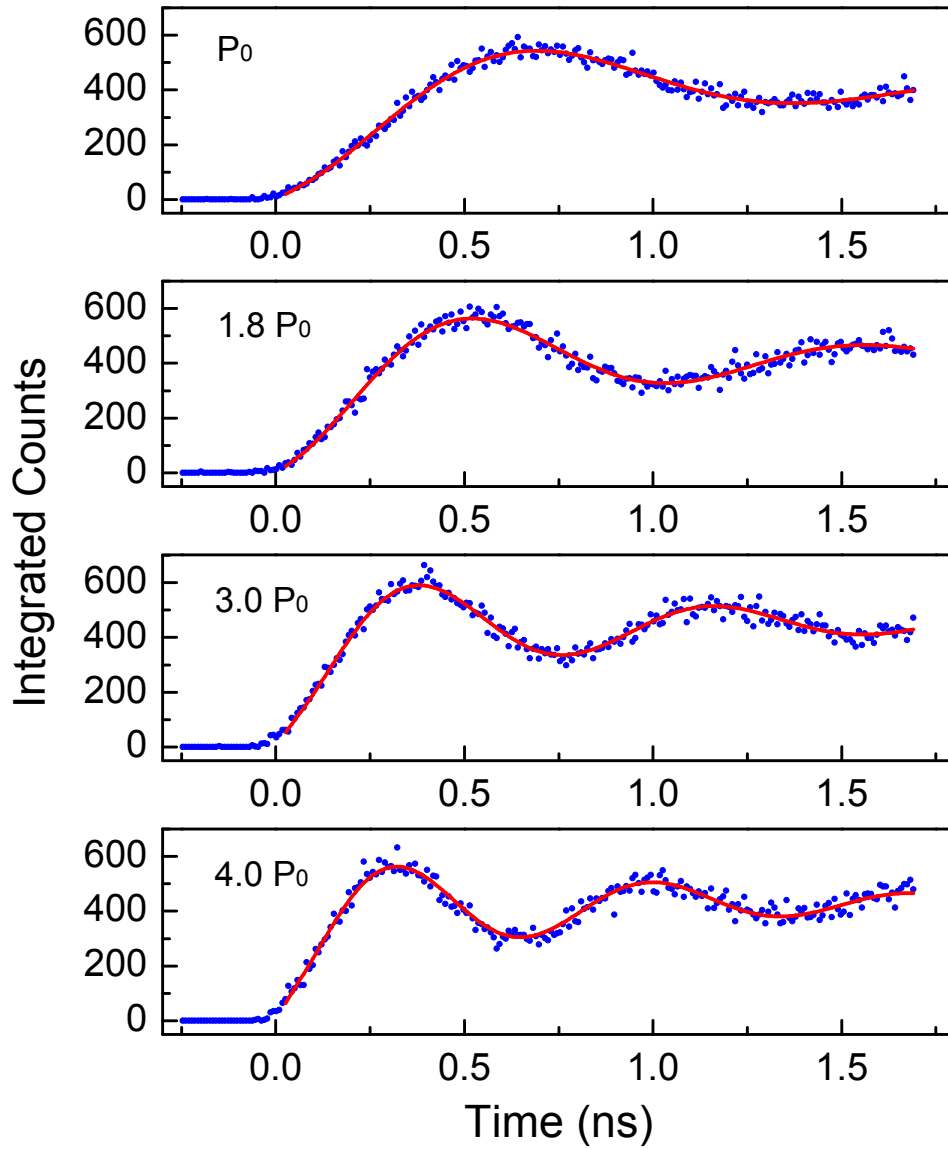


Figure 5.7: Time-dependent Rabi oscillations for four different excitation powers, plotted with the convolved fits of Equation 5.14 in red. P_0 corresponds to a peak power of approximately $3.4 \mu\text{W}$.

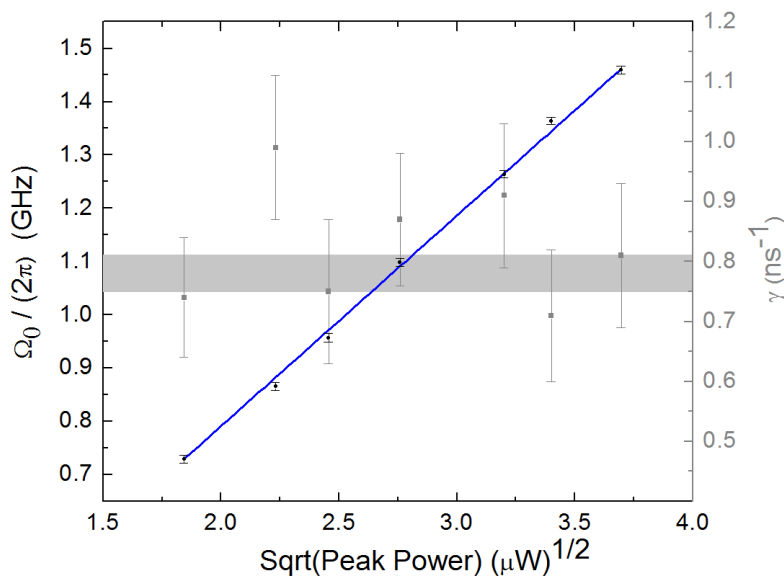


Figure 5.8: Black: The Rabi frequency scales linearly with the square root of the excitation power as expected. Grey: The decoherence rate is also plotted against the square root of the excitation power, showing no sign of excitation induced dephasing. The grey bar shows the ideal case of $\gamma = \frac{1}{2}\gamma_2$ calculated from the $1/\gamma_2 = 640 \pm 25$ ps, where the thickness of the bar shows the error.

The Rabi frequencies scale with the square root of the excitation power as expected from theory, and indicate a trion dipole moment of 17 D which is relatively consistent with the short pulse measurements (15 D). The extracted decoherence rates and Rabi frequencies for all seven powers are shown in Figure 5.8.

Averaging over the seven measurements, the decoherence rate is found to be $1/\gamma = 1.22 \pm 0.06$ ns, which is in good agreement with the theoretical prediction, $\gamma = \frac{1}{2}\gamma_2$, for the case of pure dephasing. This result is somewhat surprising because cw spectra from single InAs QDs typically exhibit homogenous absorption (and fluorescence intensity) linewidths of 500 – 600 MHz indicating a faster decoherence rate. For the QD studied in this chapter, the low power linewidth is 623 ± 25 MHz FWHM (Figure 5.9), which implies a decoherence time of $1/\gamma = 1/(\pi 623 \text{ MHz}) = 511 \pm 21$ ps. We attribute this line broadening to a spectral wandering process arising from fluctuations of the QD’s nuclear spin bath [91–93]. Our result that, $\gamma \approx \frac{1}{2}\gamma_2$ is

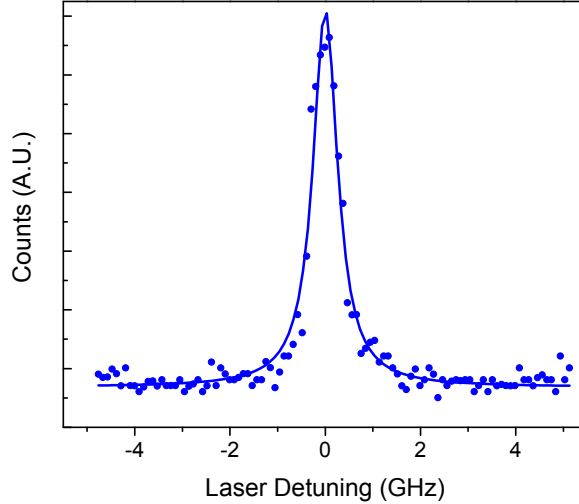


Figure 5.9: The cw QD fluorescence intensity as a function of the QD-laser detuning in the low power limit. The Lorentzian fit to the data gives a linewidth of 623 ± 25 MHz FWHM.

consistent with time domain studies on ensembles of InAs QDs [94], and more recent nonlinear cw measurements on a single InAs QD [95]; however, groups performing correlation measurements on QD resonance fluorescence have reported significantly faster decoherence rates [66]. In Chapter 6-7, we will use similar pulses to initialize the QD state via optical pumping and read out the spin state by scattering a single photon.

5.3 Photon Antibunching

In Chapter 3, the QD is driven with a cw field and the QD fluorescence intensity is measured as function of the laser-QD detuning. So far in this chapter, we have performed TCSPC measurements by exciting the QD with resonant laser pulses and time resolving the fluorescence intensity. We now return to using resonant cw excitation, and use the TCSPC technique to study the quantum optical properties of the QD fluorescence. Since a charged QD has been shown to form an effective two-level system, its fluorescence is expected to exhibit photon antibunching [96]. Photon antibunching refers to the zero probability of detecting two photons at the same time,

and light sources that exhibit antibunching are referred to as single photon sources. This effect was first observed in atomic resonance fluorescence by Kimble, Dagenais and Mandel in 1977 [96]. It has been well established that QDs can serve as high quality single photon sources when driven optically [87,97–99] and electrically [100].

For a single two-level atom, the antibunching effect is sometimes explained by saying that a single atom is only able to “emit” one photon at a time. This interpretation is reasonable for time domain measurements where a short pulse excites the atom to the upper state, which then decays emitting a single photon. However, resonance fluorescence from a single two-level system exhibits photon antibunching even under cw excitation, which is a steady state scattering problem. In fact, applying the absorption/emission interpretation to a cw resonance fluorescence experiment results in wrong answers about the spectral composition of the resonance fluorescence, which in the low power limit is elastic Rayleigh scattering. To better understand these effects, we review some concepts from quantum optics and the theory of photon antibunching. Finally, an antibunching experiment is performed to verify the single photon nature of the QD fluorescence studied in this work.

In the study of quantum optics, the electric field operator is written in terms of the creation (a_j^\dagger) and annihilation (a_j) operators,

$$\mathbf{E}(\mathbf{r}) = i \sum_j \sqrt{\frac{\hbar\omega_j}{2\epsilon_0 V}} \left(a_j \boldsymbol{\epsilon}_j e^{i\mathbf{k}_j \cdot \mathbf{r}} - a_j^\dagger \boldsymbol{\epsilon}_j e^{-i\mathbf{k}_j \cdot \mathbf{r}} \right), \quad (5.16)$$

where, j indexes the mode, V is the quantization volume, and the other symbols have their usual meanings, and we recall that

$$[a_j, a_k^\dagger] = \delta_{j,k}, \quad (5.17)$$

$$[a_j, a_k] = 0, \quad (5.18)$$

$$[a_j^\dagger, a_k^\dagger] = 0. \quad (5.19)$$

The field operator is often separated into components,

$$\mathbf{E}(\mathbf{r}) = \mathbf{E}^+(\mathbf{r}) + \mathbf{E}^-(\mathbf{r}), \quad (5.20)$$

such that,

$$\mathbf{E}^+(\mathbf{r}) = i \sum_j \sqrt{\frac{\hbar\omega_j}{2\epsilon_0 V}} (a_j \boldsymbol{\epsilon}_j e^{i\mathbf{k}_j \cdot \mathbf{r}}), \quad (5.21)$$

and

$$\mathbf{E}^-(\mathbf{r}) = -i \sum_j \sqrt{\frac{\hbar\omega_j}{2\epsilon_0 V}} (a_j^\dagger \boldsymbol{\epsilon}_j e^{-i\mathbf{k}_j \cdot \mathbf{r}}). \quad (5.22)$$

We recall that the Hamiltonian for the field can be written in term of the creation and annihilation operators,

$$H = \sum_j \hbar\omega_j \left(\hat{n}_j + \frac{1}{2} \right). \quad (5.23)$$

where $\hat{n}_j = a_j^\dagger a_j$ is the number operator. Fock states are eigenstates of \hat{n}_j where n_j is the occupation of mode ω_j , such that

$$\hat{n}_j |n_j\rangle = a_j^\dagger a_j |n_j\rangle = n_j |n_j\rangle, \quad (5.24)$$

and we recall that,

$$a_j^\dagger |n_j\rangle = \sqrt{n_j + 1} |n_j + 1\rangle, a_j |n_j\rangle = \sqrt{n_j} |n_j - 1\rangle. \quad (5.25)$$

Fock states represent excitations of a single mode with frequency ω_j , whose eigenenergies are,

$$E_{n,j} = \hbar\omega_j \left(n_j + \frac{1}{2} \right) \quad (5.26)$$

Since the QD is ideally a single photon source, we are interested in single photon states of the field. A single photon Fock state is generated in mode j by the creation operator acting on the vacuum $|0\rangle$,

$$|1_j\rangle = a_j^\dagger |0\rangle. \quad (5.27)$$

Fock states can be used to construct other states of the field, such a single mode coherent (Glauber) states which are often used to represent the coherent fields generated by narrow band lasers, and multimode coherent states which can be used to model laser pulses, and multimode Fock states to give a few examples.

A more general single photon state is a multimode single photon state given by,

$$|\psi(t)\rangle = \sum_j c_j(t) a_j^\dagger |0\rangle = \sum_j e^{-i\omega_j t} c_j(0) |1_j\rangle, \quad (5.28)$$

which is a good model for a single photon spontaneously emitted from a QD after it is excited by a short pulse. Recall that the lifetime of the excited QD trion state is approximately 1 ns, so a single spontaneously emitted photon is composed of many modes, giving rise to a single photon wavepacket with a 1 ns exponential temporal envelope. However, we are not using pulses to excite the QD, we are using cw excitation, where the time domain spontaneous emission picture does not apply. As mentioned earlier, resonance fluorescence from a cw driven two-level system is really a scattering problem, and we will have to use different theoretical tools to properly calculate the properties of the scattered field. To illustrate some basic properties of quantized fields, we first review some important results from quantum optical coherence theory and use a single mode single photon Fock state as a toy model for the QD fluorescence. We then apply these techniques to the problem of resonance fluorescence from a two-level system.

Recall that in the Heisenberg picture, the field operator is given by,

$$\mathbf{E}^+(\mathbf{r}, t) = i \sum_j \sqrt{\frac{\hbar\omega_j}{2\epsilon_0 V}} (a_j \boldsymbol{\epsilon}_j e^{i\mathbf{k}_j \cdot \mathbf{r} - i\omega_j t}), \quad (5.29)$$

and $\mathbf{E}^-(\mathbf{r}, t) = [\mathbf{E}^+(\mathbf{r}, t)]^\dagger$. Given a state of the field $|\psi\rangle$, the average intensity measured by a square law detector is,

$$\langle I(t) \rangle = \langle \psi | \mathbf{E}^-(\mathbf{r}, t) \cdot \mathbf{E}^+(\mathbf{r}, t) | \psi \rangle, \quad (5.30)$$

and the temporal second order intensity correlation is given by [68, 71],

$$g^{(2)}(\tau) = \frac{\langle E^-(t) E^-(t+\tau) E^+(t+\tau) E^+(t) \rangle}{\langle E^-(t) E^+(t) \rangle \langle E^-(t+\tau) E^+(t+\tau) \rangle}. \quad (5.31)$$

where we have dropped spatial coordinate and assume the field is measured at the same position.

Calculating $g^{(2)}$ for a single mode Fock state $|n\rangle$, we find

$$\begin{aligned}
g^{(2)} &= \frac{\langle n|E^- E^- E^+ E^+|n\rangle}{\langle n|E^- E^+|n\rangle^2} \\
&= \frac{\kappa^2 \langle n|a^\dagger a^\dagger a a|n\rangle}{(\kappa \langle n|a^\dagger a|n\rangle)^2} \\
&= \frac{\kappa^2 \langle n|(a^\dagger a)^2 - a^\dagger a|n\rangle}{\kappa^2 \langle n|a^\dagger a|n\rangle^2} \\
&= \frac{n^2 - n}{n^2}, \tag{5.32}
\end{aligned}$$

where κ is a constant. We see that for any Fock state, $g^{(2)} < 1$. For a single photon Fock state $n = 1$, we get antibunching ($g^{(2)} = 0$), which indicates that if one photon is measured, we cannot measure another photon. Now that we have seen that a single photon Fock state exhibits antibunching, we return to the problem of QD resonance fluorescence.

One could imagine performing second order intensity correlation measurements with a single fast photodetector capable of continually measuring $I(t)$, digitizing the output, and calculating the correlation function after the measurement. This approach is technologically difficult due to many of the same challenges that motivated the development of TCSPC techniques to measure fluorescence lifetimes (see Chapter 4). The first challenge is that the high gain timing resolving detectors required to detect single photons operate in pulsed mode, and are typically not capable of resolving the number of photons incident on the detector. The second challenge is the ≈ 50 ns detector deadtime after a detection event (“click”) and afterpulsing limits the useful temporal correlation capabilities of a single detector to times much longer than the 1 ns lifetime of a QD trion state. The traditional solution to these problems is to use two detectors and measure the temporal correlation between the detector clicks. It should be noted that new detector technologies such as superconducting nanowire detectors are causing some reevaluation of these traditional limitations on photon number resolution, dead time and afterpulsing [82, 101, 102].

Intensity correlation experiments are usually performed in a Hanbury-Brown and Twiss (HBT) type setup (Figure 5.10) [103]. The setup measures intensity correlations by first splitting the incident light with a 50-50 beam splitter, and then measuring

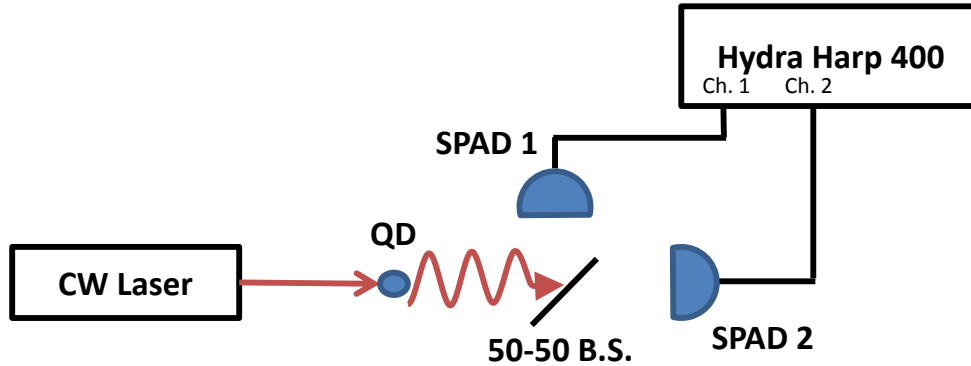


Figure 5.10: The HBT setup used to perform photon antibunching experiments on a single charged QD. A narrow bandwidth cw laser drives the charged QD. The QD resonance fluorescence is collected and sent to a 50-50 fiber beam splitter. τ -SPAD single photon detectors measure the light on the two outputs. The detection events are recorded with the HH400 picosecond event timer operating in “T2” mode.

the light in the output arms with two square-law photodetectors which are sensitive to intensity as function of time $I(t)$. HBT setups are often used in quantum optics experiments to verify that one has a single photon source. The basic idea is that if the input state is a single photon, it can only be detected by one of the detectors, so that the intensity correlation between these two detectors within a certain time window is zero. In terms of the traditional TCSPC setup described in Chapter 4, SPAD 1 is sent to the “start” and SPAD 2 is sent to the “stop” of a TAC, so that in the case of a single photon source, there are no coincidence events at zero time delay.

In the HBT setup, the detectors are at two different spatial locations, so the second order intensity correlation function is a function of space and time such that [68],

$$g^{(2)}(\mathbf{r}_1, t_1, \mathbf{r}_2, t_2) = \frac{\langle E^-(\mathbf{r}_1, t_1)E^-(\mathbf{r}_2, t_2)E^+(\mathbf{r}_2, t_2)E^+(\mathbf{r}_1, t_1) \rangle}{\langle E^-(\mathbf{r}_1, t_1)E^+(\mathbf{r}_1, t_1) \rangle \langle E^-(\mathbf{r}_2, t_2)E^+(\mathbf{r}_2, t_2) \rangle}, \quad (5.33)$$

where \mathbf{r}_1, t_1 and \mathbf{r}_2, t_2 are the space time coordinates. However, the spatial distances, and time delays can be incorporated into τ to recover $g^{(2)}(\tau)$ of Equation 5.31.

The second order intensity correlation function for resonance fluorescence, $g^{(2)}(\tau)$, is often calculated by using the quantum regression theorem [71], but first we must use an operator approach referred to as “source-field” [68], which allows us to express the quantum mechanical properties of the scattered field in terms of the quantum properties of the atomic operators. We can then calculate the second order intensity correlation function with these atomic operators. We follow the approach used in Berman and Malinkovsky [68], and Scully and Zubairy [71]. We begin with the quantized atom-field Hamiltonian for a two-level system interacting with an arbitrary number of field modes,

$$H = \frac{\hbar\omega_0}{2}\sigma_z + \sum_j \hbar\omega_j a_j^\dagger a_j + \sum_j \hbar \left(g_j \sigma_+ a_j + g_j^\dagger \sigma_- a_j^\dagger \right), \quad (5.34)$$

with

$$g_j = -i\langle 2|\boldsymbol{\mu}|1\rangle \cdot \boldsymbol{\epsilon}_j \sqrt{\frac{\omega_j}{2\hbar\epsilon_0 V}}, \quad (5.35)$$

where $\sigma_z = |2\rangle\langle 2| - |1\rangle\langle 1|$ is the population difference operator, $\sigma_+ = |2\rangle\langle 1|$, $\sigma_- = |1\rangle\langle 2|$, and ω_0 is the atomic (QD) frequency and ω_j is the field frequency.

The Heisenberg picture is used to find expressions for the time dependence of the operators: $a_j^\dagger(t)$, $a_j(t)$, $\sigma_+(t)$, and $\sigma_-(t)$. The expression for $a_j(t)$ is,

$$a_j(t) = a_j(0)e^{-i\omega_j t} - ig_j^\dagger \int_0^t \sigma_-(t')e^{-i\omega_j(t-t')} dt' \quad (5.36)$$

which can be inserted into,

$$\mathbf{E}^+(\mathbf{r}, t) = i \sum_j \sqrt{\frac{\hbar\omega_j}{2\epsilon_0 V}} \left(a_j(t) \boldsymbol{\epsilon}_j e^{i\mathbf{k}_j \cdot \mathbf{r}} \right), \quad (5.37)$$

to give two terms. The first term involving $a_j(0)e^{-i\omega_j t}$ is the free evolution of the field, and the second term called \mathbf{E}_s^+ is the “source” term which arises from the interaction terms in the Hamiltonian,

$$\mathbf{E}_s^+(\mathbf{r}, t) = \sum_j \sqrt{\frac{\hbar\omega_j}{2\epsilon_0 V}} \left(\boldsymbol{\epsilon}_j e^{i\mathbf{k}_j \cdot \mathbf{r}} g_j^\dagger \int_0^t \sigma_-(t')e^{-i\omega_j(t-t')} dt' \right), \quad (5.38)$$

where we have taken the atom (QD) to be at the origin. So we now are able to write the source-field in terms of an integral over the atomic lowering operator. In order to simplify the problem, we move to a continuum description of the field modes, replacing the sum, \sum_j , with $\left(\frac{V}{(2\pi)^3}\right) \int_{-\infty}^{\infty} d^3k$ and ω_j with $\omega_k = ck$. The Weisskopf-Wigner approximation is made by evaluating the g 's at a center optical frequency ω_c , which is large compared to the other frequencies. Then by making the rotating wave approximation, and working out the geometry of the problem in the far field (large r), it can be shown that the source-field reduces to [68, 71],

$$\mathbf{E}_s^+(\mathbf{r}, t) = - \left(\frac{\omega_c^2 \langle 1|\mu|2\rangle \sin\theta}{4\pi\epsilon_0 c^2 r} \right) \sigma_-(t - r/c) \hat{\boldsymbol{\theta}}, \quad (5.39)$$

which shows that the source-field from the atom (QD) is proportional to the atomic lowering operator at a retarded time $t - r/c$ where r is the distance between the atom and the location at which the field is measured. For the remainder of this work, we suppress the retardation r/c to simplify the notation.

Using this result, we return to calculating $g^{(2)}(\tau)$ for resonance fluorescence. We can now rewrite,

$$g^{(2)}(\tau) = \frac{\langle E^-(t)E^-(t+\tau)E^+(t+\tau)E^+(t) \rangle}{\langle E^-(t)E^+(t) \rangle \langle E^-(t+\tau)E^+(t+\tau) \rangle}, \quad (5.40)$$

as

$$g^{(2)}(\tau) = \frac{\langle \sigma^+(t)\sigma^+(t+\tau)\sigma^-(t+\tau)\sigma^-(t) \rangle}{\langle \sigma^+(t)\sigma^-(t) \rangle \langle \sigma^+(t+\tau)\sigma^-(t+\tau) \rangle}. \quad (5.41)$$

and for zero time delay, $\tau = 0$,

$$\langle \sigma^+(t)\sigma^+(t)\sigma^-(t)\sigma^-(t) \rangle = 0. \quad (5.42)$$

We see that the numerator is zero, since $\sigma^+(t)\sigma^+(t) \propto |2\rangle\langle 1||2\rangle\langle 1| = 0$, indicated the antibunching at time zero [68].

So we have formally shown that resonance fluorescence exhibits antibunching for zero time delay. In order to get the full time dependence of $g^{(2)}(\tau)$, the quantum regression theorem is typically used [64, 71]. By making the Markovian approximation, the quantum regression theorem lets one write the two-time correlation functions

needed to calculate $g^{(2)}(\tau)$ in terms of single time expectation values. The result is that [64, 71],

$$\begin{aligned} & \langle \sigma^+(t)\sigma^+(t+\tau)\sigma^-(t+\tau)\sigma^-(t) \rangle \\ &= \frac{\Omega_0^2/2}{\Omega_0^2 + \gamma\gamma_2} \left(1 - [\cos(\lambda|\tau|) + \frac{\gamma + \gamma_2}{2\lambda} \sin(\lambda|\tau|)] e^{-\frac{1}{2}(\gamma+\gamma_2)|\tau|} \right), \end{aligned} \quad (5.43)$$

where

$$\lambda = \sqrt{\Omega_0^2 - \frac{(\gamma - \gamma_2)^2}{4}}, \quad (5.44)$$

which for $\tau > 0$ is exactly the same expression that we found in Section 5.14 for $\rho_{22}(t)$ by solving the semiclassical density matrix equations for the initial condition $\rho_{11}(0) = 1$. The normalized $g^{(2)}(\tau)$ in steady state is therefore,

$$g^{(2)}(\tau) = \left(1 - [\cos(\lambda|\tau|) + \frac{\gamma + \gamma_2}{2\lambda} \sin(\lambda|\tau|)] e^{-\frac{1}{2}(\gamma+\gamma_2)|\tau|} \right) \quad (5.45)$$

which we again see is zero for $\tau = 0$ [64, 71].

It is interesting to consider the interpretation of this result, since we have found that the steady state second order intensity correlation function of the resonance fluorescence under cw excitation has the same form as the transient excited state population $\rho_{22}(t)$ under step-wise excitation. This similarity was noted by Kimble and Mandel in their 1976 work on resonance fluorescence, as an example of what a small role the quantized nature of the field has to do with the results of quantum optics measurements [64]. As can be seen with the source-field approach (Equation 5.39), the quantum optical properties of the field can be related back to the quantum mechanical properties of the source atom. In the case of $g^{(2)}(\tau)$, we can consider the measurement of the first photon as initializing the atom to the ground state, setting the same initial condition used in calculating Equation 5.14. The initialized two-level system is driven by a cw field which leads to Rabi oscillations in time, so that the conditional probability of detecting a second photon after the first is given by Equation 5.14 [64, 66].

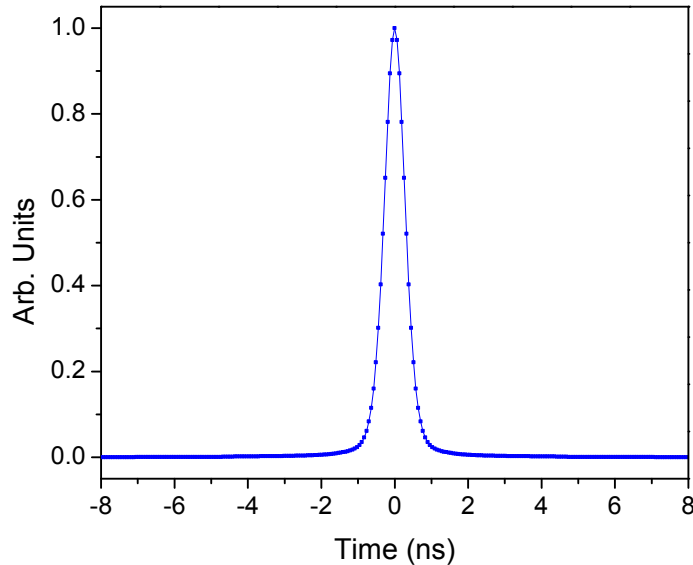


Figure 5.11: A two-sided IRF shows the temporal response in a second order intensity correlation measurement. It is constructed by convolving a time reversed IRF from one detector with a forward time IRF from the other and symmetrizing the result. The resulting IRF width 630 ps FWHM.

5.3.1 Experimental results

The experiments are performed on the same QD trion state studied throughout this chapter. A Coherent 899-21 laser generates the resonant cw field which drives the QD at 10538.85 cm^{-1} with approximately 920 nW of incident power (10 mV transmission, $\Omega_0/2\pi \approx 360 \text{ MHz}$) The resonance fluorescence is collected in the transmission geometry, and the excitation laser is rejected using the same cross-polarization fiber setup used in previous sections. The fluorescence is split with a 50-50 fiber beam splitter and sent to two nearly identical SPADS. Here, we use the higher detection τ -SPAD model detectors since the success rate of a second order intensity correlation measurement is proportional to the detection efficiency (η) squared (see below), where $\eta \approx 10^{-5}$. Recall that these detectors have a timing resolution (IRF FWHM) of about 450 ps, but since the $g^{(2)}(\tau)$ measurement is dependent on the IRFs of both detectors, a composite coincidence IRF is constructed by convolving a time reversed IRF with the forward time IRF shown in Figure 5.11.

Detection events are time-tagged using two independent channels of the HH400 in “T2” mode. The detection events are post processed to calculate the temporal correlation function between detection events. Since we split the first photon at time t_1 between two detectors, it can go to either SPAD 1 (D_1) or SPAD 2 (D_2). Similarly the second photon at time t_2 can also go to either detector, so the probability of getting two clicks is,

$$P_{success} = \frac{1}{2}\eta(D_1(t_1) + D_2(t_1)) \times \frac{1}{2}\eta(D_1(t_2) + D_2(t_2)), \quad (5.46)$$

which equals

$$P_{success} = \frac{1}{4}\eta^2(D_1(t_1)D_1(t_2) + D_1(t_1)D_2(t_2) + D_2(t_1)D_1(t_2) + D_2(t_1)D_2(t_2)). \quad (5.47)$$

Due to the dead time of the detectors and electronics, only the two terms with a click in each detector can contribute,

$$P_{success} = \frac{1}{4}\eta^2(D_1(t_1)D_2(t_2) + D_2(t_1)D_1(t_2)), \quad (5.48)$$

and since we are time-tagging each channel separately and analyzing the data in post-processing, we are able to collect both of these contributions. In a traditional TCSPC experiment using a single TAC with one detector as the “start” and the other as the “stop,” only one of these terms is recorded. So we have found that the success probability scales like $\frac{1}{2}\eta^2$. In the post-processing, we choose a time bin size of 64 ps, which following an analysis similar to Equation 5.13 requires 2-3 hours of integration to obtain a SNR of approximately 10:1.

The raw data are shown in Figure 5.12 along with the theoretical prediction expected from Equation 5.45 and the convolved theory. The data is accumulated over approximately 3 hours, which corresponds to a $g^{(2)}(\infty)$ level of about 70 counts per time bin. In Figure 5.12 we have plotted Equation 5.45 (green) using the parameters obtained from the short pulse and Rabi data with no free parameters. The theory is then convolved with a two-sided IRF (Figure 5.11) to show the expected signal. Here, we do not attempt to deconvolve the raw data due to the relatively low signal to noise, however, the convolved theory shows good qualitative agreement with the

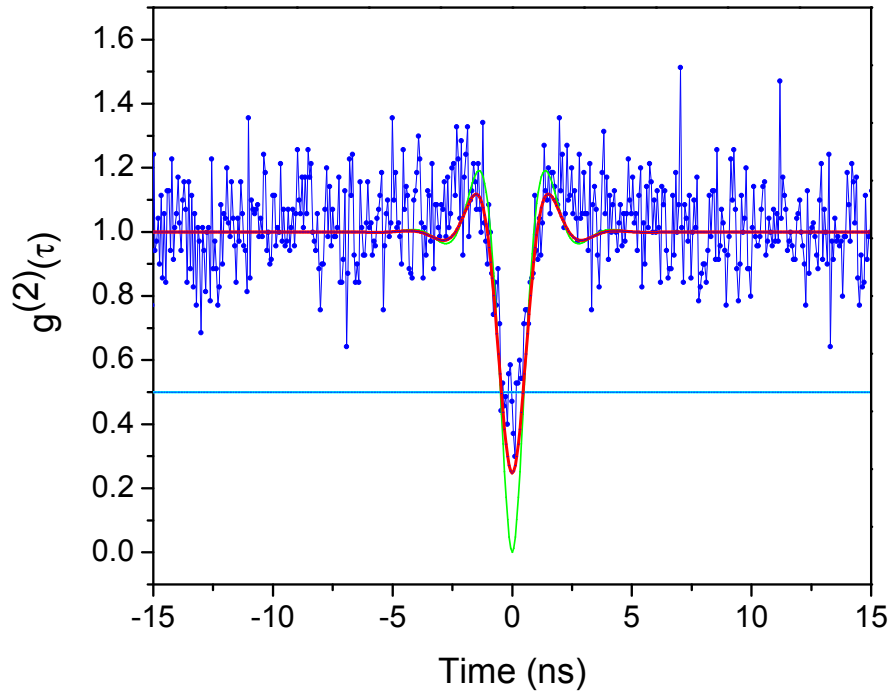


Figure 5.12: Blue: Second order intensity correlation function for QD resonance fluorescence under cw excitation showing a clear antibunching dip at zero time delay. Green: Theoretical prediction from Equation 5.45 using the QD parameters measured in pulsed measurement. Red: The theoretical prediction (green curve) is convolved with the two-sided IRF (Figure 5.11) to show the expected signal. The blue line at 0.5 shows the single photon limit, and since the $g^{(2)}$ signal is below 0.5 at time zero, the QD is a single photon source.

measured $g^{(2)}$ signal. Since the antibunching dip falls below 0.5 at zero time, we can conclusively say that the QD is a single photon source.

5.4 Chapter Summary

In this chapter, we have developed a theoretical background for quantum optics measurements, and performed transient measurements on the spontaneous emission and resonance fluorescence from a single charged QD. Using TCSPC techniques and EOM generated optical pulses, we have measured the lifetime of the QD trion state, and observed both power dependent and time dependent Rabi oscillations, verifying the coherent optical response of the QD. Under cw excitation, the second order intensity correlation function of QD resonance fluorescence exhibits photon antibunching which shows that it is a source of single photons.

CHAPTER 6

An Optically Driven QD Spin

In this work, we are ultimately pursuing a quantum information architecture based on optically driven QD spins. Recall from Chapter 3, that the QD is charged with a single electron which will serve as a spin qubit, but due to the optical selection rules, the spin can not be manipulated optically. In this Chapter, we apply an external magnetic field which breaks the symmetry and leads to new eigenstates, which allow for the realization of an optically driven QD spin qubit. This chapter is intended as a review of charged InAs QDs in the presence of an external magnetic field. The physics of this system and the experimental achievements presented in this Chapter are now well-established [2, 59, 73, 104, 105].

6.1 Selection Rules with Magnetic Field in the Voigt Geometry

In the absence of an external magnetic field, the charged QD is composed of two degenerate two-level systems which we call the z -basis states (Chapter 2). The transition between $|z+\rangle$ to $|T_z+\rangle$ is excited with $\sigma+$ polarized light and the transition from $|z-\rangle$ to $|T_z-\rangle$ is excited with $\sigma-$ polarized light, and the cross transitions (e.g. $|z+\rangle$ to $|T_z-\rangle$) are not allowed. We now consider the effect of an external magnetic field applied perpendicular to the growth direction (called the Voigt geometry). Recall that the ground state spin is determined by the single electron in the conduction band energy level, and the trion state spin is determined by the heavy hole since the electron spins form a singlet (Chapter 2). The Zeeman interaction between the spins and the externally applied magnetic field mixes the z -basis to form new eigenstates.

In particular, the magnetic field is applied along the x direction so that $\mathbf{B}_{ext} = B\hat{x}$, so that the interaction Hamiltonian is,

$$H_{Zeeman} = g_{e,i}\mu_B B \hat{S}_{e,x} - g_{h,i}\mu_B B \hat{S}_{h,x} \quad (6.1)$$

where, B is the magnitude of the applied field, μ_B is the Bohr magneton, $g_{e,i}$ and $g_{h,i}$ are the electron and heavy hole in-plane g-factors, and $\hat{S}_{e,x}$ ($\hat{S}_{h,x}$) and are the spin operators for the electron (hole). Writing this Hamilton in the z -basis, we find

$$H_{Zeeman} = \begin{matrix} & |z+\rangle & |z-\rangle & |T_z+\rangle & |T_z-\rangle \\ \langle z+| & \left(\begin{array}{cccc} 0 & \frac{\hbar g_{e,i}\mu_B B}{2} & 0 & 0 \\ \frac{\hbar g_{e,i}\mu_B B}{2} & 0 & 0 & 0 \\ 0 & 0 & 0 & -\frac{\hbar g_{h,i}\mu_B B}{2} \\ 0 & 0 & -\frac{\hbar g_{h,i}\mu_B B}{2} & 0 \end{array} \right) & & & \\ \langle z-| & & & & \\ \langle T_z+| & & & & \\ \langle T_z-| & & & & \end{matrix} \quad (6.2)$$

which can be broken into two independent 2×2 Hamiltonians for the electron and hole. The new eigenstates of the system, called the x -basis states, are

$$|x+\rangle = \frac{|z-\rangle + |z+\rangle}{\sqrt{2}} \quad (6.3)$$

$$|x-\rangle = \frac{|z-\rangle - |z+\rangle}{\sqrt{2}} \quad (6.4)$$

$$|T_x+\rangle = \frac{|T_z-\rangle + |T_z+\rangle}{\sqrt{2}} \quad (6.5)$$

$$|T_x-\rangle = \frac{|T_z-\rangle - |T_z+\rangle}{\sqrt{2}}, \quad (6.6)$$

with the energy level structure of this four-level system is shown in Figure 6.1. The x -basis ground states are split by the Zeeman frequency $\Delta_e = g_{e,i}\mu_B B$, and the trion states are now split by $\Delta_h = g_{h,i}\mu_B B$.

The optical selection rules in the x -basis can be calculated from the z -basis selection rules. Recall that the electric dipole interaction is $H_{dip} = -\boldsymbol{\mu} \cdot \mathbf{E}$, so if we consider a transition between $|x+\rangle$ and $|T_x+\rangle$, we find

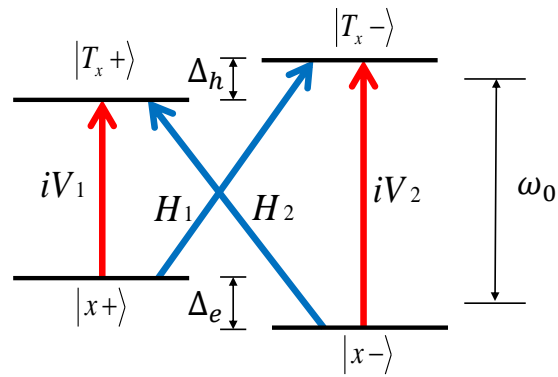


Figure 6.1: Energy level diagram for the charged QD with an external magnetic field applied perpendicular to the growth geometry (Voigt direction), forming a four-level system. The ground states form the spin qubit and are split by the Zeeman frequency (Δ_e). The optically excited trion states are at a frequency, ω_0 , above the ground states which corresponds to a wavelength of approximately 950 nm for the QDs studied in this work. The trion states are split by the hole Zeeman frequency (Δ_h). The transitions are coupling with horizontally (H) and vertically (V) polarized light, where the i is a reminder of the relative phase between matrix elements.

$$-\langle T_x+|\boldsymbol{\mu} \cdot \mathbf{E}|x+\rangle = -\left(\frac{\langle T_z+| + \langle T_z-|}{\sqrt{2}}\right) \boldsymbol{\mu} \cdot \mathbf{E} \left(\frac{|z+\rangle + |z-\rangle}{\sqrt{2}}\right) \quad (6.7)$$

$$= -\frac{1}{2}(\langle T_z+|\boldsymbol{\mu} \cdot \mathbf{E}|z+\rangle + \langle T_z+|\boldsymbol{\mu} \cdot \mathbf{E}|z-\rangle + \langle T_z-|\boldsymbol{\mu} \cdot \mathbf{E}|z+\rangle + \langle T_z-|\boldsymbol{\mu} \cdot \mathbf{E}|z-\rangle). \quad (6.8)$$

Looking back at Equations 2.30-2.34, we see that the only nonzero terms are

$$\begin{aligned} & -\frac{1}{2}(\langle T_z+|\boldsymbol{\mu} \cdot \mathbf{E}|z+\rangle + \langle T_z-|\boldsymbol{\mu} \cdot \mathbf{E}|z-\rangle) = \\ & -\frac{1}{2}(\langle T_z+|rC_{+1}^{(1)}|z+\rangle E_{-1} + \langle T_z-|rC_{-1}^{(1)}|z-\rangle E_{+1}) \end{aligned} \quad (6.9)$$

where E_{-1} and E_{+1} are the coefficients of the polarization vectors in the spherical tensor basis,

$$\mathbf{E} = -\frac{1}{2}(E_{-1} \hat{\mathbf{e}}_{+1} + E_{+1} \hat{\mathbf{e}}_{-1}). \quad (6.10)$$

Taking the coefficients to be equal, and recalling that $\hat{\mathbf{e}}_{\pm 1} = \mp \frac{\hat{\mathbf{x}} \pm i\hat{\mathbf{y}}}{\sqrt{2}}$, we find,

$$\mathbf{E} = -\frac{E}{2}(\hat{\mathbf{e}}_{+1} + \hat{\mathbf{e}}_{-1}) = -\frac{E}{2\sqrt{2}}[-(\hat{\mathbf{x}} + i\hat{\mathbf{y}}) + (\hat{\mathbf{x}} - i\hat{\mathbf{y}})] = \frac{E}{\sqrt{2}} i\hat{\mathbf{y}}, \quad (6.11)$$

so we see that the $|x+\rangle$ to $|T_x+\rangle$ transition is driven by a $\hat{\mathbf{y}}$ polarized field which corresponds to vertical polarization in the laboratory. Performing similar calculations on the the other three transitions, one finds that the $|x-\rangle$ to $|T_x-\rangle$ is also driven by vertically polarized field, and the two cross transitions are driven by $(\hat{\mathbf{x}})$, a horizontally polarized field. Because of these selection rules, we refer to the outer two transitions as “vertically or V polarized” and the inner two as “horizontally or H polarized.” There is a relative phase of i between the transition matrix elements of the H and V transitions. These selection rules are shown in Figure 6.2. Even though we call the transitions H and V , the actual orientation of these transitions in the laboratory frame can vary due to the heavy-light hole mixing effect [59, 106]. The transitions are still excited by linearly polarized light, and the V transitions remain orthogonal to the H transitions, however, the absolute orientation of the transitions is rotated

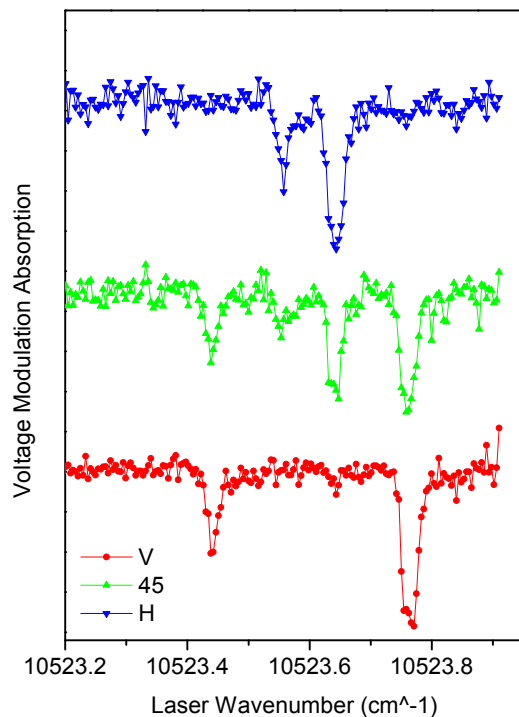


Figure 6.2: Selection rules of a charged QD with a magnetic field applied in the Voigt geometry. The inner (outer) transitions are driven by horizontally- H (vertically- V) polarized light which are orthogonal, although the absolute orientation of these transitions can vary due to heavy-light hole mixing. When the laser is polarized at 45 degrees, all transitions can be excited.

relative to the laboratory frame. Since the relative polarizations are not affected, once the rotation angle for a specific QD is found, studies can be performed in this rotated frame as usual [59].

The external magnetic field, “turns on” the cross transitions, which allows for optical manipulation of the electron spin. Since the magnetic field determines the Zeeman splittings, it can be used to tune the four-level system for particular quantum information applications. In order to frequency resolve the four levels, the magnitude of the magnetic field applied is on the order of 0.5 – 3 T, since the trion linewidth is approximately 600 MHz and the electron (hole) splitting frequencies are typically

7 GHz/T and 4 GHz/T respectively ($g_{e,i} \approx 0.5$ and $g_{h,i} \approx 0.3$). In the analogy with QDs as artificial atoms, this system is in some sense a realization of an artificial trapped ion, where the long lived spin state, which exhibits slow decoherence, can be used to encode quantum information, while the optically excited states can be used to rotate the spin with fast optical pulses.

6.2 Spectroscopy on the Four-Level QD System

The four-level QD system is characterized using the cw spectroscopy techniques described in Chapter 3. We continue using a semi-classical description of the QD-laser field interaction, taking the incident laser fields to be classical, of the form $\mathbf{E}(t) = \mathbf{E}_0(t) \cos(\omega t)$, where $E_0(t)$ is the envelope and ω is the laser frequency. The Hamiltonian for the four-level system in the presence of an external driving field is,

$$\hat{H} = \begin{array}{c} \langle x- | \\ \langle x+ | \\ \langle T_x+ | \\ \langle T_x- | \end{array} \begin{array}{c} |x-\rangle \quad |x+\rangle \quad |T_x+\rangle \quad |T_x-\rangle \\ \left(\begin{array}{cccc} -\frac{\hbar\Delta_e}{2} & 0 & V_{13} & V_{14} \\ 0 & \frac{\hbar\Delta_e}{2} & V_{23} & V_{24} \\ V_{31} & V_{32} & -\frac{\hbar\Delta_h}{2} + \hbar\omega_0 & 0 \\ V_{41} & V_{42} & 0 & \frac{\hbar\Delta_h}{2} + \hbar\omega_0 \end{array} \right) \end{array}$$

where we index the states in order of increasing energy: $|x-\rangle = |1\rangle$, $|x+\rangle = |2\rangle$, $|T_x+\rangle = |3\rangle$, $|T_x-\rangle = |4\rangle$, and $V_{ij} = -\langle i | \boldsymbol{\mu} \cdot \mathbf{E}(t) | j \rangle$ such that,

$$\begin{aligned} V_{13} &= \hbar\Omega_{13}(t) \cos(\omega t - \phi(t)) \\ V_{24} &= \hbar\Omega_{24}(t) \cos(\omega t - \phi(t)) \\ V_{14} &= -i\hbar\Omega_{14}(t) \cos(\omega t - \phi(t)) \\ V_{23} &= -i\hbar\Omega_{23}(t) \cos(\omega t - \phi(t)) \\ V_{ji} &= V_{ij}^* \end{aligned} \tag{6.12}$$

where the time-dependent Rabi frequency is related to the field envelope ($E_{ij,0}(t)$) by $\Omega_{ij}(t) = \mu E_{ij,0}(t)/\hbar$ and we take the magnitude of the dipole moment to be equal for the four transitions.

To calculate the optical response and time evolution of the driven four-level system, we use the density matrix formalism discussed in Chapter 2. The equations of motion for the density matrix elements are obtained by using the master equation,

$$i\hbar\hat{\rho}/dt = [\hat{H}, \hat{\rho}] + \text{relaxation terms}, \quad (6.13)$$

which gives 16 equations of motion which are presented in several of my colleague's theses [73,107]. Usually, the rotating wave approximation is made, and the system is transformed to an interaction picture to simplify the calculations, which is explained nicely in a recent thesis [107]. The decay terms consist of the excited state decay rates (nanosecond time scale), and their corresponding decoherence rates. In addition to these, the electron or hole (of the trion) can undergo a spin flip, but the time scale for such processes is milliseconds so it can generally be ignored. However, the electron spin ground state can decohere at a much shorter time scale (few nanoseconds), due to the hyperfine interaction with the nuclear spin bath [91,92,108].

In steady state, analytic solutions can be found to these equations, however they are too long to print here and give little insight to the physics. For cw experiments with narrow bandwidth lasers, it is usually advantageous to isolate a single three-level lambda system to simplify the problem. For the case of time-domain experiments involving short optical pulses that couple all four transitions, the time dependence of density matrix elements is generally calculated numerically, however analytic solutions for certain cases can be found (see Section 6.3).

6.2.1 Steady-State Spectroscopy and Optical Pumping

When the magnetic field is applied, the resulting four-level system can be thought of as two three-level lambda systems sharing their ground states. One might assume that since the magnetic field Zeeman splits the ground state levels, the QD electron spin would automatically be initialized to the lowest energy state. This is not the case because the thermal energy (345 μeV at 4 K) is sufficiently large to randomize the electron spin state whose Zeeman energy is typically at most 200 μeV (at 7 T). However from atomic physics, we know that a feature of a driven lambda system

is that it exhibits an effect known as optical pumping [109]. When one leg of the lambda system is resonantly driven with a cw field, the system evolves to a dark state, where the population is “pumped” to the other ground state. In quantum information science, optical pumping is a useful method for initializing the system to a pure state. In the four-level QD system, optical pumping can be used to achieve $\approx 99\%$ initialization fidelity after a few nanoseconds [104].

Narrow bandwidth lasers can be used to spectrally probe the four-level system. However, if a cw laser optically pumps the system to the other ground state, it can no longer scatter photons, and since this occurs on the time scale of nanoseconds, the time averaged absorption (or fluorescence) signal is zero. Recall from Chapters 2 and 3, that a negatively charged QD is first identified through bias-dependent photoluminescence and cw absorption spectroscopies, and that QD states have a finite voltage existence range (typically 100 – 200 mV), which is usually determined at zero magnetic field. On the edge of the existence range, the Fermi energy is at a level where the ground state charge configuration is metastable, with rapid tunneling into and out of the QD. This is called the “co-tunneling region,” and it is useful for cw spectroscopy in a magnetic field because if the tunneling rate is sufficiently fast, the system no longer optically pumps, so cw absorption or fluorescence spectroscopies can be performed [104].

Experiments are performed at approximately 5 K in a liquid helium optical cryostat with an integrated superconducting magnet capable of applying fields up to 7 T. A charged QD is identified at zero field, and its voltage existence range is determined by performing bias-dependent absorption study. The sample bias is set to the co-tunneling region edge, typically at a point where the magnitude of absorption signal is approximately half of its magnitude in the center of the existence range. When the magnetic field is applied, the single trion resonance splits to reveal the four transitions (Figure 6.3). Turning on the magnetic field does cause a slight change to the optical alignment, but the asphere-integrated sample mount (Chapter 3) is sufficiently stable so that the input laser remains sufficiently aligned with the QD to obtain an absorption signal. In some cases, the alignment needs to be re-optimized

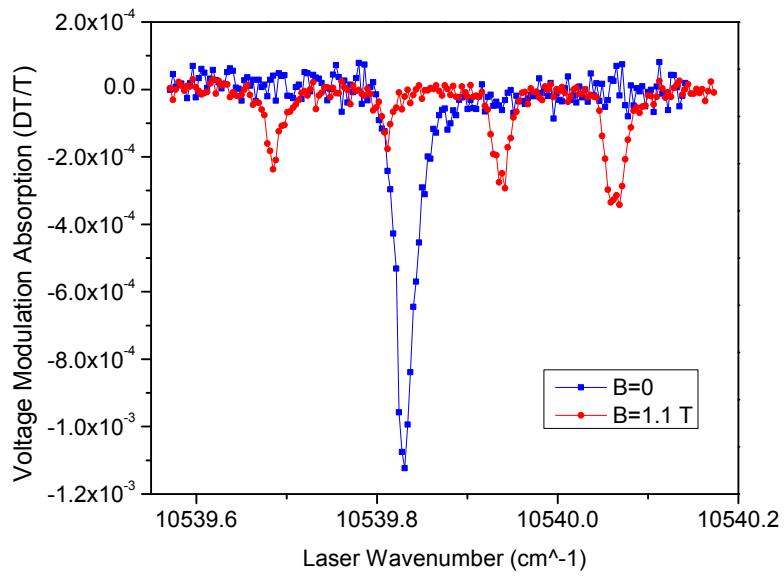


Figure 6.3: Voltage modulation absorption of a charged QD in the co-tunneling region of the voltage existence range showing the absorption signal at zero field (blue) and the signal at 1.1 T (red) where the transitions are split by the magnetic field.

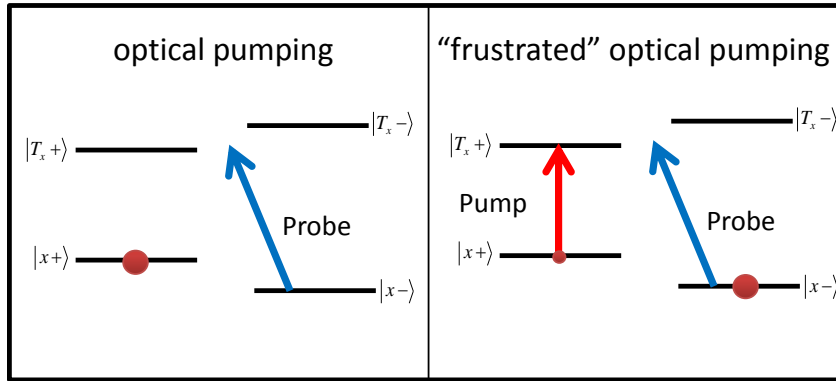


Figure 6.4: In the middle of the existence range, a single probe laser optically pumps the system so it becomes transparent (no absorption). A re-pumping laser can be added to recover the absorption by “frustrating” the optical pumping.

by peaking off the signal at field. In addition to the Zeeman splittings, there is a small diamagnetic effect which shifts all four transitions to higher energy as seen in Figure 6.3. Typically a magnetic field of 1 – 2 T is convenient for experiments, since it allows for all four peaks to be clearly separated, but still within one scan range of a tunable laser (typically 20-30 GHz). By comparing the spectral positions of the four peaks to the single zero magnetic field resonance on the edge of the existence range, one can use the trion’s Stark shift to predict the spectral positions of the resonances anywhere within the trion state’s existence range.

For quantum information applications, the ground state has to be stable to serve as a qubit, so we must work in the middle of the existence range, where the system goes transparent to absorption due to optical pumping. The absence of absorption in the middle of the existence range is evidence of optical pumping, but we would like to optically probe and manipulate the four-level system in this stable regime. The solution is to add an additional laser. This laser serves as a re-pumping beam that frustrates the optical pumping by driving another transition which repopulates the depleted ground state (Figure 6.4).

In two laser experiments, the laser being detected is called the probe, and the laser pumping the system is called the pump. The pump and probe are usually cross-polarized at either $+45^\circ / -45^\circ$ or σ^+ / σ^- so that both lasers can couple to all four transitions, but polarization can be used to isolate the probe from the pump before the detector. Typically, large voltage modulation is used so that the lock-in signal directly reflects the absorption signal (c.f. Chapter 3) [59]. In Figure 6.5, we are able to clearly observe optical pumping behavior. When the pump is off, there is no absorption since the probe optically pumps the population over to the other ground state. Then, when a pump is tuned to one of the low (high) energy transitions, absorption is recovered on the two high (low) energy transitions, demonstrating the re-pumping behavior [104, 110]. Similar two-laser fluorescence measurements can be performed by directly detecting fluorescence as described in Chapter 3. However, since polarization is used to reject the excitation lasers, the pump and probe must be copolarized, and the signal is now proportional to the sum of two excited state populations.

We have reviewed the fundamentals of cw spectroscopy and optical pumping of a negatively charged QD in the presence of a magnetic field in the Voigt geometry. Using cw absorption spectroscopy, the four-level system and its optical selection rules are verified. We are able to observe two distinct regimes in the QD's voltage existence range: the co-tunneling regime where the unstable ground state allows for identification of the transitions and selection rules, and the stable optical pumping regime where the system optically pumps with a single probe laser. In the optical pumping regime, the steady state probe absorption can be recovered by using an additional (re-pumping) laser as described here, or by using a pulsed laser to rotate the ground state as described in the next section [105]. Optical pumping will be used for the remainder of this work to initialize the electron spin to a pure state. Further details on these methods can be found in the theses which first developed these techniques [59, 73].

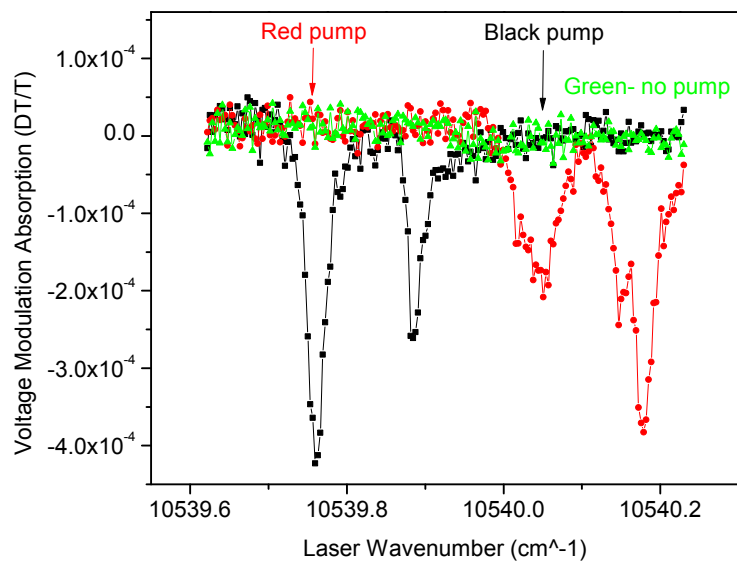


Figure 6.5: In the middle of the voltage existence range, the ground state is stable, and the four-level system undergoes optical pumping so it is transparent to a single probe laser beam (green). If the re-pumping beam is pumps one of the right transitions absorption

6.3 Picosecond Qubit Rotations- Spin Rabi

Quantum information applications of QD spins require the ability to manipulate the spin qubit rapidly relative to the coherence time [24]. For InAs QDs, the electron spin coherence time (T_2^*) is typically a few nanoseconds, although the intrinsic time (T_2) can be extended to the microsecond time scale using cw locking and echo techniques [91, 108]. In this work, short (2-3 ps) pulses from a mode-locked Ti:sapphire laser are used to perform coherent spin rotations, by driving the two-photon (Raman) transitions of the four-level system.

In Chapter 5, the basic theory of Rabi oscillations is presented for a resonantly driven two-level system. Using the charged dot in the absence of a magnetic field, we are able to observe both time-dependent Rabi oscillations by time resolving the fluorescence under square-pulse excitation, and field-dependent Rabi oscillations by varying the power of short pulses. In quantum information science, field-dependent Rabi oscillations using short pulses are especially useful because they can serve to rotate the state of a qubit rapidly. Now that the QD spin can be initialized to a pure state via optical pumping, we would like to use Rabi oscillations to coherently manipulate the spin qubit. However, unlike the two-level system of Chapter 5, the QD spin states of the four-level system are optically coupled through the excited trion states. Recall that the Zeeman frequency, Δ_e , is typically chosen to be 5–10 GHz, so the spin could be directly manipulated by applying a resonant microwave field at Δ_e that drives the magnetic dipole transition [111], however, it is often more practical to use short optical pulses driving the electric dipole transitions because of the short pulse widths and ability to focuss the light onto a single dot using far field optics.

Consider the case of a QD initialized to the $|x-\rangle$ state by optical pumping. Using the optical Rabi oscillations described in Chapter 5, one could perform optical manipulations of the QD spin by applying two separate optical pulses. For example, the spin could be flipped with a π pulse on V_2 that drives the population up to $|T_x-\rangle$, and then a π pulse on H_1 that drives the population down to $|x+\rangle$ (Figure 6.6). This technique is not ideal because it relies on creating significant trion population, and due to relatively short trion lifetime (≈ 1 ns), decay while the trion is populated limits

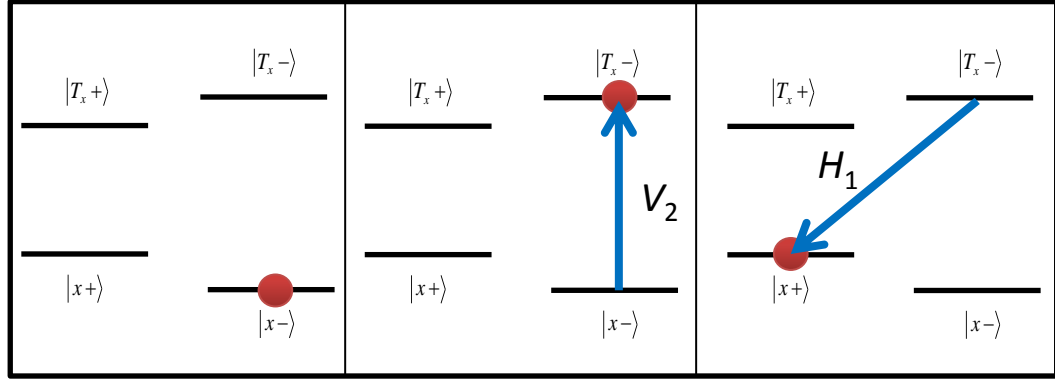


Figure 6.6: The electron spin can be optically manipulated by a step-wise two pulse sequence relying on intermediate trion population. Step-wise approaches generally exhibit lower fidelities due to fast decay in the excited state.

the operation’s fidelity. The solution is to temporally overlap the pulses so that they can drive a two-photon transition (stimulated Raman transition). If the excitation pulses are sufficiently detuned from the trion resonance, they can still be resonant on the two-photon transition, but they excite trion population only virtually [112, 113] (Figure 6.7). For sufficiently detuned pulses, the system can be modeled as an effective two-level system composed of the two ground states $|x+\rangle$ and $|x-\rangle$, where the optical pulses are used to drive “spin Rabi” oscillations between the spin states.

So we are left considering the interaction of a QD spin with a detuned optical pulse. A complete derivation of this interaction can be found in the literature [112, 113] and in previous students theses [73, 107], but we review a few important results for completeness. In practice, a single 2-3 ps pulse can replace the two pulses described above given that the pulse bandwidth (≈ 200 GHz) is larger than the electron Zeeman frequency (≈ 7 GHz). One begins with the complete Hamiltonian (Equation 6.1), and since the pulse width is much shorter than the trion lifetime (≈ 1 ns), decay during the pulse can be neglected. Therefore, it is sufficient to work with state amplitudes, where the state vector can be written,

$$|\psi(t)\rangle = a_1(t)|1\rangle + a_2(t)|2\rangle + a_3(t)|3\rangle + a_4(t)|4\rangle \quad (6.14)$$

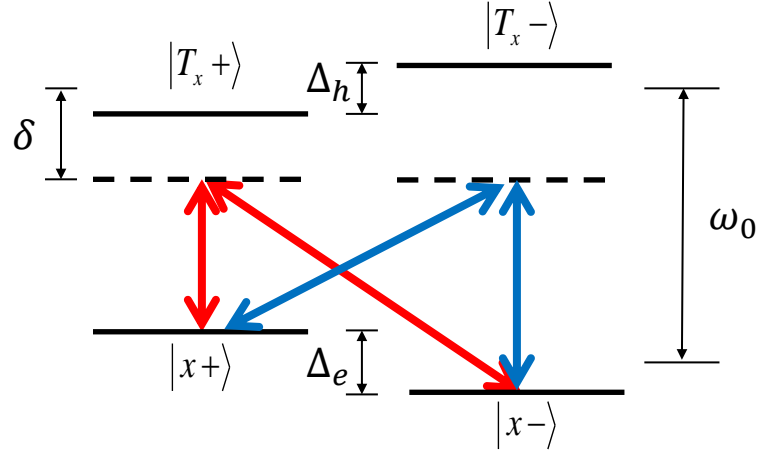


Figure 6.7: Energy level diagram depicting the two-photon resonance for a detuned stimulated Raman transition. The relevant frequencies are shown labeling the trion resonance (ω_0), the electron Zeeman frequency (Δ_e), the hole Zeeman frequency (Δ_h), and the laser detuning (δ).

The driving field is taken to be of the form,

$$\mathbf{E} = \frac{1}{2}[(E_x(t)\hat{\mathbf{x}} + E_y(t)\hat{\mathbf{y}})e^{-i\omega t} + c.c.], \quad (6.15)$$

The problem is most easily solved in the field interaction picture,

$$a_1(t) = c_1(t) \quad (6.16)$$

$$a_2(t) = c_2(t) \quad (6.17)$$

$$a_3(t) = c_3(t)e^{-i\omega t} \quad (6.18)$$

$$a_4(t) = c_4(t)e^{-i\omega t} \quad (6.19)$$

where ω is the center frequency of the driving field so that,

$$|\psi(t)\rangle = c_1(t)|1\rangle + c_2(t)|2\rangle + c_3(t)e^{-i\omega t}|3\rangle + c_4(t)e^{-i\omega t}|4\rangle. \quad (6.20)$$

The Hamiltonian in this field interaction picture is,

$$H_{FIP} = \hbar \begin{pmatrix} -\frac{\Delta_e}{2} & 0 & \chi_H^*(t) & \chi_V^*(t) \\ 0 & \frac{\Delta_e}{2} & \chi_V^*(t) & \chi_H^*(t) \\ \chi_H(t) & \chi_V(t) & -\frac{\Delta_h}{2} + \delta & 0 \\ \chi_V(t) & \chi_H(t) & 0 & \frac{\Delta_h}{2} + \delta \end{pmatrix} \quad (6.21)$$

where we have made the rotating wave approximation, and $\chi_H(t) = \frac{\mu E_x(t)}{\sqrt{2}\hbar}$, $\chi_V(t) = \frac{i\mu E_y(t)}{\sqrt{2}\hbar}$, and $\mu = |\langle T_z + |\hat{\mu}| |z+\rangle|$, and we have taken the dipole moments of the four transitions to be equal. The resulting equations of motion are

$$\dot{c}_1(t) = i\frac{\Delta_e}{2}c_1(t) - i\chi_H^*(t)c_3(t) - i\chi_V^*(t)c_4(t) \quad (6.22)$$

$$\dot{c}_2(t) = -i\frac{\Delta_e}{2}c_2(t) - i\chi_V^*(t)c_3(t) - i\chi_H^*(t)c_4(t) \quad (6.23)$$

$$\dot{c}_3(t) = -i\chi_H(t)c_1(t) - i\chi_V(t)c_2(t) + i\left(\frac{\Delta_h}{2} - \delta\right)c_3(t) \quad (6.24)$$

$$\dot{c}_4(t) = -i\chi_V(t)c_1(t) - i\chi_H(t)c_2(t) - i\left(\frac{\Delta_h}{2} + \delta\right)c_3(t). \quad (6.25)$$

For a sufficiently large detuning, δ , one can adiabatically eliminate the excited states (c_3, c_4), resulting in an effective two-level system. One can simplify the effective two-level spin Hamiltonian to the form [73, 107],

$$H_{spin} = \hbar \begin{pmatrix} -\frac{\Delta_e}{2} & -\frac{\chi_H^*(t)\chi_V(t) + \chi_V^*(t)\chi_H(t)}{\delta} \\ -\frac{\chi_H^*(t)\chi_V(t) + \chi_V^*(t)\chi_H(t)}{\delta} & +\frac{\Delta_e}{2} \end{pmatrix} \quad (6.26)$$

Where we see that the coupling between the spin states is from a two-photon process. For the case of arbitrary polarization $E_x(t) = \cos(\theta)E(t)$ and $E_y(t) = \sin(\theta)E(t)e^{i\phi}$. The magnitude of the off diagonal terms are maximum for circular polarizations, $\theta = \pi/4$ and $\phi = (n + 1/2)\pi$, where n is an integer. So that we can write,

$$\frac{\chi_H^*(t)\chi_V(t) + \chi_V^*(t)\chi_H(t)}{\delta} = -\frac{\mu E^2(t) \sin(\phi)}{\hbar\delta}. \quad (6.27)$$

so $\phi = \pm\frac{\pi}{2}$ corresponds to $\sigma\pm$ polarization. We are interested in using a short pulse to drive a spin rotation, of the form,

$$E(t) = E_0 \operatorname{sech}\left(\frac{t}{\tau}\right), \quad (6.28)$$

where τ is the pulse width, and E_0 is the amplitude of the pulse. Assuming that τ is much shorter than the precession period, one can write an effective rotation operator for the interaction by neglecting precession during the pulse, such that [73, 107],

$$\hat{R}_\alpha = \hbar \begin{pmatrix} \cos(\alpha/2) & i \sin(\alpha/2) \\ i \sin(\alpha/2) & \cos(\alpha/2) \end{pmatrix}$$

where the rotation angle is given by $\alpha = \int [-\frac{\mu E^2(t) \sin(\phi)}{\delta}] dt$. So, we see that we can control the rotation angle by the the applied field amplitude, detuning, and polarization. We see that for circularly polarized pulses, $\sin(\pm\pi/2) = \pm 1$, which maximizes the rotation angle. We can observe “spin-Rabi” oscillations of the effective two-level system by varying the field amplitude with the other parameters fixed [2, 30, 105]. In this work, the pulses are red detuned, so that $\delta > 0$. The polarization ($\sigma\pm$) can be used to flip the sign of the off diagonal terms.

6.3.1 Spin Rotation Experiments

Spin rotation experiments are performed in the magnetic optical cryostat with an applied magnetic field of 1.1 T. The spin state is initialized to $|x-\rangle$ with a 4 ns optical pumping pulse resonant with the V_1 transition. A Coherent MIRA 900 mode-locked Ti:sapphire laser generates 2 ps laser pulses which serve to rotate the spin state, by driving the stimulated Raman transition (Section 6.3). The spin rotation pulses are red detuned from the trion resonances by approximately 1 meV (240 GHz). The 4 ns pulse is generated by gating a cw laser with an EOM synchronized with the MIRA pulses which sets the experimental repetition rate of approximately 76 MHz. The 4 ns optical pumping pulse for the next experimental run also serves as a spin read out by scattering a single photon if the spin is in the $|x+\rangle$ state (Figure 6.8).

The optical pumping and rotation pulses are circularly polarized ($\sigma-$). The $\sigma+$ polarized light from the QD is collected using the cross polarization fiber setup described in Chapter 3. In order to further suppress the rotation laser pulses, the collected light is passed through an air spaced etalon to spectrally reject the detuned rotation laser by an additional factor of ≈ 35 dB. The etalon has a ≈ 37 GHz FWHM transmission width and a free spectral range of ≈ 3.6 THz (10 nm) with an insertion loss of ≈ -0.6 dB. The QD photons are directly detected using a single photon detector and the HH400 in integration mode as described in Chapters 4, 5. This provides a measure of the fluorescence counts as a function of time relative to the experimental clock.

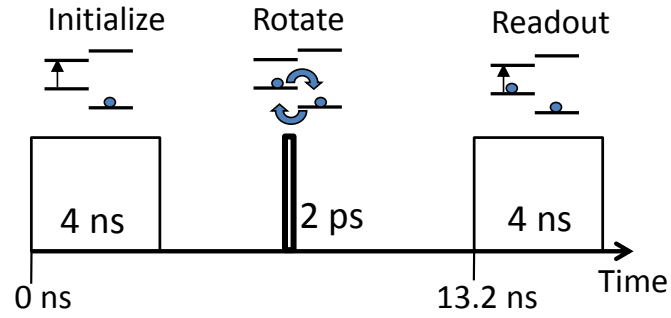


Figure 6.8: Timing diagram for the spin-Rabi experiments. A 4 ns optical pumping pulse initializes the system to a pure state. A detuned 2 ps pulse driving the two-photon resonance rotates the spin state. The resulting spin population is read out by detecting a single scattered photon during the next 4 ns pulse.

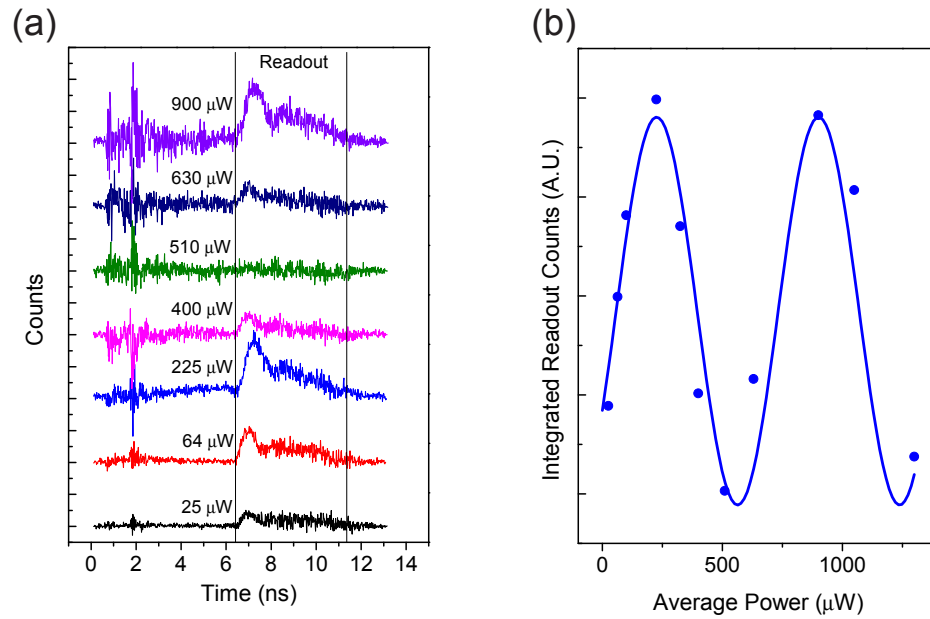


Figure 6.9: (a) fluorescence histograms showing readout signal from the 4 ns pulse as a function of the applied rotation pulse power. The area under the curves in the “Readout” time region serves as a measure of the $|x+\rangle$ population. The noise around 2 ns comes primarily from imperfect background subtraction. (b) The integrated readout signals from data sets as shown in (a) are plotted versus the applied pulse power to observe power dependent spin-Rabi oscillations.

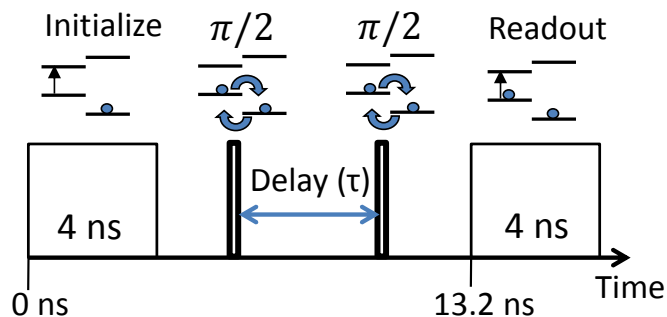


Figure 6.10: Timing diagram for a spin coherence measurement. The first $\pi/2$ pulse creates a superposition of x -basis states which undergoes unitary evolution in time until the second pulse rotates the coherence into a x basis population that is read out by the 4 ns pulse. The time delay between the two $\pi/2$ -area pulses is varied to observe oscillations at the electron Zeeman frequency.

The counts recorded during the readout/initialization pulse serve as a measure of the $|x+\rangle$ population. The data are recorded as a function of rotation pulse power to observe “spin-Rabi” oscillations. A background measurement of the undesired laser pulse leaking onto the detector is recorded for each rotation power by Stark shifting the QD out of resonance with the 4 ns laser pulse. Using this, the on resonant signal is background subtracted, and the counts from the readout pulse are integrated to give the readout signal amplitude shown in Figure 6.9. Since this is a second order process, with an effective Rabi frequency of $\frac{|\Omega|^2}{\delta}$, the oscillation frequency is proportional to the applied average power, not the square root of the power as with trion Rabi oscillations. We observe two complete spin-Rabi cycles (up to 4π -area), however only a few points are recorded at high power since we are typically interested in $0 - \pi$ -area pulses which contribute less background to the measurement. For the remainder of this work, we use relatively low power ($\pi/2$ -area) pulses, where a fit to the low power ($< \pi$) region of the data indicate near unity rotation fidelity.

The spin rotation pulses can also be used to demonstrate the coherence of the electron spin by rotating the spin prior to measurement in the x -basis [2, 30, 105]. This is usually carried out with two temporally separated rotation pulses, and is referred to in the literature as a Ramsey experiment [114]. The QD spin is initialized and read out as in the spin-Rabi experiments, but now two rotation pulses of equal pulse area are used to manipulate the spin. The rotation pulse power is determined experimentally by performing a spin-Rabi measurement. Typically, $\alpha = \pi/2$ area pulses are used to obtain the maximum signal amplitude. The QD is initialized with a 4 ns optical pumping pulse, then the first rotation pulse generates a coherence between the electron spin states. The system undergoes unitary evolution in time until the second pulse rotates this coherence into an x -basis population which can be read out by the following 4 ns pulse. The readout signal is,

$$\text{Signal} \propto |\langle x+ | \hat{R}_{\pi/2} \hat{U}(\tau) \hat{R}_{\pi/2} | x- \rangle|^2 = \frac{1}{2} (1 + \cos(\Delta_e \tau)) \quad (6.29)$$

where

$$\hat{R}_{\pi/2} = \frac{1}{\sqrt{2}} \begin{pmatrix} 1 & i \\ i & 1 \end{pmatrix},$$

and

$$\hat{U}_\tau = \begin{pmatrix} 1 & 0 \\ 0 & e^{-i\Delta_e \tau} \end{pmatrix},$$

where τ is the time delay between the two rotation pulses. As the time delay between the two rotation pulses is varied, the readout signal oscillates at the electron Zeeman frequency, demonstrating the coherence.

The spin coherence signal is shown in Figure 6.11. The data are consistent with Zeeman frequency of 7.35 GHz obtained from cw measurements, however, the expected sinusoidal signal is distorted and resembles a saw-tooth signal. This effect is believed to arise from the hyperfine interaction with the QD's $10^4 - 10^5$ constituent nuclear spins which can become polarized giving rise to a dynamic magnetic (Overhauser) field [91, 115]. The nuclear spin fluctuations that couple to the electron spin through hyperfine interaction are the primary source of decoherence for the QD electron spin qubit, typically resulting in an electron spin coherence time (T_2^*) of a few

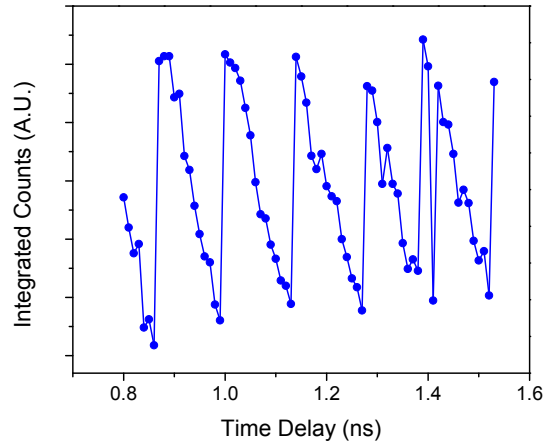


Figure 6.11: Two-pulse measurement using the pulse sequence of Figure 6.10 showing electron spin coherence. Oscillations are observed at the electron Zeeman frequency 7.35 GHz. The saw-tooth signal is believed to arise from the hyperfine interaction with the QD’s constituent nuclear ensemble. The author would like to acknowledge A. Burgers and U. Paudel for performing this measurement.

nanoseconds. Using spin echo techniques, the intrinsic decoherence time (T_2) has been measured out to microsecond time scales [108]. The nuclear spin fluctuations have also been suppressed using resonant cw techniques, showing that the nuclear field can be stabilized, extending the T_2^* decoherence time scale to microseconds [92].

6.4 Chapter Summary

In this chapter, the energy levels and optical selection rules of a charged InAs in the presence of an externally applied magnetic field have been derived. The resulting four-level system allows for a long lived electron spin qubit which can be rapidly manipulated through the QD’s optically excited trion states, realizing an optically driven spin qubit. The system is studied with a combination of cw and time domain techniques to verify the QD’s optical properties and the coherence of the electron spin state. The spin can be initialized by optical pumping, coherently manipulated with picosecond pulses driving the stimulated Raman transition, and read out by detecting a single scattered photon. In the next chapter, these techniques will be combined to

enable the experimental demonstration of spin-photon entanglement.

CHAPTER 7

Spin-Photon Entanglement

In Chapter 6, a single optically driven QD spin qubit is realized with the charged InAs QD system in the presence of an external magnetic field. The next step towards realizing a scalable quantum information architecture requires the ability to entangle spins confined to spatially distinct QDs. Spatially adjacent QD spins have been entangled by using the local tunneling interaction [35], but we pursue an approach that can mediate entanglement between distant QD spins using intermediate spin-photon entangled states. In this Chapter, we present the theory and experimental demonstration of a spin-photon entangled state.

7.1 A Quantum Dot Spin-Photon Entangled State

In this work, we consider the spin-photon entangled state generated by spontaneous decay from one of the QD's trion states [42]. Recall that the charged QD in the presence of a magnetic field forms an effective four-level system, and by using frequency selective excitation, we can isolate a three-level lambda system (Chapter 6). If the $|T_{x-}\rangle$ state is excited, it spontaneously decays with equal probability to $|x+\rangle$ or $|x-\rangle$. We can see that the decay to $|x+\rangle$ is correlated with emission of a horizontally (H) polarized photon and the decay to $|x-\rangle$ is correlated with a vertically (V) polarized photon (Figure 7.1). However, decay from $|T_{x+}\rangle$ results in the “opposite” correlation where $|x+\rangle$ ($|x-\rangle$) is correlated with V (H). Here, we study the system after it is excited to the $|T_{x-}\rangle$ state, so we are considering the “right” lambda system shown in Figure 7.1.

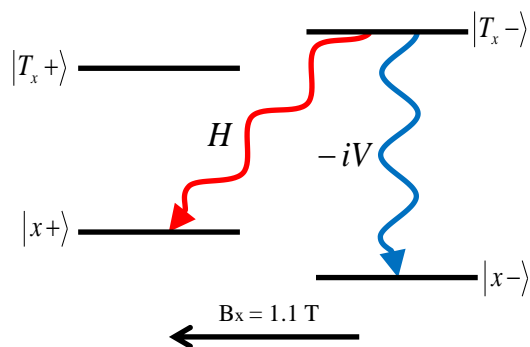


Figure 7.1: When the $|T_x -\rangle$ state decays, the spontaneously emitted photon is correlated with the resulting QD spin state.

In this Chapter, we will show that this correlated spin-photon state is actually an entangled state ($|\Psi\rangle$) of the form,

$$|\Psi\rangle = \frac{|H\rangle|x+\rangle - i|V\rangle|x-\rangle}{\sqrt{2}}. \quad (7.1)$$

Spontaneous emission occurs due to the coupling of the atomic (QD) states to the vacuum modes of the electromagnetic field which is usually treated with Weisskopf-Wigner theory [116]. Since we are often only concerned only with the state of the QD, we trace over the field, resulting in decay and decoherence rates for the the QD which we use in the density matrix formalism. Because of this, spontaneous emission is often thought of as a source of decoherence, since quantum information is “lost” to the environment.

Here, we are concerned with the spin-photon state generated after decay from the $|T_x -\rangle$ state. If we do not measure the state of the photon, and it is instead measured by the environment, the QD is equally likely to be measured in either ground state ($|x+\rangle$ or $|x-\rangle$), but there is no coherence. However, if we measure the state of the spontaneously emitted photon, and correlate this with the resulting QD state, we can observe coherent effects that arise from the entanglement between the spin and

photon. This type of entanglement was first demonstrated in 2004 by *Blinov et al.*, who showed that the polarization state of a spontaneously emitted photon from a single trapped ion is entangled with the resulting hyperfine levels of the ion [20].

To understand origin of the entangled spin-photon state, we begin with the theory of spontaneous emission in a lambda system. The Hamiltonian for the quantized three-level atom-field system is given by,

$$H = \sum_j \hbar\omega_j a_j^\dagger a_j + \hbar\omega_1 \sigma_{11} + \hbar\omega_2 \sigma_{22} + \hbar\omega_3 \sigma_{33} + \sum_j \sum_{n=1,2} \hbar g_{n,j} \left[e^{i\mathbf{k}_j \cdot \mathbf{r}} \sigma_+^n a_j - a_j^\dagger e^{-i\mathbf{k}_j \cdot \mathbf{r}} \sigma_-^n \right], \quad (7.2)$$

where we index the states as shown in Figure 7.2. $\omega_j = ck_j$ is the frequency of the field mode, $\omega_2 - \omega_1 = \Delta_e$ is the electron Zeeman frequency, and $\hbar\omega_3$ is energy of the $|T_x-\rangle$ trion state. σ_{11} , σ_{22} and σ_{33} are the population operators, $|1\rangle\langle 1|$, $|2\rangle\langle 2|$, and $|3\rangle\langle 3|$. $\sigma_+^{n=1,2}$ is the raising operator for the atom ($|3\rangle\langle n=1,2|$) and $\sigma_-^n = (\sigma_+^n)^\dagger$. The $g_{n,j}$ are

$$g_{n,j} = -i \left(\frac{\omega_j}{2\hbar\epsilon_0 V} \right)^{1/2} \mu_{3n}; \quad n = 1, 2. \quad (7.3)$$

The system starts with the field in the vacuum state, so that the state vector for the system is,

$$|\Psi\rangle(t) = \sum_j a_{1,j}(t) |1, k_j, V\rangle + \sum_j a_{2,j}(t) |2, k_j, H\rangle + a_{3,0}(t) |3, 0\rangle. \quad (7.4)$$

where the first index labels the state of the atom and the second corresponds to the mode of the single photon. The system starts in the excited state which decays according to,

$$a_{3,0}(t) = e^{-\gamma_3 t/2} \Theta(t) \quad (7.5)$$

where γ_3 is the excited state decay rate. One can show that for times after the emission ($t \gg 1/\gamma_3$) [42],

$$|\Psi\rangle(t) = - \sum_j \frac{g_{1,j}}{\omega_B - \omega_j - i\gamma_3/2} e^{-i(\omega_1 + \omega_k)t} |1, k_j, V\rangle - \sum_j \frac{g_{2,j}}{\omega_R - \omega_j - i\gamma_3/2} e^{-i(\omega_2 + \omega_k)t} |2, k_j, H\rangle, \quad (7.6)$$

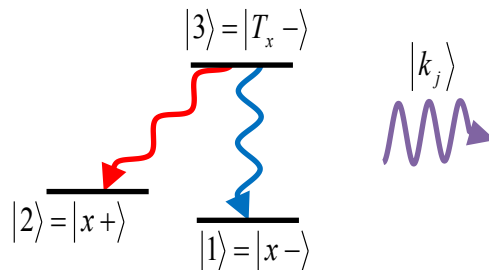


Figure 7.2: Energy level diagram for the states involved in lambda system decay.

where the center frequencies for the two transitions are $\omega_B = \omega_3 - \omega_1$ (blue) and $\omega_R = \omega_3 - \omega_2$ (red) which are frequency-mismatched since in the QD system, $\omega_B - \omega_R = \omega_2 - \omega_1 = \Delta_e > \gamma_3$. This means that the spontaneous emission from the two decay channels is frequency resolvable with only Lorentzian overlap.

The result is that the spin of the QD is entangled with both the polarization and frequency of the spontaneously emitted photon, which can be written as a hyper-entangled state of the form,

$$|\Psi\rangle = \frac{|\omega_R\rangle|H\rangle|x+\rangle - i|\omega_B\rangle|V\rangle|x-\rangle}{\sqrt{2}}, \quad (7.7)$$

where $|\omega_R\rangle$ (red) and $|\omega_B\rangle$ (blue) labels the frequency qubit.

Since we would like to verify the spin-polarization entanglement, we consider what effect the frequency qubit will have on our measurement. The density matrix of this

hyperentangled state is,

$$\hat{\rho}_{total} = \frac{1}{2} \begin{array}{c} \begin{array}{cccc} |1\rangle & |2\rangle & |3\rangle & |4\rangle \\ \left(\begin{array}{cccc} 1 & 0 & 0 & -i \\ 0 & 0 & 0 & 0 \\ 0 & 0 & 0 & 0 \\ i & 0 & 0 & 1 \end{array} \right) \\ \langle 1| \\ \langle 2| \\ \langle 3| \\ \langle 4| \end{array} \end{array} \quad (7.8)$$

where,

$$|1\rangle = |\omega_R\rangle \otimes (|x+\rangle|H\rangle) \quad (7.9)$$

$$|2\rangle = |\omega_R\rangle \otimes (|x-\rangle|V\rangle) \quad (7.10)$$

$$|3\rangle = |\omega_B\rangle \otimes (|x+\rangle|H\rangle) \quad (7.11)$$

$$|4\rangle = |\omega_B\rangle \otimes (|x-\rangle|V\rangle). \quad (7.12)$$

where the presence of the on and off diagonal terms are responsible for the entanglement. If the frequency of the photon is not detected, we trace over the frequency qubit resulting in,

$$\hat{\rho}_{spinpolarization} = \frac{1}{2} \begin{array}{c} \begin{array}{cc} |1'\rangle & |2'\rangle \\ \left(\begin{array}{cc} 1 & 0 \\ 0 & 1 \end{array} \right) \\ \langle 1'| \\ \langle 2'| \end{array} \end{array} \quad (7.13)$$

where $|1'\rangle = |x+\rangle|H\rangle$ and $|2'\rangle = |x-\rangle|V\rangle$, which is a mixed case for the spin-polarization state that exhibits no entanglement. So at first glance, it appears that if we average of the frequency information as with a normal broadband detector, the entanglement of a spin-polarization state is negligible due to the frequency mismatch of the two decay channels.

However, in 2005, *Economou et al.* showed that the spin-polarization entanglement can be measured by using a fast detection scheme that is capable of destroying the frequency information [42]. In this work, we use the fast detection process of a high timing resolution single photon detector to destroy the frequency information, which allows us to measure a spin-polarization entangled state. In the next Section, a simple quantum mechanical model of a fast detector is developed which lets us justify this technique theoretically.

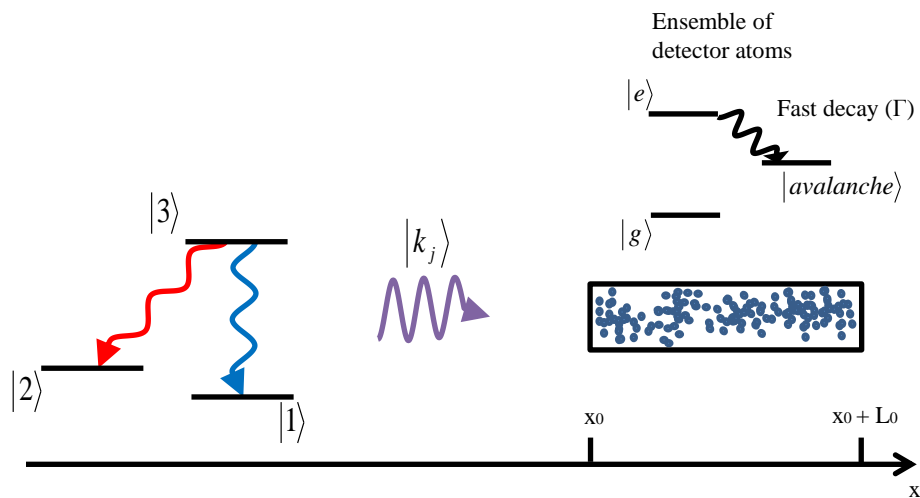


Figure 7.3: The spin-entangled photon is detected by a single photon detector, which we model as an ensemble of two-level detector atoms whose excited state rapidly decays to a avalanche or reservoir state of the detector. The source atom (QD) is taken to be at the origin, and the detector extends from x_0 to $x_0 + L_0$.

7.2 Theory of Frequency-Mismatched Spontaneous Emission

In order to study the effect of the frequency mismatch on spin-photon entanglement described in Section 7.1, we develop a simple quantum mechanical model of the photodetector, and study the effect of the photon detection process on the resulting state of the QD [117]. The setup of the problem is depicted in Figure 7.3, which is composed of a three-level lambda system, a single photon state of the field, and an ensemble of two-level detector atom's whose excited state ($|e\rangle$) rapidly decays to some macroscopic “avalanche” state ($|avalanche\rangle$) of the detector. The rapid decay from $|e\rangle$ to $|avalanche\rangle$ occurs at a rate Γ , which we associate with the inverse of the detector timing resolution.

To simplify the problem, the calculation is performed in one dimension, where we assume that the two orthogonal polarization components of the spontaneous emission are equally coupled to the detector with suitable polarization optics. The Hamiltonian

for this system is,

$$\begin{aligned}
H &= \sum_m \hbar\omega_d \sigma_{ee}^m + \sum_j \hbar\omega_j a_j^\dagger a_j \\
&+ \sum_m \sum_j \hbar g_j \left[e^{ik_j x_m} \sigma_+^m a_j - a_j^\dagger e^{-ik_j x_m} \sigma_-^m \right] \\
&+ \hbar\omega_2 \sigma_{22}^s + \hbar\omega_3 \sigma_{33}^s \\
&+ \sum_j \sum_{s=1,2} \hbar g_{j,s} \left[e^{ik_j x} \sigma_+^s a_j - a_j^\dagger e^{-ik_j x} \sigma_-^s \right], \tag{7.14}
\end{aligned}$$

where m indexes the detector atoms. ω_d is the detector atoms' center frequency, σ_{ee}^m is the population operator for detector atom m at location x_m . The source atom/QD (labeled by s) has levels $|1\rangle, |2\rangle, |3\rangle$ as shown in Figure 7.3, with state $|1\rangle$ taken at zero energy. j indexes the mode of the field k_j , where $\omega_j = ck_j$, and the other symbols have their usual meanings. The g 's are given by,

$$g_{j,s} = -i \left(\frac{\omega_j}{2\hbar\epsilon_0 AL} \right)^{1/2} \mu_{3s}; \quad s = 1, 2, \tag{7.15}$$

$$g_j = -i \left(\frac{\omega_j}{2\hbar\epsilon_0 AL} \right)^{1/2} \mu_d, \tag{7.16}$$

where A is the area of the detector, and L is the quantization volume. μ_{3s} is the dipole matrix element for the source atom (QD), and μ_d is the dipole matrix element for the detector atom, where both are taken to be real. The detector is modeled as a cylinder in the positive x direction that extends from x_0 to $x_0 + L_0$, and the source atom is located at the origin.

The state vector for the system can be written in an interaction representation as,

$$\begin{aligned}
|\Psi\rangle &= b_{3,g,0}(t) |3, g, 0\rangle e^{-i\omega_3 t} + \sum_j b_{1,g,n}(t) |1, g, k_j\rangle e^{-i\omega_j t} \\
&+ \sum_j b_{2,g,j}(t) |2, g, k_j\rangle e^{-i(\omega_2 + \omega_j)t} + \sum_m b_{1,m,0}(t) |1, m, 0\rangle e^{-i\omega_d t} \\
&+ \sum_m b_{2,m,0}(t) |2, m, 0\rangle e^{-i(\omega_2 + \omega_d)t}, \tag{7.17}
\end{aligned}$$

where the first index labels the state of the source atom (QD), the second labels the state of the detector atom which can either be in the ground state g or the detector

atom m can be excited. The ‘‘avalanche’’ state of the detector is not directly needed in the calculation so it is not included in the state vector. The third index labels the state of the single photon field which can be in the vacuum state or can be occupied with the mode k_j .

From Schrödinger’s equation, we can find the equations of motion for state amplitudes to be,

$$\dot{b}_{1,g,j}(t) = ig_{j,1}e^{-i(\omega_{31}-\omega_j)t}b_{3,g,0}(t) + i\sum_m g_j e^{-ik_j x_m} e^{-i(\omega_d-\omega_j)t}b_{1,m,0}(t), \quad (7.18)$$

$$\dot{b}_{2,g,j}(t) = ig_{j,2}e^{-i(\omega_{32}-\omega_j)t}b_{3,g,0}(t) + i\sum_m g_j e^{-ik_j x_m} e^{-i(\omega_d-\omega_j)t}b_{2,m,0}(t), \quad (7.19)$$

$$\dot{b}_{1,m,0}(t) = -i\sum_j g_j e^{ik_j x_m} e^{-i(\omega_j-\omega_d)t}b_{1,g,j}(t), \quad (7.20)$$

$$\dot{b}_{2,m,0}(t) = -i\sum_j g_j e^{ik_j x_m} e^{-i(\omega_j-\omega_d)t}b_{2,g,j}(t), \quad (7.21)$$

$$\dot{b}_{3,g,0}(t) = -i\sum_{s=1,2} g_{j,s} \sum_j e^{-i(\omega_j-\omega_{3s})t}b_{s,g,j}(t), \quad (7.22)$$

where $\omega_{31} = \omega_3 - \omega_1$ and $\omega_{32} = \omega_3 - \omega_2$.

A continuum description of the field is used by replacing $b_j(t)$ with $\sqrt{\frac{2\pi}{L}}b(k, t)$, \sum_j with $(\frac{L}{2\pi})\int_{-\infty}^{\infty} dk$, and ω_j with $\omega_k = ck$ so that the equations of motion are,

$$\dot{b}_{1,g}(k, t) = i\sqrt{\frac{L}{2\pi}}g_1 e^{-i(\omega_{31}-\omega_k)t}b_{3,g,0}(t) + i\sqrt{\frac{L}{2\pi}}\sum_m g_d e^{-ikx_m} e^{-i(\omega_d-\omega_k)t}b_{1,m,0}(t), \quad (7.23)$$

$$\dot{b}_{2,g}(k, t) = i\sqrt{\frac{L}{2\pi}}g_2 e^{-i(\omega_{32}-\omega_k)t}b_{3,g,0}(t) + i\sqrt{\frac{L}{2\pi}}\sum_m g_d e^{-ikx_m} e^{-i(\omega_d-\omega_k)t}b_{2,m,0}(t), \quad (7.24)$$

$$\dot{b}_{1,m,0}(t) = -ig_d\sqrt{\frac{L}{2\pi}}\int_{-\infty}^{\infty} e^{ikx_m} e^{-i(\omega_k-\omega_d)t}b_{1,g}(k, t)dk, \quad (7.25)$$

$$\dot{b}_{2,m,0}(t) = -ig_d\sqrt{\frac{L}{2\pi}}\int_{-\infty}^{\infty} e^{ikx_m} e^{-i(\omega_k-\omega_d)t}b_{2,g}(k, t)dk, \quad (7.26)$$

$$\dot{b}_{3,g,0}(t) = -i\sqrt{\frac{L}{2\pi}}\sum_{s=1,2} g_s \int_{-\infty}^{\infty} e^{-i(\omega_k-\omega_{3s})t}b_{s,g}(k, t)dk. \quad (7.27)$$

where the g ’s are evaluated at their appropriate center frequencies as in Weisskopf-Wigner theory.

We now wish to solve for analytic expression for the amplitudes $b_{1,m,0}(t)$ and $b_{2,m,0}(t)$, which will let us calculate the resulting state of the atom (QD) once a detector atom (m) has been excited. We begin with Equations 7.23 and 7.24 which are formally integrated and substituted into Equation 7.27. By neglecting the back action of the detector atoms on the source atom one finds,

$$\dot{b}_{3,g,0}(t) = \frac{L}{2\pi} \sum_{s=1,2} g_s^2 \int_0^t dt' \int_{-\infty}^{\infty} dk e^{-i(\omega_k - \omega_{3s})(t-t')} b_{3,g,0}(t') = -(\gamma_3/2) b_{3,g,0}(t), \quad (7.28)$$

where γ_3 is the one-dimensional excited state decay rate for the source atom. Taking the initial condition of the source atom starting in its excited state, we find,

$$b_{3,g,0}(t) = e^{-\gamma_3 t/2} \Theta(t), \quad (7.29)$$

where $\Theta(t)$ is the unit step function.

The fast detector model is now included by adding fast decay from $b_{1,m,0}(t)$ and $b_{2,m,0}(t)$ such that Equations 7.25 and 7.26 become,

$$\dot{b}_{1,m,0}(t) = -ig_d \sqrt{\frac{L}{2\pi}} \int_{-\infty}^{\infty} e^{ikx_m} e^{-i(\omega_k - \omega_d)t} b_{1,g}(k, t) dk - \frac{\Gamma}{2} b_{1,m,0}(t), \quad (7.30)$$

$$\dot{b}_{2,m,0}(t) = -ig_d \sqrt{\frac{L}{2\pi}} \int_{-\infty}^{\infty} e^{ikx_m} e^{-i(\omega_k - \omega_d)t} b_{2,g}(k, t) dk - \frac{\Gamma}{2} b_{2,m,0}(t). \quad (7.31)$$

where Γ is taken to be large compared to the other rates in the problem, so we can solve the equations for the quasi-static amplitudes,

$$b_{1,m,0}(t) \approx -\frac{2i}{\Gamma} g_d \sqrt{\frac{L}{2\pi}} \int_{-\infty}^{\infty} e^{ikx_m} e^{-i(\omega_k - \omega_d)t} b_{1,g}(k, t) dk, \quad (7.32)$$

$$b_{2,m,0}(t) \approx -\frac{2i}{\Gamma} g_d \sqrt{\frac{L}{2\pi}} \int_{-\infty}^{\infty} e^{ikx_m} e^{-i(\omega_k - \omega_d)t} b_{2,g}(k, t) dk. \quad (7.33)$$

We now show the details of the calculation only for $b_{2,m,0}(t)$ since these two equations are of similar form. Equation 7.33 and 7.29 are substituted into 7.24 to give,

$$\begin{aligned} \dot{b}_{2,g}(k, t) = & i \sqrt{\frac{L}{2\pi}} g_2 e^{-i(\omega_{32} - \omega_k)t} e^{-\gamma_3 t/2} \Theta(t) \\ & + \frac{2}{\Gamma} \frac{L}{2\pi} g_d^2 \sum_m \int_{-\infty}^{\infty} e^{i(k'-k)x_m} e^{-i(\omega_{k'} - \omega_k)t} b_{2,g}(k', t) dk', \end{aligned} \quad (7.34)$$

which can be solved by using Fourier transform technique where,

$$B_{s,g}(X, t) = \frac{1}{\sqrt{2\pi}} \int_{-\infty}^{\infty} e^{ikx} b_{s,g}(k, t) dk, \quad (7.35)$$

so that the Equation 7.34 becomes,

$$\begin{aligned} \dot{B}_{2,g}(x, t) &= i\sqrt{L}g_2 e^{-i\omega_{32}t} e^{-\gamma_3 t/2} \delta(x + ct) \Theta(t) \\ &+ \frac{2}{\Gamma} g_d^2 L \sum_m \delta(x - x_m + ct) B_{2,g}(x, t), \end{aligned} \quad (7.36)$$

and the sum is converted to an integral with $\sum_m \rightarrow NA \int_{x_0}^{x_0+L_0} dx_m$, where N is the density of detector atoms. In limit of $L_0 \rightarrow \infty$,

$$\begin{aligned} \dot{B}_{2,g}(x, t) &= i\sqrt{L}g_2 e^{-i\omega_{32}t} e^{-\gamma_3 t/2} \delta(x + ct) \Theta(t) \\ &- \frac{\alpha c}{2} \Theta(x - x_0 + ct) B_{2,g}(x, t). \end{aligned} \quad (7.37)$$

where $\alpha = \frac{2\omega_d N \mu_d^2}{\Gamma \epsilon_0 c \hbar}$ is the detector's absorption coefficient. This equation can be solved subject to the initial condition $B_{2,g}(x, 0) = 0$, to give,

$$\begin{aligned} B_{2,g}(x, t) &= \frac{i\sqrt{L}g_2}{c} e^{i\omega_{32}x/c} e^{\gamma_3 x/2c} \Theta(-x) \Theta(x + ct) \\ &\times \exp \left[-\frac{\alpha c}{2} \left(t + \frac{x - x_0}{c} \right) \Theta(x - x_0 + ct) \right]. \end{aligned} \quad (7.38)$$

So now equation Equation 7.33 can be written,

$$\begin{aligned} b_{2,m,0}(t) &= -\frac{2i}{\Gamma} \sqrt{\frac{L}{2\pi}} g_2 \int_{-\infty}^{\infty} e^{ikx_m} e^{-i(\omega_k - \omega_d)t} b_{2,g}(k, t) dk \\ &= -\frac{2i}{\Gamma} \sqrt{L} g_2 e^{i\omega_d t} B_{2,g}(x_m - ct, t). \end{aligned} \quad (7.39)$$

Combining Equations 7.38 and 7.39, we find that,

$$b_{2,m,0}(t) = -\frac{L}{\Gamma} \frac{g_d g_2}{c} e^{i(\omega_d - \omega_{32})t} e^{ik_{32}x_m} e^{-\frac{\gamma_3}{2} \left(t - \frac{x_m}{c} \right)} e^{-\frac{\alpha}{2} (x_m - x_0)} \Theta(ct - x_m), \quad (7.40)$$

where we have used that $(x_m - x_0) > 0$ and define $k_{i,j} = \omega_{i,j}/c$. Similarly for $b_{2,m,0}(t)$ one finds,

$$b_{1,m,0}(t) = -\frac{L}{\Gamma} \frac{g_d g_1}{c} e^{i(\omega_d - \omega_{31})t} e^{ik_{31}x_m} e^{-\frac{\gamma_3}{2} \left(t - \frac{x_m}{c} \right)} e^{-\frac{\alpha}{2} (x_m - x_0)} \Theta(ct - x_m). \quad (7.41)$$

Recall that these amplitudes correspond to the excitation of the detector atom m , and one of the ground state levels of the source atom. The decay rate Γ , which we identify as the inverse of the timing resolution, causes rapid relaxation to a reservoir state of the detector which heralds the presence of ground state coherence in the source atom. To calculate the resulting coherence, we have to average over all of the detector atoms since we do not know which one is excited, and normalize the result by the probability of the detector being excited.

$$\rho_{ij}(t) = \frac{\int_{x_0}^{x_0+L_0} dx_m b_{i,m,0}(t) [b_{j,m,0}(t)]^* e^{i\omega_{ji}t}}{\sum_{s=1}^2 \int_{x_0}^{x_0+L_0} dx_m |b_{s,m,0}(t)|^2}, \quad (7.42)$$

where L_0 can now be finite. The resulting source atom ground state coherence is,

$$\rho_{12}(t) = \frac{\mu_{31}\mu_{32}}{\mu_{31}^2 + \mu_{32}^2} \frac{\int_{x_0}^{x_0+L_0} e^{-\alpha(x_m-x_0)} e^{-\gamma_3(t-\frac{x_m}{c})} e^{ik_{21}x_m} \Theta(ct-x_m) dx_m}{\int_{x_0}^{x_0+L_0} e^{-\alpha(x_m-x_0)} e^{-\gamma_3(t-\frac{x_m}{c})} \Theta(ct-x_m) dx_m}, \quad (7.43)$$

where we assume $\omega_{32} \approx \omega_{31} \approx \omega_d$ except when these frequencies contribute to phases. In the limit of large absorption α or $k_{21}L_0 \ll 1$, the phase $e^{-ik_{21}x_m}$ is effectively constant over the integral. In the limit of $\alpha L_0 \gg 1$ and $\alpha \gg k_{21}, \gamma_3$,

$$\rho_{12} = \frac{\mu_{31}\mu_{32}}{\mu_{31}^2 + \mu_{32}^2} e^{ik_{21}x_0}. \quad (7.44)$$

So that by taking the dipole moment matrix elements to be equal for the two transitions we see that the coherence is its maximal value,

$$\rho_{12} = \frac{1}{2} e^{ik_{21}x_0}, \quad (7.45)$$

where the spatial phase ($e^{ik_{21}x_0}$) is a constant depending on x_0 , the distance between the source atom and the detector.

It is interesting to note that the phase factor inside the integral of Equation 7.43 has the effect of reducing the resulting ground state coherence if it is allowed to vary significantly. Since in our model of a fast detector, we choose the detector timing resolution to be sufficiently fast (large Γ), and the absorption to occur at the front of the detector (x_0), we are able to suppress the effect of the photon's frequency information, which would otherwise reduce the measurable entanglement fidelity since

the detector atoms could in principle measure which decay channel occurred. Since the frequency information is destroyed by the rapid detection process, the detector atoms do not have time to be sensitive to the frequency mismatch. This can be interpreted as an example of a “quantum eraser” experiment where the frequency “which-path” information is erased by the fast detection process [42, 60, 117, 118]. If spontaneous emission is viewed as a quantum jump process, we can consider the fast detection as providing a measurement of the (retarded) emission time of the photon, which initializes the QD to a coherent superposition of the ground states, indirectly proving that a spin-photon entangled state existed before the photon is measured.

7.3 Spin-Photon Entanglement Experiment

In the last two sections we theoretically justified the existence of a spin-photon entangled state of the form,

$$|\Psi\rangle = \frac{|H\rangle|x+\rangle - i|V\rangle|x-\rangle}{\sqrt{2}}, \quad (7.46)$$

which is created by spontaneous decay from the $|T_x-\rangle$ state.

It is clear from Equation 7.46, that the spin and polarization are correlated, but in order to experimentally demonstrate that this is an entangled state, we have to show that the spin and polarization remain correlated in two different bases of measurement. First, we show that in the computational (x -basis/eigenbasis) that detection of an H polarized photon is correlated with $|x+\rangle$, and a V photon is correlated with $|x-\rangle$. Then, in a rotated basis (z -basis), we show that detection of a circularly polarized photon ($\sigma\pm$) is correlated with measuring the QD in a superposition of x -basis states ($|z\pm\rangle$), where the correlation is time-dependent due to the precession of spin at the electron Zeeman frequency. This spin precession is related to the frequency-mismatch problem of the previous sections, since the measurement of a circularly polarized photon initializes the QD spin to a superposition state ($|z\pm\rangle$), however the exact time of the photon measurement varies over the lifetime of the trion state (≈ 1 ns).

In order to observe this time-dependent correlation, our detector’s timing reso-

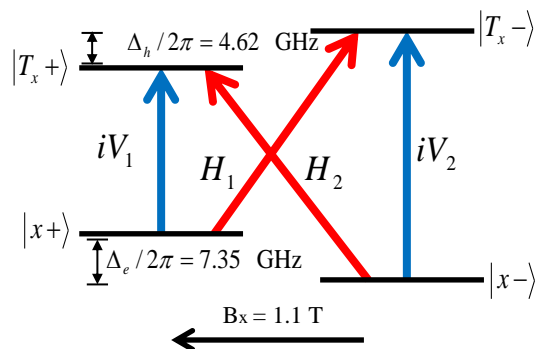


Figure 7.4: Energy level diagram including the electron and hole Zeeman frequencies for the magnetic field used in this work. The electron Zeeman frequency is kept as small as possible, while keeping the hole/trion splitting large enough to use frequency selective excitation. The optical energy splitting is approximately 1.305 meV (10523.5cm^{-1}).

lution (48 ps FWHM) must be faster than the precession period. As described in Chapter 6, an externally applied magnetic field sets the electron and trion energy splittings. The magnetic field is chosen to be large enough to sufficiently split the energy levels, allowing for frequency selective excitation, while simultaneously keeping the electron Zeeman frequency small enough to temporally resolve the rotated basis correlation. For the charged QD studied here, this corresponds to a magnetic field of 1.1 T which sets the electron (hole) Zeeman frequency to 7.35 GHz (4.62 GHz)(Figures 7.4,7.5) so that the detector timing resolution is $\approx 2.8\times$ faster than the electron spin precession period (136 ps).

The experiments are performed with the QD sample held at approximately 7 K in the magnetic optical cryostat described in Chapter 6. The experimental setup is shown in Figure 7.6. The narrow-bandwidth resonant optical pulses used to drive the QD are generated with a pair of narrow band Ti:sapphire lasers (Coherent 899:21, 899:29 models) that are time gated with with EOMs (Chapter 4) to create a 250 ps pulse which serves to excite the system to the $|T_x-\rangle$ trion state, and a 4 ns optical

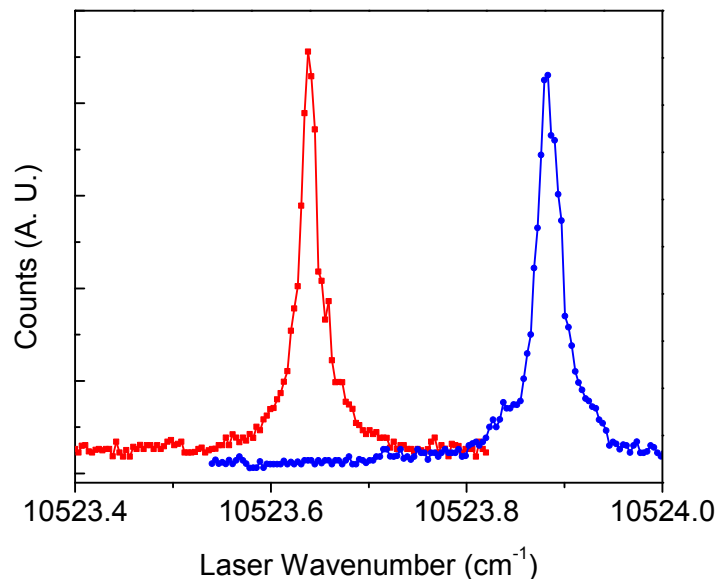


Figure 7.5: Fluorescence recorded as function of the excitation laser frequency showing the 7.35 GHz splitting between the two transitions of the right lambda system.

pumping pulse which serves to initialize the system to a pure state. Photons scattered/emitted during/after these resonant pulses are used to provide a spin readout channel. The cw lasers are independently intensity stabilized using traveling wave acousto-optic modulators before being coupled into the EOMs. In the rotated basis measurements, a mode-locked Ti:sapphire laser is used (Coherent MIRA 900 model) to generate red detuned (1 meV) 2 ps pulses which rotate the QD spin state by driving the stimulated Raman transition (Chapter 6). For the rotated basis measurements, the pulse generator driving the EOMs is externally triggered by a fast photodiode monitoring the mode-locked laser's pulse train (repetition rate ≈ 76 MHz), which serves as the master clock.

Light is collected in the transmission geometry using the aspheric lens setup described in Chapter 3. For all the measurements, the excitation lasers are cross polarized relative to the measurement axis of QD photons, which allows us to block the excitation lasers. In addition to the polarization rejection, the excitation lasers are aligned at a slight angle ($\approx 2 - 5$ mrad) relative to the collection axis. This allows

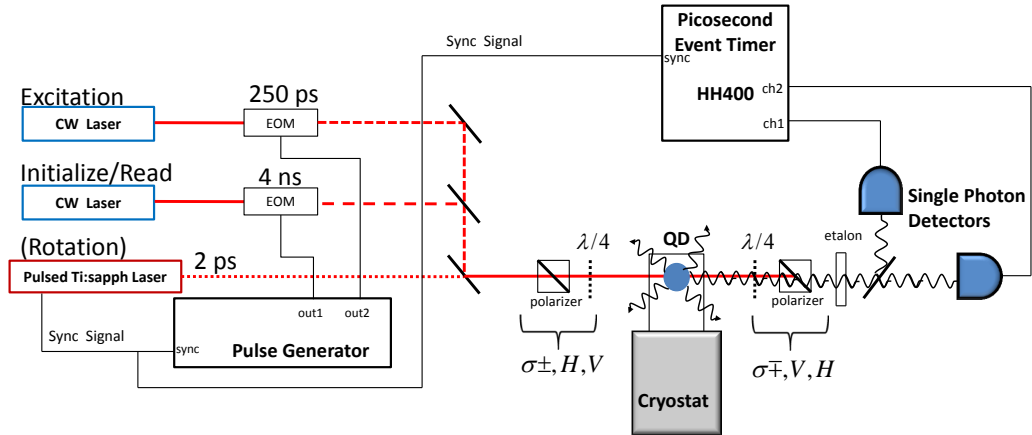


Figure 7.6: The experimental setup used in the spin-photon entanglement experiments. The QD is held in the magnetic optical cryostat at 7 K. Two cw lasers are modulated with EOMs to generate resonant 250 ps and 4 ns pulses. A mode-locked Ti:sapphire laser is used in the rotated basis measurements to rotate the spin state. The lasers are polarized before the cryostat with a combination of polarizer and quarter-wave plate. Light is collected in the transmission geometry. Another quarter-wave plate and polarizer are used to set the photon detection axis and to filter out the excitation lasers. In the rotated basis measurement, an etalon is used to further suppress the detuned pulses from the modelocked laser. The QD light is split and sent to a pair of single photon detectors. Detection events are time-tagged with a picosecond event timer synchronized with the laser's repetition rate.

us to achieve an overall rejection ratio exceeding 70 dB for the resonant excitation pulses. For the rotated basis measurements, a large bandwidth etalon (described in Chapter 6) is used to spectrally reject the detuned 2 ps pulse. Light from the QD is coupled into a single mode fiber which is split with a 50:50 fiber splitter and sent to a pair of single photon detectors. In the computational basis measurements, high timing resolution is not required to observe the spin-polarization correlation, so two of the high detection efficiency (τ -SPAD model) detectors are used. In the rotated basis measurements, the fast (48 ps) timing resolution (PDF model) detector is required to measure the entangled photon, but the high detection efficiency detector is used to read out the QD spin state. Since we are dedicating each detector to a specific measurement, the success rate is reduced by a factor of 2; however, the higher detection efficiency increases the success rate by a factor of 10, yielding a factor of 5 total gain. The detection events from each detector are independently time-tagged relative to the experimental clock by the HH400 picosecond event timer operating in “T3” mode (see Chapter 4). All detection events are written to disk and post-processed to calculate the correlations.

Six independent experiments are performed to measure eight conditional probabilities, $P(x\pm|H)$, $P(x\pm|V)$, $P(z\pm|\sigma+)$, and $P(z\pm|\sigma-)$, which are used to calculate a lower bound on the entanglement fidelity using the expression [20],

$$\begin{aligned} \mathcal{F} \geq 1/2 & (\rho_{Hx+,Hx+} + \rho_{Vx-,Vx-} - 2\sqrt{\rho_{Hx-,Hx-}\rho_{Vx+,Vx+}} \\ & + \rho_{\sigma+z-, \sigma+z-} - \rho_{\sigma+z+, \sigma+z+} + \rho_{\sigma-z+, \sigma-z+} - \rho_{\sigma-z-, \sigma-z-}), \end{aligned} \quad (7.47)$$

where the density matrix elements are taken to be 1/2 of the appropriate conditional probability. The first four measurements are performed in the computational basis to obtain independent measures of $P(x+|H)$, $P(x-|H)$, $P(x+|V)$, and $P(x-|V)$. Two independent experiments are performed in the rotated basis projecting the photon polarization to $\sigma+$ and $\sigma-$, and since the correlation is time dependent, we are about to extract $P(z\pm|\sigma+)$, and $P(z\pm|\sigma-)$ from these measurements.

7.3.1 Computational Basis Experiments

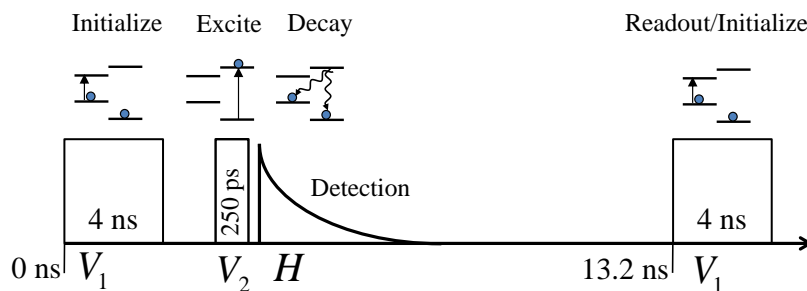


Figure 7.7: The spin is initialized with a 4 ns optical pumping pulse, and then excited with a 250 ps (π -area) pulse to the $|T_x-\rangle$ state which decays, emitting the spin-entangled photon. If an H photon is detected, the spin is projected to the $|x+\rangle$ state, so the probability of scattering a photon during the next 4 ns pulse (which now serves to readout the spin) is 1. If no photon is detected, the probability of scattering a photon with the 4 ns readout pulse is 0.5.

In the computational (x) basis, we verify that detecting an H polarized photon is correlated with measuring the spin in the $|x+\rangle$ state, and that detecting a V polarized photon is correlated with $|x-\rangle$. These experiments are performed with the pulse sequence as shown in Figure 7.7.

For the H measurement, the system is first initialized to the $|x-\rangle$ state with a 4 ns optical pumping pulse resonant on transition V_1 with an effective Rabi frequency of $\Omega_0 \approx 1$ GHz. Then, a 250 ps (π -area) pulse resonant on the V_2 transition excites the system to the $|T_x-\rangle$ state. The $|T_x-\rangle$ state decays, emitting the spin-entangled photon. If an H polarized entangled photon is detected, the following 4 ns pulse (from the next cycle) can serve to read out the $|x+\rangle$ population by scattering a single H readout photon while it re-initializes the system for the next run of the experiment. Since the photons are time-tagged relative to the experimental clock, the temporal location of the photon allows us to identify it an entangled photon or a readout photon (Figure 7.8).

Given that the detection efficiency is much less than 1, and that the two decay channels to $|x+\rangle$ and $|x-\rangle$ are equally likely, if no entangled photon is detected, the

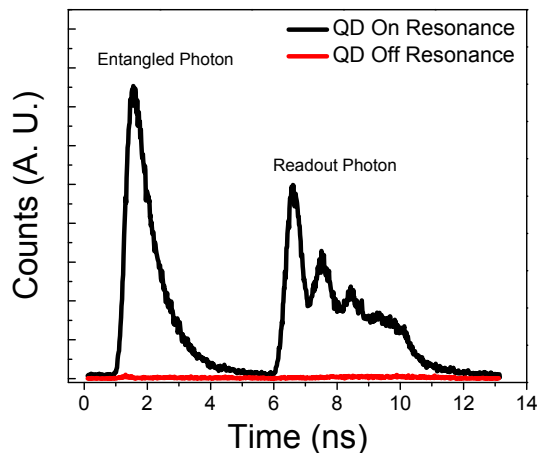


Figure 7.8: An example of a time-histogram of a typical computational basis measurement. The black (red) shows the signal (background) when the QD is tuned on (off) resonance with the DC Stark shift. The entangled photon is generated following the 250 ps (π -area) excitation pulse. Here, the readout photon is generated during the 4 ns pulse which re-initializes the system by optical pumping. The oscillations during the readout are Rabi oscillations at a frequency of ≈ 1 GHz.

spin is equally likely to be measured in either ground state, so the probability of scattering a readout photon is $1/2$. Using this, we are able to normalize the conditional probabilities by comparing the number of entangled photon-readout photon correlations for the same shot of the experiment to the number of correlations between temporally distant shots of the experiment which corresponds to a conditional probability of $1/2$ since these events are uncorrelated (see Figure 7.9).

As an independent check, we measure the anti-correlation between detecting an H photon and measuring the spin in the $|x-\rangle$ state (Figure 7.10). This is performed by inserting an additional 250 ps pulse resonant with the V_2 transition, after $|T_x-\rangle$ decays but before the next 4 ns pulse, which serves to read out the population in the $|x-\rangle$ state. So that if an H is detected, the probability of scattering a readout off V_2 is 0. The conditional probabilities are again normalized by comparing the number of same shot correlations to the number of correlations between temporally distant shots of the experiment.

For the excitation (readout) pulses, detection of an H photon indicates that the

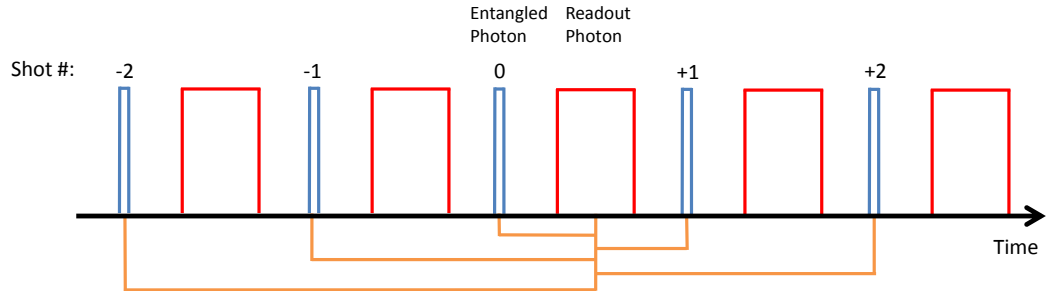


Figure 7.9: The conditional probabilities are normalized by comparing the number of entangled photon-readout photon correlations for the same shot of the experiment to the number of correlations for temporally distant (uncorrelated) shots of the experiment which correspond to a conditional probability of 0.5.

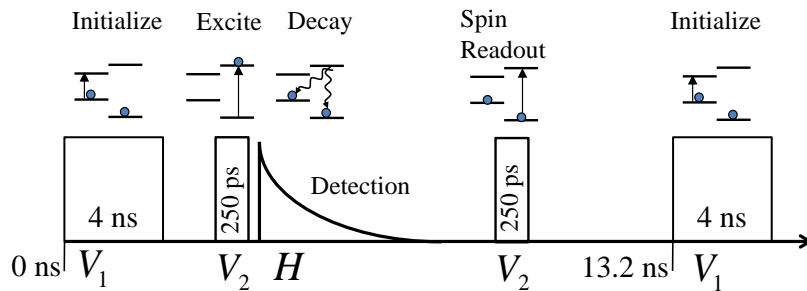


Figure 7.10: As an independent check, we perform a correlation measurement verifying that detection of an H photon is anti-correlated with measuring the spin in the $|x-\rangle$ state, by inserting an additional 250 ps spin readout pulse on V_2 that reads out the $|x-\rangle$ population after the photon is detected, but before the spin is re-initialized.

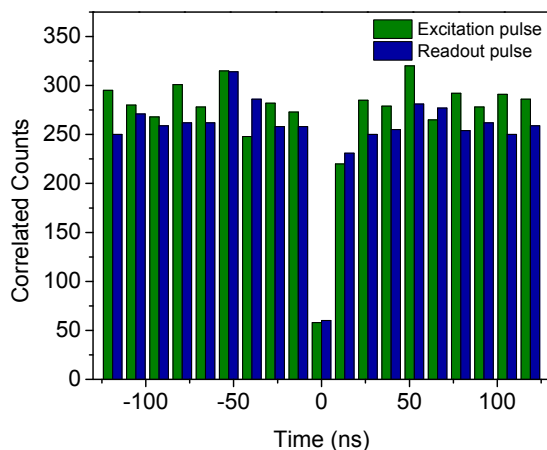


Figure 7.11: Anti-bunching for the excitation pulse and readout pulse showing a nonzero signal at time zero, arising from re-excitation due to off-resonant coupling of the pulses. This background is used to correct the raw spin-photon correlation data.

spin has been initialized to the $|x+\rangle$ ($|x-\rangle$) state, so that the probability of detecting two photons associated with either one of these pulses should be zero (similar to antibunching). However, off-resonant coupling of the pulses to the undesired transition can lead to a trion getting re-excited, where it can scatter another erroneous photon. These erroneous photons contribute a systematic background to the computational basis measurements, which we can measure by counting the number of entangled photon-entangled photon correlations and readout photon-readout photon correlations for the same shot of the experiment Figure 7.11.

We can use these events to measure the likelihood of emitting a spurious photon from either the excitation or readout pulses, which goes like $P(\text{EntangledPhoton}) \times P(\text{Error}_{\text{ExcitationPulse}})$ and $P(\text{ReadoutPhoton}) \times P(\text{Error}_{\text{ReadoutPulse}})$. By scaling these correlations by the ratio of entangled photons to readout photons, we can estimate the number of erroneous correlations between the entangled and readout photons. The dominant contribution to this error is proportional to $P(\text{EntangledPhoton}) \times P(\text{Error}_{\text{ReadoutPulse}})$ and $P(\text{ReadoutPhoton}) \times P(\text{Error}_{\text{ExcitationPulse}})$. Since this background contributes equally across time bins, these counts are subtracted from the raw data before they are normalized to correct for this systematic error (Fig-

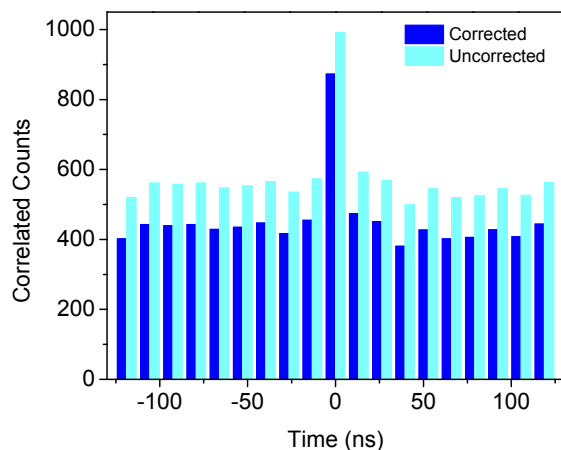


Figure 7.12: An example the raw and corrected computational basis correlation data which both show a clear positive correlation signal at time zero. The uncorrelated distant runs are used to normalized the conditional probabilities.

ure 7.12).

The conditional probabilities for the two H measurements ($P(x+|H)$, $P(x-|H)$) are then normalized requiring that their sum equals 1. We obtain the conditional probabilities of $P(x+|H) = 0.94 \pm 0.05$ and $P(x-|H) = 0.06 \pm 0.01$. The raw data, without background subtraction or normalization, give $P(x+|H) = 0.91 \pm 0.03$ and $P(x-|H) = 0.12 \pm 0.04$.

We repeat this measurement detecting V polarized photons, where the excitation lasers are now horizontally polarized. The 4 ns pulse is now resonant on the H_2 transition which initializes the QD to the $|x+\rangle$ state, and the 250 ps (π -area) pulse is resonant on the H_1 transition exciting the system to $|T_x-\rangle$.

The data are analyzed the same way as in the H measurement, and we obtain condition probabilities: $P(x-|V) = 0.84 \pm 0.04$, $P(x+|V) = 0.16 \pm 0.01$. The uncorrected values are $P(x-|V) = 0.68 \pm 0.02$ and $P(x+|V) = 0.25 \pm 0.02$. In this configuration, the effect of off-resonant coupling is more pronounced because the excitation lasers are driving the “ H ” transitions which are the closest in energy. The background subtraction method is able to partially correct for this error, however it is unable to correct for the off resonant coupling’s effect on reducing the initialization

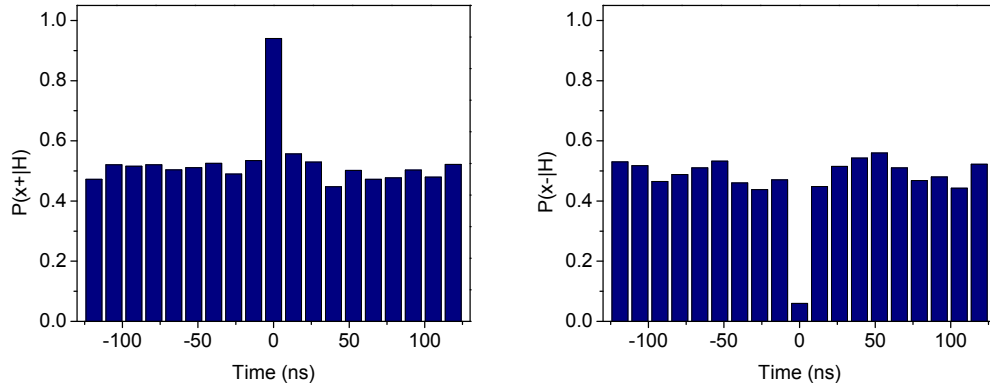


Figure 7.13: Normalized spin-photon correlation data for the $P(x+|H)$ and $P(x-|H)$ measurements showing a correlation between detecting an H photon and measuring the spin in the $|x+\rangle$ state.

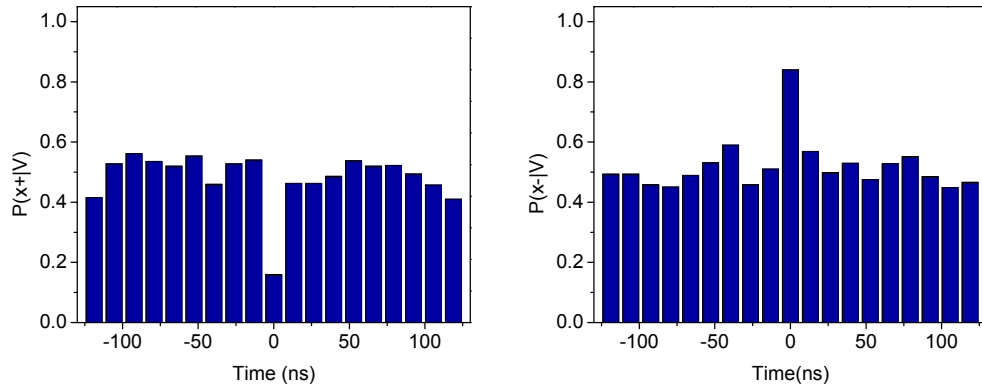


Figure 7.14: Normalized spin-photon correlation data for the $P(x+|V)$ and $P(x-|V)$ measurements showing a correlation between detecting an V photon and measuring the spin in the $|x-\rangle$ state.

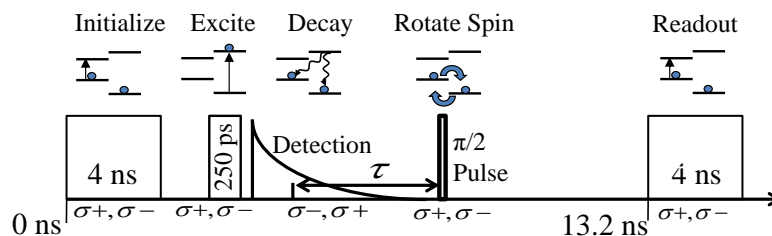


Figure 7.15: Timing diagram for the rotated basis measurements.

fidelities. Combining the H and V measurements, we can calculate a lower bound on the computational basis fidelity of 0.79 ± 0.03 using,

$$\mathcal{F}_c \geq \rho_{Hx+,Hx+} + \rho_{Vx-,Vx-} - 2\sqrt{\rho_{Hx-,Hx-}\rho_{Vx+,Vx+}}. \quad (7.48)$$

7.3.2 Rotated Basis Correlation

The final two measurement are performed in the rotated (z) basis, where we project the photon state to $|\sigma_{\pm}\rangle$ which initializes the spin to a superposition of the x -basis eigenstates ($|z_{\pm}\rangle$). Since the eigenstates are not degenerate, the correlation signal is now time dependent. The timing diagram is shown in Figure 7.15. The excitation lasers are now circularly polarized, orthogonal to the detection axis, where we again use the frequency of the excitation pulses to spectrally isolate specific transitions. The spin is initialized to the $|x-\rangle$ state, with a 4 ns pulse resonant on the V_1 transition, followed by a 250 ps (π -area) pulse resonant with the V_2 transition which excites the system to the $|T_x-\rangle$, which decays, resulting in the spin-entangled photon.

$$|\Psi\rangle = \frac{|H\rangle|x+\rangle - i|V\rangle|x-\rangle}{\sqrt{2}}, \quad (7.49)$$

The photon state is measured along σ_{\pm} using a quarter-wave plate and polarizer before the single photon detector. Here, the fast (48 ps FWHM) timing resolution

detector described in Chapter 4 is used to detect the entangled photon, so that at time zero, the spin is projected to the state,

$$\langle \sigma \pm | \Psi \rangle = \frac{|x+\rangle \mp |x-\rangle}{2}, \quad (7.50)$$

this undergoes unitary evolution according to Schrödinger's equation for a time τ ,

$$\hat{U}(\tau) \langle \sigma \pm | \Psi \rangle = \frac{e^{-i\Delta_e \tau} |x+\rangle \mp |x-\rangle}{2}, \quad (7.51)$$

so that as τ varies, the spin state oscillates between $|z\pm\rangle$. In order to observe this time varying correlation signal, a 2 ps $\pi/2$ (Raman) pulse (Chapter 6) rotates the spin measurement basis, so that the coherence is mapped into an x -basis probability amplitude. Recall, that the operator for the rotation pulse can be written as,

$$\hat{R}_{\sigma\mp} = \frac{1}{\sqrt{2}} (|x+\rangle \langle x+| \pm i |x+\rangle \langle x-| \pm i |x-\rangle \langle x+| + |x-\rangle \langle x-|) \quad (7.52)$$

so that following the rotation pulse the state is,

$$\hat{R}_{\sigma\mp} \hat{U}(\tau) \langle \sigma \pm | \Psi \rangle = \frac{(e^{-i\Delta_e \tau} - i) |x+\rangle \mp (1 - ie^{-i\Delta_e \tau}) |x-\rangle}{2\sqrt{2}}. \quad (7.53)$$

The next 4 ns pulse serves to read out the $|x+\rangle$ population so that the resulting signal is proportional to,

$$\begin{aligned} |\langle x+ | \hat{R}_{\sigma\mp} \hat{U}(\tau) \langle \sigma \pm | \Psi \rangle|^2 &= \frac{(e^{-i\Delta_e \tau} - i)(e^{+i\Delta_e \tau} + i)}{8} \\ &= \frac{1}{4} (1 + \sin(\Delta_e \tau)). \end{aligned} \quad (7.54)$$

We see that the signature of the rotated basis correlation is an coincidence oscillation at the electron Zeeman frequency. Since the lifetime (≈ 1 ns) is longer than the this oscillation period (136 ps), the time τ varies automatically. The number of coincidences is weighted by the trion decay's exponential envelope, so that the form of the measured signal for times t after the excitation pulse is,

$$signal \propto (1 + \alpha \sin(\Delta_e \tau + \phi_0)) e^{-\gamma_2 t} \Theta(t), \quad (7.55)$$

where we have allowed for imperfect contrast (α), and a phase shift ϕ_0 . An example of the theoretical signal convolved with the detector's instrument response function

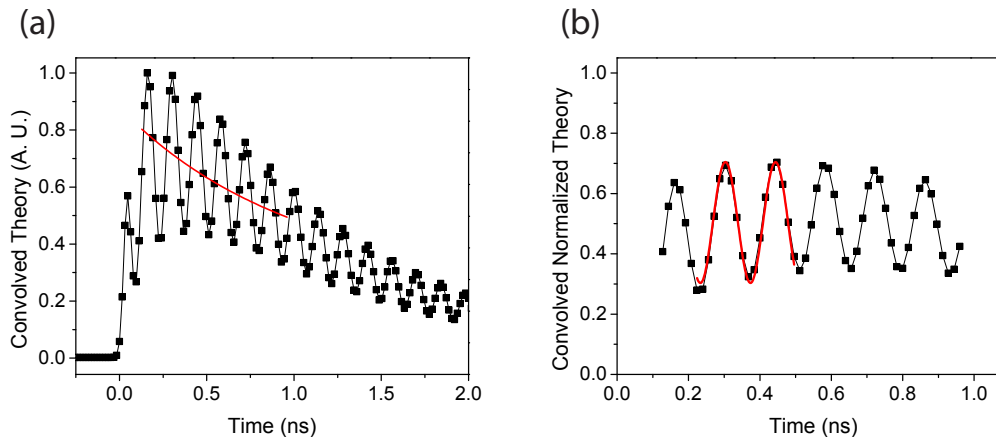


Figure 7.16: (a) Black: The theory (Equation 7.55 is convolved with the detector’s instrument response function to show the form of the expected signal. Red: An exponential fit to the theoretical signal is used to normalize to a conditional probability. (b) Black: Theoretical signal after dividing out by the exponential fit. Red: A fit to the convolved normalized theory yields a fringe contrast of 0.4, which limits the maximum obtainable entanglement fidelity to 0.7.

is shown in Figure 7.16. After dividing out by the exponential envelope and fitting to the convolved theory, we see that the maximum achievable contrast (α) is 0.4, due to the temporal convolution of the theoretical signal with the 48 ps detector response. This temporal convolution limits the maximum achievable entanglement fidelity of the experiment to 0.7. An example of the correlation data before dividing out by the exponential is shown in Figure 7.17.

We perform two independent measurements, projecting the photon state to $\sigma+$ and $\sigma-$. The number of entangled photon-readout photon coincidences are binned as function of the entangled photon detection time. The data (after dividing out by the exponential envelope) is shown in Figure 7.18. The data are fit to the expression $(1 + \alpha \sin(\Delta_e \tau + \phi_0))$, and from the two fringe contrasts (α), we are able to extract four rotated basis conditional probabilities: $P(z - |\sigma+) = 0.70 \pm 0.05$, $P(z + |\sigma+) = 0.30 \pm 0.05$, $P(z - |\sigma-) = 0.31 \pm 0.04$, and $P(z + |\sigma-) = 0.69 \pm 0.04$.

7.3.3 Spin-Photon Entanglement Results

Combining the computational and rotated basis results (Figure 7.19), we are able

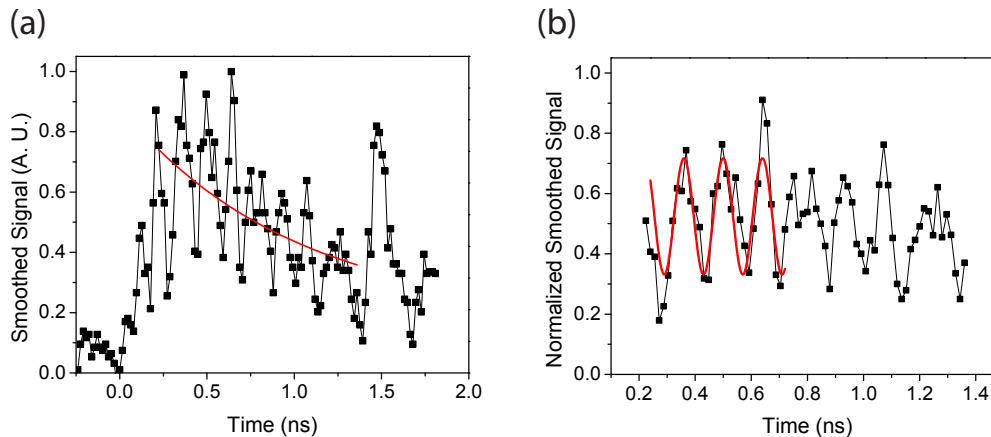


Figure 7.17: (a) Black: Rotated basis correlation signal showing oscillations at the electron Zeeman frequency with an exponential envelope. Here the data are binned at 16 ps time bins and smoothed. The spike at 1.5 ns is the residual rotation pulse leak through which is not completely blocked by the rejection setup. Red: An exponential fit to the data is used to normalize the rotated basis conditional probabilities. (b) Black: after dividing out by the exponential envelope, we observe the coincidence signal whose fringe contrast is consistent with theoretical limit. Red: A sinusoidal fit is overlaid as a guide to the eye.

to put a lower bound on the entanglement fidelity of $\mathcal{F} \geq 0.59 \pm 0.04$ [43], which is limited primarily by the temporal convolution of the rotated basis signal with the detector’s instrument response function. Taking this into account, we are able to achieve 84% of the detector limited fidelity. The remaining reduction in fidelity arises primarily from off-resonant coupling in the V polarized measurements which reduces the initialization fidelity.

Recently, *De Greve et al.* have reported spin-photon entanglement fidelities of 0.8 using a nonlinear frequency downconversion technique [62]. By mixing the entangled photon with a short (8 ps) pump pulse, they are able to time gate their single photon detector, effectively setting their timing resolution to 8 ps, at the expense of count rate. However, for future studies, such as using intermediate spin-photon entangled states to mediate probabilistic spin-spin entanglement [5], fast (sub-ns) timing resolution is not required, so that by using larger magnetic fields, near unity spin-spin entanglement fidelities are in principle realizable in our approach. This and other

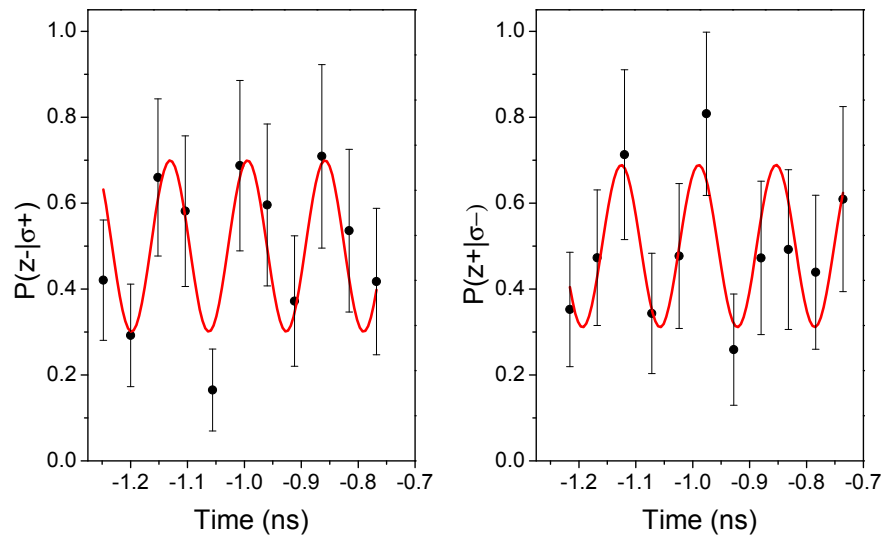


Figure 7.18: Black: Rotated basis correlation data used to extract the conditional probabilities. The raw data are time binned relative to the rotation pulse with 48 ps time bins and the exponential envelope is divided out. Red: The data are fit using the experimentally determined Zeeman frequency, 7.35 GHz. We fit to the first three periods where the signal to noise is the highest. The fringe contrasts are 0.40 ± 0.10 for $\sigma+$ and 0.38 ± 0.08 for $\sigma-$.

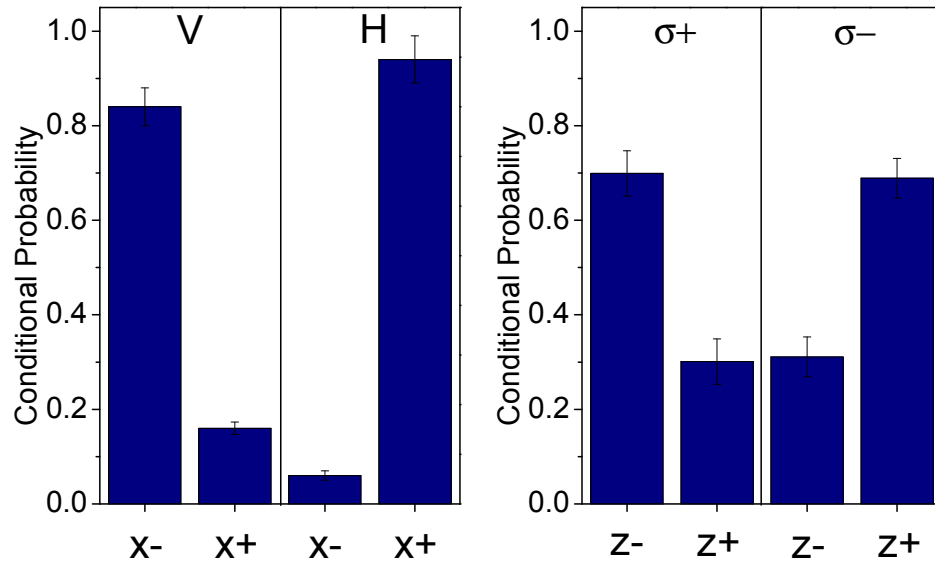


Figure 7.19: Conditional probabilities for the computational (x) and rotated (z) basis measurements.

applications will be discussed further in the Chapter 8.

7.4 Chapter Summary

In this Chapter, we have presented the theory and experimental demonstration of a QD spin-photon entangled state. Projective correlation measurements are performed in two bases to verify that the spin and polarization state are entangled. This spin-photon entanglement is an important step towards realizing a scalable quantum information architecture based on optically driven QD spins.

CHAPTER 8

Conclusions and Future Directions

In this work, we have pursued quantum information applications of optically driven QD spins. The spin of a single electron confined to an InAs QD has been shown to form a useful single qubit for quantum information applications [1, 2], and now the primary challenge in realizing a practical quantum information architecture resides in scaling the system to a multiple spin system. In our approach, we use intermediate spin-photon entangled states to mediate entanglement between distant QD spins. The first steps toward achieving this goal are isolating single photons emitted from the QD and showing that the generation of a spin-photon entangled state is realizable, which is the subject of this thesis. Future studies will build upon these achievements to pursue the realization of an elementary quantum network based on QD spins coupled by photons.

8.1 Results Summary

The primary achievement of this work is the successful demonstration of a QD spin-photon entangled state (Chapter 7). In order to accomplish this, a new sample and optical design is implemented and quantum optics techniques are applied to the QD system, allowing for the demonstration of QD resonance fluorescence (Chapter 3). Then, time correlated single photon counting techniques are applied to the QD system, and programmable optical pulses are generated using waveguide electro-optic modulators, providing frequency selective excitation of specific QD transitions (Chapter 4). Combining these techniques, lifetime measurements, time dependent

Rabi oscillations, and photon antibunching under resonant excitation are demonstrated (Chapter 5). These techniques are then applied to the QD spin system in the presence of an externally applied magnetic field to realize the optically coupled spin qubit. State initialization through resonant optical pumping, and coherent manipulation of the QD spin using detuned pulses driving a stimulated Raman transition are demonstrated, where the QD spin state is read out by scattering a single photon (Chapter 6). Finally, a QD spin-photon entangled state is demonstrated (Chapter 7), which will be integral to future applications of scaling the QD spin architecture.

8.2 Applications of a Spin-Photon Entangled State

The QD spin-photon entangled state is the first step towards scaling the QD spin system using intermediate photon states. On its own, this state represents a hybrid entangled state between two qubits: a matter qubit (the QD spin), and flying qubit (the polarization state of a single photon). A natural extension to this work is extending the system to three qubits, then four qubits, and so on to build up a quantum network of coupled QD spins. Here, some possible extensions of this work are explored including practical considerations about the experimental realization of such protocols.

8.2.1 Quantum Teleportation: Three Qubit System

The spin-photon entangled state can be used to demonstrate a quantum teleportation scheme between a photon state and the resulting state of the QD spin (shown in Figure 8.1). A single input photon is prepared in a coherent superposition of two modes, forming a frequency qubit of the form,

$$|\psi_{input}(t)\rangle = \frac{c_R|\omega_R\rangle + c_B e^{-i\Delta_e(t-t_c)}|\omega_B\rangle}{\sqrt{2}}, \quad (8.1)$$

where $|\omega_R\rangle$ (red) and $|\omega_B\rangle$ (blue) labels the frequency qubit, $\Delta_e = \omega_B - \omega_R$ is set to match the electron Zeeman frequency, t_c is the “creation” time of the state, and the state amplitudes c_R and c_B are controlled by the preparation of the photon. The single photon can be prepared by exciting a neutral QD to a coherent superposition

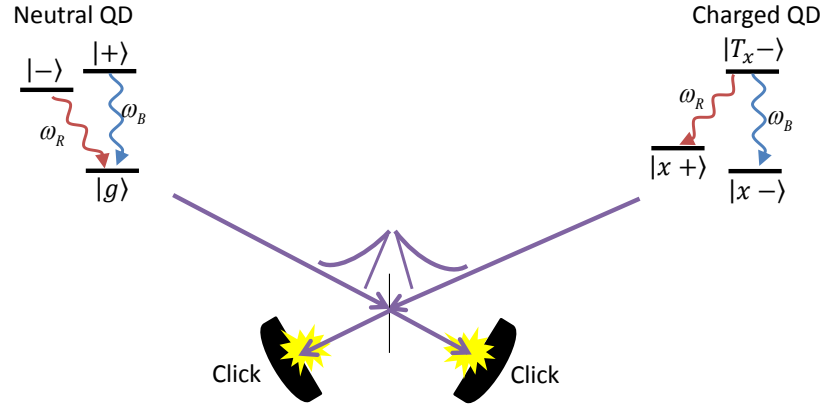


Figure 8.1: A single photon frequency qubit, generated by exciting a single neutral QD to a coherent superposition of its excited states, can be teleported to the QD spin state by measuring coincident detector clicks in a H.O.M. interferometer. The resulting spin state is then read out to verify that the state is transferred.

of its excited states, which are part of a three level “V” system [119]. When the QD decays, the excited state amplitudes are mapped onto a coherent superposition of the photon states as in Equation 8.1. Alternatively, the input photon can be created by a heralded spontaneous parametric down-converted single photon source whose bandwidth, and frequency is matched to the QD. An electro-optic phase modulator can be used to generate a coherent superposition of two frequency modes.

Recall that spin-photon entangled of Chapter 7 can be written as,

$$|\Psi\rangle = \frac{|\omega_R\rangle|H\rangle|x+\rangle - i|\omega_B\rangle|V\rangle|x-\rangle}{\sqrt{2}}, \quad (8.2)$$

In order to observe the spin-photon polarization entangled state a fast detection scheme is used in Chapter 7 to destroy this frequency information. However, if the photon state is projected along a circular polarization, with a suitable waveplate and polarizer combination, the resulting state can be written as,

$$|\psi_{spin-freq}\rangle = |\sigma-\rangle\langle\sigma-|\Psi\rangle = \frac{(|\omega_R\rangle|x+\rangle + |\omega_B\rangle|x-\rangle)|\sigma-\rangle}{\sqrt{2}}, \quad (8.3)$$

which is a spin-frequency entangled state.

The photons are mixed on a 50-50 beam splitter resulting in the state vector,

$$|\psi_{input}(t)\rangle \otimes |\psi_{spin-freq}\rangle. \quad (8.4)$$

The two detectors simultaneously click only if the photons are in the antisymmetric state [22],

$$|\psi_{asym}\rangle = \frac{1}{\sqrt{2}}(|\omega_R\rangle_a|\omega_B\rangle_b - |\omega_B\rangle_a|\omega_R\rangle_b), \quad (8.5)$$

so coincident clicks project the state vector to the QD state at time t_d ,

$$\begin{aligned} |\psi_{QD}(t)\rangle &= \frac{1}{\sqrt{2}}(c_R|x-\rangle + e^{-i\Delta_e(t-t_d)}e^{-i\Delta_e(t_d-t_c)}c_B|x+\rangle) \\ &= \frac{1}{\sqrt{2}}(c_R|x-\rangle + e^{-i\Delta_e(t-t_c)}c_B|x+\rangle), \end{aligned} \quad (8.6)$$

where we have included the unitary evolution of the QD spin after the detection and renormalized the state vector. We see that upon coincident detector clicks, the state amplitudes of $|\psi_{input}\rangle$ are “teleported” onto the QD spin state. A challenge is that the optical frequencies and lifetime (pulse shape) of the input photon must be indistinguishable from the spin-entangled photon for this protocol to work since it relies on Hong-Ou-Mandel (H.O.M.) interference [21]. Since QD ensembles are inhomogeneously broadened, two randomly selected QDs would not be suitable for such a study. However in practice, it is not uncommon to find two QDs with nearly identical optical properties after moderate searching. The transitions can then be tuned exactly on resonance by applying external electric and magnetic fields.

In order to verify that the state transfer is successful, the input c 's are varied and the resulting QD spin state must be verified. To show that the state transfer is coherent, a $\pi/2$ spin rotation pulse can be applied to $|\psi_{QD}(t)\rangle$ at $t = t_r$ to map the coherence into a population. An important feature of the resulting state is that the dependence on the detection time (t_d) cancels out, and only the time difference $t_r - t_c$ between the rotation pulse and the “creation” of the input photon contributes to the signal. So that if the excitation pulse that creates the input photon is synchronized with the rotation pulse, an oscillation at the electron Zeeman frequency can

be observed by varying $t_r - t_c$, indicating that the state is coherent. Since the signal is not dependent on exact photon detection time, which limited the spin-photon entanglement fidelity, near unity teleportation fidelities should be realizable.

A challenge in this approach is that it requires three detection events for a success: two to herald the entanglement, and one to read out the spin state. So the success rate scales as η^3 , where η is the detection efficiency which is currently $\eta \approx 5 \times 10^{-5}$. In order to practically realize such an experiment, the detection efficiency must be improved to $\eta \approx 0.1\%$, so that given the experimental repetition rate of 76 MHz, the experimental success rate exceeds once per minute. Achieving a detection efficiency of $> 0.1\%$ has been realized by other groups studying InAs QD by using solid immersion lenses and weak optical cavities integrated with the sample structure to enhance the collection efficiency [61, 120]. Adopting such a design will facilitate the demonstration of quantum teleportation schemes and other multi-qubit quantum information applications.

8.2.2 Spin-Spin Entanglement

Intermediate spin-photon entangled states can also be used to mediate entanglement between two distant QD spins. The setup is depicted in Figures 8.2,8.3, where single photon detection events are used to herald entanglement between distant spins. The approach is not deterministic since it relies on postselection, but such protocols are capable of generating high fidelity entangled states which are useful for studying simple quantum networks. There are two protocols known as “type-I” and “type-II” entanglement, which are well known in the trapped ion community [19, 22, 121, 122]. In both protocols, the QDs are simultaneously excited with short laser pulses, and the spin-entangled photons from the two QDs are mixed on a 50-50 beam splitter before they are sent to a pair of single photon detectors. Detection events establish the spin-spin entanglement which can then be verified by using the techniques described in Chapter 7.

In the type-I protocol (Figure 8.2), the two QDs must be only weakly excited so

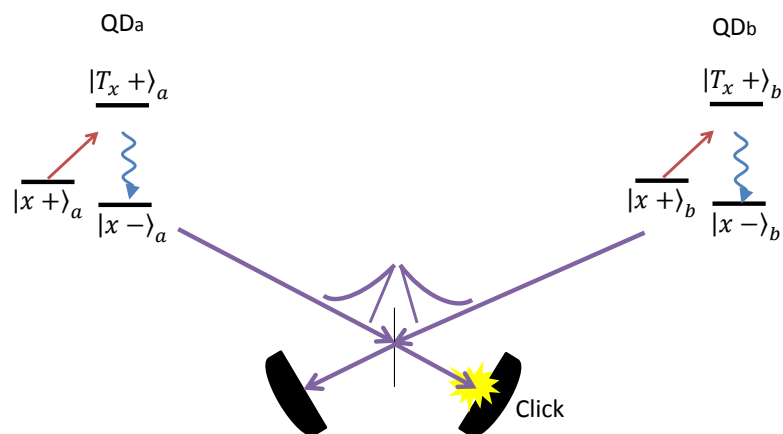


Figure 8.2: In a type-I protocol, the two QDs are weakly excited so that the probability of either being excited is much less than 1. If one detector registers a click, the QD spins are projected to an entangled state (Equation 8.7).

that the probability of either QD being excited (P_e) is much less than one. A single detection event in one of the detectors heralds the spin-spin entangled state of the form [122],

$$\langle \psi_{\text{photon}} | \Psi_{a,b} \rangle = \frac{1}{\sqrt{2}} (|x+\rangle_a |x-\rangle_b - e^{i\phi} |x-\rangle_a |x+\rangle_b). \quad (8.7)$$

where the phase ϕ is determined by the optical path difference between the two arms. This approach is challenging because it requires interferometric stability between the paths, but it has the advantage that the entanglement is heralded by a single detection event. This protocol has recently been used to establish entanglement between two trapped ions [123] and a similar protocol has been applied to spins associated with nitrogen vacancy centers in diamond [124].

Of course, since the protocol requires weak excitation to achieve high entanglement fidelities, there is a trade off between excitation probability and success rate. Given the current detection efficiency, and setting the excitation probability to $P_e \approx 0.01$, the experimental repetition rate of 76 MHz yields a spin-spin entanglement generation rate of $\approx 20 \text{ s}^{-1}$ [122]. In order to read out the both spin states to verify the

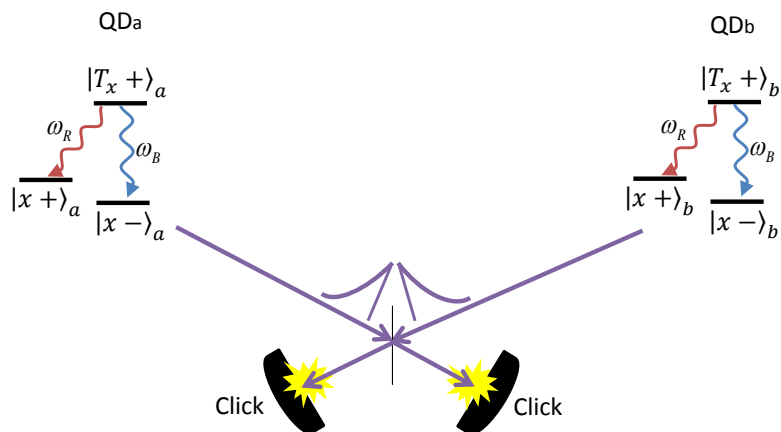


Figure 8.3: In a type-II protocol, both QDs are initialized to the $|T_x-\rangle$ state, which decay emitted two spin-entangled photons. Coincident detector clicks herald a spin-spin entangled state (Equation 8.8).

entanglement, two more spin readout photons must be detected so that the overall success rate for the experiment scales as $\eta^3 \times P_e$.

The type-II protocol (Figure 8.3), requires two simultaneous detection events to herald entanglement (described in Chapter 1 for ions), which similar to the teleportation protocol described in Section 8.2.1. The two QD are simultaneously excited, which then decay emitting spin-entangled photons. The photons are mixed on a 50-50 beam splitter, and coincident detector clicks heralds the spin-spin entangled state,

$$|\Psi\rangle_{a,b} = \frac{1}{\sqrt{2}} (|x+\rangle_a|x-\rangle_b - |x-\rangle_a|x+\rangle_b). \quad (8.8)$$

which does not have the optical path dependence of the type-I protocol. This experimental simplification is especially important in trapped ion experiments due to the challenge of spatially trapping ions below the Lamb-Dicke limit, which is why this was the first approach used to establish entanglement between two trapped ion qubits [5]. Another advantage of the approach is that the fidelity is not directly affected high excitation probability so both QDs can be fully excited. It is interesting to note that the frequency mismatch of the two decay channels, which limited the spin-photon

entanglement fidelity, is now a resource to enable high fidelity spin-spin entanglement fidelity. The sub-ns timing resolution required in the spin-photon entanglement experiment is not required as long as the photon wavepackets from the two QDs are sufficiently indistinguishable.

The downside of the approach is that the success rate for establishing entanglement scales as the detection efficiency squared since two photons must be detected. Given the current detection efficiency, this corresponds to a spin-spin entanglement generation of $\approx 3 \text{ min}^{-1}$ [122]. Again, to verify the spin-spin entanglement two more spin readout photons must be detected, so the total experimental success rate scales at η^4 for this protocol.

In both protocols, the entanglement generation and experimental success rates can be improved by increasing the collection efficiency so that the detection efficiency is $\eta \approx 0.1\%$ [61, 120]. However, since the spin-spin entanglement verification protocol goes as η^2 , both of these protocols would require many hours of data accumulation to acquire sufficient signal to noise. Another possibility is to integrate the QD with a strongly coupled optical cavity, where the decay into a specific cavity mode becomes a deterministic process, allowing for near unity collection efficiency.

A challenge associated with the single QD spin system is that the spin state readout that scatters a single photon is part of the optical pumping process which reinitializes the spin state. In many atomic systems, the ground state population is read out by scattering many photons off of a non-destructive “cycling” transition. A cycling transition is an effective two-level system whose excited state decays to a single ground state, which allows for a spin state population to be read out without destroying it. The single charged QD system does not have an accessible cycling transition; however, by moving to a QD molecule sample, a “W” system can be realized that is composed of a lambda system with two cycling transitions for each of the ground states [125](Figure 8.4).

Using a cycling transition to read out the spin state can dramatically increase the success rate of an experiment because many photons can be scattered to read out the final spin state population. So that in a heralded spin-spin entanglement

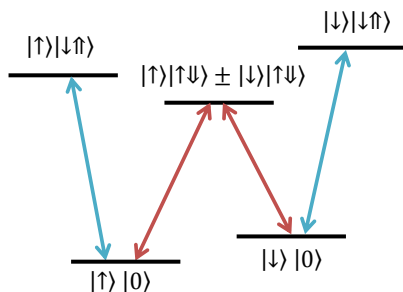


Figure 8.4: By moving to a QD molecule system a W system can be formed, which is composed of a central lambda system (red) and two cycling transitions (blue) which can provide a nondestructive readout of the spin populations. The kets label the spin configurations of the lower and upper QDs which form the molecule.

protocol, once the entanglement is established, a spin readout protocol is initialized by turning on a long laser pulse resonant with one of the cycling transitions. The number of fluorescence photons detected during the readout pulse can be compared to a threshold level to determine the spin state population. For example, given that the current detection efficiency is $\eta \approx 5 \times 10^{-5}$, and that the QD scatters $\approx 10^9$ photons per second, the average wait time to detect a single photon is $20 \mu\text{s}$, so that many photons can contribute to the spin readout signal without slowing down the experimental success rate, which is then limited only by the spin-spin entanglement generation rate.

8.3 Chapter Summary

In this Chapter, the primary results of this thesis have been summarized, and a few of the possible future directions have been analyzed. Specifically, applications of the spin-photon entangled state are considered as they relate to scaling the QD spin system. We analyze the feasibility of demonstrating quantum teleportation between a photon state and the QD spin state and entanglement of distant QD spins using

intermediate spin-photon entangled states. In addition to scaling the QD spin system with spin-photon entangled states, other quantum information applications such as hybrid entanglement between QDs and trapped ions [126], and QDs operating at different optical frequencies can in principle be realized [3]. In such hybrid protocols, it has been proposed that the optically driven QD spin qubit can be used for its fast information processing since the system is compatible with fast gate times, and the trapped ion interface could serve as a long lived quantum memory. Intermediate spin-photon entangled states play a crucial role as a quantum communication channel which can connect disparate quantum systems to realize many exciting quantum information applications.

BIBLIOGRAPHY

BIBLIOGRAPHY

- [1] Xiaodong Xu, Yanwen Wu, Bo Sun, Qiong Huang, Jun Cheng, D.G. Steel, AS Bracker, D Gammon, C Emary, and LJ Sham. Fast spin state initialization in a singly charged InAs-GaAs quantum dot by optical cooling. *Physical Review Letters*, 99(9):097401, 2007.
- [2] David Press, Thaddeus D. Ladd, Bingyang Zhang, and Yoshihisa Yamamoto. Complete quantum control of a single quantum dot spin using ultrafast optical pulses. *Nature*, 456(7219):218–221, 2008.
- [3] A. Imamoglu, D. D. Awschalom, G. Burkard, D. P. DiVincenzo, D. Loss, M. Sherwin, and A. Small. Quantum information processing using quantum dot spins and cavity QED. *Physical Review Letters*, 83:4204–4207, 1999.
- [4] Wang Yao, Ren-Bao Liu, and L. J. Sham. Theory of control of the spin-photon interface for quantum networks. *Physical Review Letters*, 95:030504, 2005.
- [5] D. L. Moehring, P. Maunz, S. Olmschenk, K. C. Younge, D. N. Matsukevich, L.-M. Duan, and C. Monroe. Entanglement of single-atom quantum bits at a distance. *Nature*, 449(7158):68–71, 2007.
- [6] T. H. Maiman. Stimulated optical radiation in ruby. *Nature*, 187(4736):493–494, 1960.
- [7] P. A. Franken, A. E. Hill, C. W. Peters, and G. Weinreich. Generation of optical harmonics. *Physical Review Letters*, 7:118–119, 1961.
- [8] W. Neuhauser, M. Hohenstatt, P. E. Toschek, and H. Dehmelt. Localized visible Ba⁺ mono-ion oscillator. *Physical Review A*, 22:1137–1140, 1980.
- [9] D.J. Wineland and Wayne M. Itano. Spectroscopy of a single Mg⁺ ion. *Physics Letters A*, 82(2):75 – 78, 1981.
- [10] R. P. Feynman. Quantum mechanical computers. *Foundations of Physics*, 16(6):507–531, 1986.
- [11] David Deutsch. Quantum theory, the Church-Turing principle and the universal quantum computer. *Proceedings of the Royal Society of London. A. Mathematical and Physical Sciences*, 400(1818):97–117, 1985.
- [12] Lov K. Grover. A fast quantum mechanical algorithm for database search. In *Proceedings of the twenty-eighth annual ACM symposium on Theory of computing*, pages 212–219. ACM, 1996.

- [13] P. W. Shor. Polynomial-time algorithms for prime factorization and discrete logarithms on a quantum computer. *SIAM journal on computing*, 26(5):1484–1509, 1997.
- [14] Charles H. Bennett, David P. DiVincenzo, John A. Smolin, and William K. Wootters. Mixed-state entanglement and quantum error correction. *Physical Review A*, 54(5):3824, 1996.
- [15] Peter W. Shor. Fault-tolerant quantum computation. In *Foundations of Computer Science, 1996. Proceedings., 37th Annual Symposium on*, pages 56–65. IEEE, 1996.
- [16] Michael A. Nielsen and Isaac L. Chuang. *Quantum computation and quantum information*. Cambridge University Press, 2010.
- [17] Juan Ignacio Cirac and Peter Zoller. A scalable quantum computer with ions in an array of microtraps. *Nature*, 404(6778):579–581, 2000.
- [18] Margareta Wallquist, Klemens Hammerer, Peter Rabl, Mikhail Lukin, and Peter Zoller. Hybrid quantum devices and quantum engineering. *Physica Scripta*, 2009(T137):014001, 2009.
- [19] C. Cabrillo, J.I. Cirac, P. Garcia-Fernandez, and P. Zoller. Creation of entangled states of distant atoms by interference. *Physical Review A*, 59(2):1025, 1999.
- [20] B. B. Blinov, D. L. Moehring, L.-M. Duan, and C. Monroe. Observation of entanglement between a single trapped atom and a single photon. *Nature*, 428(6979):153–157, 2004.
- [21] C. K. Hong, Z. Y. Ou, and L. Mandel. Measurement of subpicosecond time intervals between two photons by interference. *Physical Review Letters*, 59(18):2044, 1987.
- [22] Christoph Simon and William T. M. Irvine. Robust long-distance entanglement and a loophole-free bell test with ions and photons. *Physical Review Letters*, 91:110405, 2003.
- [23] A.Y. Cho and J.R. Arthur. Molecular beam epitaxy. *Progress in Solid State Chemistry*, 10, Part 3(0):157 – 191, 1975.
- [24] Daniel Loss and David P. DiVincenzo. Quantum computation with quantum dots. *Physical Review A*, 57(1):120, 1998.
- [25] J.R. Petta, A.C. Johnson, J.M. Taylor, E.A. Laird, A. Yacoby, M.D. Lukin, C.M. Marcus, M.P. Hanson, and A.C. Gossard. Coherent manipulation of coupled electron spins in semiconductor quantum dots. *Science*, 309(5744):2180–2184, 2005.

- [26] Daniel Gammon and Duncan G. Steel. Optical studies of single quantum dots. *Physics Today*, 55:36, 2002.
- [27] T.H. Stievater, Xiaoqin Li, D. Gammon Steel, D. Gammon, D.S. Katzer, D. Park, C. Piermarocchi, and L.J. Sham. Rabi oscillations of excitons in single quantum dots. *Physical Review Letters*, 87(13):133603, 2001.
- [28] Gang Chen, N.H. Bonadeo, D.G. Steel, D. Gammon, D.S. Katzer, D. Park, and L.J. Sham. Optically induced entanglement of excitons in a single quantum dot. *Science*, 289(5486):1906–1909, 2000.
- [29] Xiaoqin Li, Yanwen Wu, Duncan Steel, D. Gammon, T.H. Stievater, D.S. Katzer, D. Park, C. Piermarocchi, and L.J. Sham. An all-optical quantum gate in a semiconductor quantum dot. *Science*, 301(5634):809–811, 2003.
- [30] J. Berezovsky, M.H. Mikkelsen, N.G. Stoltz, L.A. Coldren, and D.D. Awschalom. Picosecond coherent optical manipulation of a single electron spin in a quantum dot. *Science*, 320(5874):349–352, 2008.
- [31] Yanwen Wu, Erik D. Kim, Xiaodong Xu, Jun Cheng, D.G. Steel, A.S. Bracker, D. Gammon, Sophia E Economou, and LJ Sham. Selective optical control of electron spin coherence in singly charged GaAs-Al_{0.3}Ga_{0.7}As quantum dots. *Physical Review Letters*, 99(9):097402, 2007.
- [32] Tomonori Ishikawa, Tetsuya Nishimura, Shigeru Kohmoto, and Kiyoshi Asakawa. Site-controlled InAs single quantum-dot structures on GaAs surfaces patterned by in situ electron-beam lithography. *Applied Physics Letters*, 76(2):167–169, 2000.
- [33] M. Mehta, D. Reuter, A. Melnikov, A.D. Wieck, and A. Remhof. Focused ion beam implantation induced site-selective growth of InAs quantum dots. *Applied Physics Letters*, 91(12):123108–123108, 2007.
- [34] Michael Scheibner, Allan S. Bracker, Danny Kim, and Daniel Gammon. Essential concepts in the optical properties of quantum dot molecules. *Solid State Communications*, 149(35):1427–1435, 2009.
- [35] Danny Kim, Samuel G. Carter, Alex Greulich, Allan S. Bracker, and Daniel Gammon. Ultrafast optical control of entanglement between two quantum-dot spins. *Nature Physics*, 7(3):223–229, 2010.
- [36] Tomoyuki Yoshie, Axel Scherer, J. Hendrickson, G. Khitrova, H.M. Gibbs, G. Rupper, C. Ell, O.B. Shchekin, and D.G. Deppe. Vacuum rabi splitting with a single quantum dot in a photonic crystal nanocavity. *Nature*, 432(7014):200–203, 2004.
- [37] G. Seogon J.P. Reithmaier, A. Löffler, C. Hofmann, S. Kuhn, S. Reitzenstein, L.V. Keldysh, V.D. Kulakovskii, and A. Forchel T.L. Reinecke. Strong

- coupling in a single quantum dot-semiconductor microcavity system. *Nature*, 432(7014):197–200, 2004.
- [38] Dirk Englund, Andrei Faraon, Ilya Fushman, Nick Stoltz, and Jelena Vučković & Pierre Petroff. Controlling cavity reflectivity with a single quantum dot. *Nature*, 450(7171):857–861, 2007.
- [39] J.I. Cirac, Peter Zoller, H.J. Kimble, and H. Mabuchi. Quantum state transfer and entanglement distribution among distant nodes in a quantum network. *Physical Review Letters*, 78(16):3221–3224, 1997.
- [40] H.J. Kimble. The quantum internet. *Nature*, 453(7198):1023–1030, 2008.
- [41] Samuel G. Carter, Timothy M. Sweeney, Mijin Kim, Chul Soo Kim, Dmitry Solenov, Sophia E. Economou, Thomas L. Reinecke, Lily Yang, Allan S. Bracker, and Daniel Gammon. Quantum control of a spin qubit coupled to a photonic crystal cavity. *Nature Photonics*, 7(4):329–334, 2013.
- [42] Sophia E. Economou, Ren-Bao Liu, L.J. Sham, and D.G. Steel. Unified theory of consequences of spontaneous emission in a λ system. *Physical Review B*, 71(19):195327, 2005.
- [43] J. R. Schaibley, A. P. Burgers, G. A. McCracken, L.-M. Duan, P. R. Berman, D. G. Steel, A. S. Bracker, D. Gammon, and L. J. Sham. Demonstration of quantum entanglement between a single electron spin confined to an InAs quantum dot and a photon. *Physical Review Letters*, 110:167401, 2013.
- [44] R. N. Hall, G. E. Fenner, J. D. Kingsley, T. J. Soltys, and R. O. Carlson. Coherent light emission from GaAs junctions. *Physical Review Letters*, 9:366–368, 1962.
- [45] Nick Holonyak and S.F. Bevacqua. Coherent (visible) light emission from Ga (As- P) junctions. *Applied Physics Letters*, 1(4):82–83, 1962.
- [46] Jasprit Singh. *Electronic and optoelectronic properties of semiconductor structures*. Cambridge University Press, 2003.
- [47] Dieter Bimberg, Marius Grundmann, Nikolai N Ledentsov, et al. *Quantum dot heterostructures*, volume 471973882. John Wiley Chichester, 1999.
- [48] D.L. Huffaker, G. Park, Z. Zou, O.B. Shchekin, and D.G. Deppe. 1.3 μm room-temperature GaAs-based quantum-dot laser. *Applied Physics Letters*, 73(18):2564–2566, 1998.
- [49] A.J. Nozik. Quantum dot solar cells. *Physica E: Low-dimensional Systems and Nanostructures*, 14(1):115–120, 2002.
- [50] Neil W. Ashcroft and N. David Mermin. Solid state physics. *Saunders College, Philadelphia*, 1, 1976.

- [51] J. C. Slater and G. F. Koster. Simplified lcao method for the periodic potential problem. *Physical Review*, 94:1498–1524, 1954.
- [52] J.M. Luttinger and W. Kohn. Motion of electrons and holes in perturbed periodic fields. *Physical Review*, 97(4):869, 1955.
- [53] Huaxiang Fu, Lin-Wang Wang, and Alex Zunger. Excitonic exchange splitting in bulk semiconductors. *Physical Review B*, 59:5568–5574, 1999.
- [54] L. R. C. Fonseca, J. L. Jimenez, J. P. Leburton, and Richard M. Martin. Self-consistent calculation of the electronic structure and electron-electron interaction in self-assembled InAs-GaAs quantum dot structures. *Physical Review B*, 57:4017–4026, 1998.
- [55] O. Stier, M. Grundmann, and D. Bimberg. Electronic and optical properties of strained quantum dots modeled by 8-band k·p theory. *Physical Review B*, 59:5688–5701, 1999.
- [56] Alberto Franceschetti and Alex Zunger. Pseudopotential calculations of electron and hole addition spectra of InAs, InP, and Si quantum dots. *Physical Review B*, 62:2614–2623, 2000.
- [57] Z.R. Wasilewski, S. Fafard, and J.P. McCaffrey. Size and shape engineering of vertically stacked self-assembled quantum dots. *Journal of crystal growth*, 201:1131–1135, 1999.
- [58] R. J. Warburton, C. Schafflein, D. Haft, F. Bickel, A. Lorke, K. Karrai, J. M. Garcia, W. Schoenfeld, and P. M. Petroff. Optical emission from a charge-tunable quantum ring. *Nature*, 405(6789):926–929, 2000.
- [59] Xiaodong Xu. *Coherent Optical Spectroscopy of a Single Semi-Conductor Quantum Dot*. Doctoral thesis, University of Michigan, 2008.
- [60] E. Togan, Y. Chu, A. S. Trifonov, L. Jiang, J. Maze, L. Childress, M. V. G. Dutt, A. S. Sorensen, P. R. Hemmer, A. S. Zibrov, and M. D. Lukin. Quantum entanglement between an optical photon and a solid-state spin qubit. *Nature*, 466(7307):730–734, 2010.
- [61] W.B. Gao, Parisa Fallahi, Emre Togan, Javier Miguel-Sanchez, and Atac Imamoglu. Observation of entanglement between a quantum dot spin and a single photon. *Nature*, 491(7424):426–430, 2012.
- [62] Kristiaan De Greve, Leo Yu, Peter L. McMahon, Jason S. Pelc, Chandra M. Natarajan, Na Young Kim, Eisuke Abe, Sebastian Maier, Christian Schneider, Martin Kamp, Sven Höfling, Robert H. Hadfield, Alfred Forchel, M. M. Fejer, and Yoshihisa Yamamoto. Quantum-dot spin-photon entanglement via frequency downconversion to telecom wavelength. *Nature*, 491(7424):421–425, 2012.

- [63] B. R. Mollow. Power spectrum of light scattered by two-level systems. *Physical Review*, 188:1969–1975, 1969.
- [64] H. J. Kimble and L. Mandel. Theory of resonance fluorescence. *Physical Review A*, 13(6):2123–2144, 1976.
- [65] A. Muller, E. B. Flagg, P. Bianucci, X. Y. Wang, D. G. Deppe, W. Ma, J. Zhang, G. J. Salamo, M. Xiao, and C. K. Shih. Resonance fluorescence from a coherently driven semiconductor quantum dot in a cavity. *Physical Review Letters*, 99:187402, 2007.
- [66] E. B. Flagg, A. Muller, J. W. Robertson, S. Founta, D. G. Deppe, M. Xiao, W. Ma, G. J. Salamo, and C. K. Shih. Resonantly driven coherent oscillations in a solid-state quantum emitter. *Nature Phys.*, 5(3):203–207, 2009.
- [67] Clemens Matthiesen, Anthony Nickolas Vamivakas, and Mete Atatüre. Sub-natural linewidth single photons from a quantum dot. *Physical Review Letters*, 108(9):093602, 2012.
- [68] P.R. Berman and V. S. Malinovsky. *Principles of Laser Spectroscopy and Quantum Optics*. Princeton University Press, 2011.
- [69] W. Heitler. *The Quantum Theory of Radiation*. Oxford University Press, 1944.
- [70] R. Loudon. *The Quantum Theory of Light*. Oxford University Press, 1983.
- [71] M.O. Scully and M.S. Zubairy. *Quantum Optics*. Cambridge University Press, 1997.
- [72] Benito Alen, Florian Bickel, Khaled Karrai, Richard J. Warburton, and Pierre M. Petroff. Stark-shift modulation absorption spectroscopy of single quantum dots. *Appl. Phys. Lett.*, 83:2235, 2003.
- [73] Erik Kim. *The Coherent Optical Spectroscopy and Control of an Electron Spin in a Self-Assembled Quantum Dot for Quantum Computing*. Doctoral thesis, University of Michigan, 2009.
- [74] S. J. van Enk and H. J. Kimble. Strongly focused light beams interacting with single atoms in free space. *Physical Review A*, 63:023809, 2001.
- [75] M. Kroner, A. O. Govorov, S. Remi, B. Biedermann, S. Seidl, A. Badolato, P. M. Petroff, W. Zhang, R. Barbour, B. D. Gerardot, R. J. Warburton, and K. Karrai. The nonlinear fano effect. *Nature*, 451(7176):311–314, 2008.
- [76] Benito Alen, Alexander Hagele, Martin Kroner, Stefan Seidl, Khaled Karrai, Richard J. Warburton, Antonio Badolato, Gilberto Medeiros-Ribeiro, and Pierre M. Petroff. Absorptive and dispersive optical responses of excitons in a single quantum dot. *Applied Physics Letters*, 89(12):123124–123124–3, 2006.

- [77] P. Higdon, R. Juskaitytis, and T. Wilson. The effect of detector size on the extinction coefficient in confocal polarization microscopes. *Journal of Microscopy*, 187(1):8–11, 1997.
- [78] Michael Shribak, Shinya Inoue, and Rudolf Oldenbourg. Polarization aberrations caused by differential transmission and phase shift in high-numerical-aperture lenses: theory, measurement, and rectification. *Optical Engineering*, 41(5):943–954, 2002.
- [79] L.M. Bollinger and G. E. Thomas. Measurement of the time dependence of scintillation intensity by a delayed-coincidence method. *Review of Scientific Instruments*, 32(9):1044–1050, 1961.
- [80] Desmond O’Connor. *Time-correlated single photon counting*. Academic Press, 1984.
- [81] Robert H. Hadfield. Single-photon detectors for optical quantum information applications. *Nature Photonics*, 3(12):696–705, 2009.
- [82] B.E. Kardynalstrok and A.J. Z.L. Yuan. An avalanche photodiode-based photon-number-resolving detector. *Nature Photonics*, 2(7):425–428, 2008.
- [83] Michael Wahl, Hans-Jurgen Rahn, Tino Rohlicke, Gerald Kell, Daniel Nettels, Frank Hillger, Ben Schuler, and Rainer Erdmann. Scalable time-correlated photon counting system with multiple independent input channels. *Review of Scientific Instruments*, 79(12):123113–123113, 2008.
- [84] C.E. Rogers III, J.L. Carini, J.A. Pechkis, and P.L. Gould. Characterization and compensation of the residual chirp in a mach-zehnder-type electro-optical intensity modulator. *Optics express*, 18(2):1166–1176, 2010.
- [85] Erik D. Kim, Katherine Truex, Yanwen Wu, A. Amo, Xiaodong Xu, D.G. Steel, A.S. Bracker, D. Gammon, and L.J. Sham. Picosecond optical spectroscopy of a single negatively charged self-assembled InAs quantum dot. *Applied Physics Letters*, 97(11):113110–113110, 2010.
- [86] L. Allen and J. H. Eberly. *Optical Resonance and Two-Level Atoms*. Wiley, 1975.
- [87] Andreas Muller, Edward B. Flagg, Pablo Bianucci, X.Y. Wang, Dennis G. Deppe, Wenquan Ma, Jiayu Zhang, G.J. Salamo, Min Xiao, and Chih-Kang Shih. Resonance fluorescence from a coherently driven semiconductor quantum dot in a cavity. *Physical Review Letters*, 99(18):187402, 2007.
- [88] J.R. Schaibley, A.P. Burgers, G.A. McCracken, D.G. Steel, A.S. Bracker, D. Gammon, and L.J. Sham. Direct detection of time-resolved rabi oscillations in a single quantum dot via resonance fluorescence. *Physical Review B*, 87(11):115311, 2013.

- [89] H. C. Torrey. Transient nutations in nuclear magnetic resonance. *Physical Review*, 76:1059–1068, 1949.
- [90] P.C. Hansen. Regularization tools version 4.0 for Matlab 7.3. *Numerical Algorithms*, 46:189–194, 2007.
- [91] Xiaodong Xu, Wang Yao, Bo Sun, Duncan G. Steel, Allan S. Bracker, Daniel Gammon, and L.J. Sham. Optically controlled locking of the nuclear field via coherent dark-state spectroscopy. *Nature*, 459(7250):1105–1109, 2009.
- [92] Bo Sun, Colin Ming Earn Chow, Duncan G Steel, Allan S. Bracker, Daniel Gammon, and L.J. Sham. Persistent narrowing of nuclear-spin fluctuations in InAs quantum dots using laser excitation. *Physical Review Letters*, 108(18):187401, 2012.
- [93] Alexander Högele, Stefan Seidl, Martin Kroner, Khaled Karrai, Richard J. Warburton, Brian D. Gerardot, and Pierre M. Petroff. Voltage-controlled optics of a quantum dot. *Physical Review Letters*, 93(21):217401, 2004.
- [94] W. Langbein, P. Borri, U. Woggon, V. Stavarache, D. Reuter, and A. D. Wieck. Radiatively limited dephasing in InAs quantum dots. *Physical Review B*, 70:033301, 2004.
- [95] Xiaodong Xu, Bo Sun, Erik D. Kim, Katherine Smirl, P. R. Berman, D. G. Steel, A. S. Bracker, D. Gammon, and L. J. Sham. Single charged quantum dot in a strong optical field: Absorption, gain, and the ac-stark effect. *Physical Review Letters*, 101:227401, 2008.
- [96] H.J. Kimble, M. Dagenais, and L. Mandel. Photon antibunching in resonance fluorescence. *Physical Review Letters*, 39(11):691–695, 1977.
- [97] B. Lounis, H.A. Bechtel, D. Gerion, P. Alivisatos, and W.E. Moerner. Photon antibunching in single cdse/zns quantum dot fluorescence. *Chemical Physics Letters*, 329(5):399–404, 2000.
- [98] P. Michler, A. Kiraz, C. Becher, W.V. Schoenfeld, P.M. Petroff, Lidong Zhang, E. Hu, and A. Imamoglu. A quantum dot single-photon turnstile device. *Science*, 290(5500):2282–2285, 2000.
- [99] Charles Santori, Matthew Pelton, Glenn Solomon, Yseulte Dale, and Yoshihisa Yamamoto. Triggered single photons from a quantum dot. *Physical Review Letters*, 86(8):1502–1505, 2001.
- [100] Zhiliang Yuan, Beata E Kardynal, R. Mark Stevenson, Andrew J. Shields, Charlene J. Lobo, Ken Cooper, Neil S. Beattie, David A. Ritchie, and Michael Pepper. Electrically driven single-photon source. *Science*, 295(5552):102–105, 2002.

- [101] Aaron J. Miller, Sae Woo Nam, John M. Martinis, and Alexander V. Sergienko. Demonstration of a low-noise near-infrared photon counter with multiphoton discrimination. *Applied Physics Letters*, 83(4):791–793, 2003.
- [102] Xiaolong Hu, Tian Zhong, James E White, Eric A. Dauler, Faraz Najafi, Charles H. Herder, Franco N.C. Wong, and Karl K. Berggren. Fiber-coupled nanowire photon counter at 1550 nm with 24% system detection efficiency. *Optics letters*, 34(23):3607–3609, 2009.
- [103] R. Hanbury Brown and R.Q. Twiss. Correlation between photons in two coherent beams of light. *Nature*, 177(4497):27–29, 1956.
- [104] Xiaodong Xu, Yanwen Wu, Bo Sun, Qiong Huang, Jun Cheng, D. G. Steel, A. S. Bracker, D. Gammon, C. Emary, and L. J. Sham. Fast spin state initialization in a singly charged InAs-GaAs quantum dot by optical cooling. *Physical Review Letters*, 99:097401, 2007.
- [105] Erik D. Kim, Katherine Truex, Xiaodong Xu, Bo Sun, D. G. Steel, A. S. Bracker, D. Gammon, and L. J. Sham. Fast spin rotations by optically controlled geometric phases in a charge-tunable InAs quantum dot. *Physical Review Letters*, 104:167401, 2010.
- [106] D.N. Krizhanovskii, A. Ebbens, A.I. Tartakovskii, F. Pulizzi, T. Wright, M.S. Skolnick, and M. Hopkinson. Individual neutral and charged $\text{In}_x\text{Ga}_{1-x}\text{As}$ – GaAs quantum dots with strong in-plane optical anisotropy. *Physical Review B*, 72(16):161312, 2005.
- [107] Katherine Truex. *Optical Coherent Control of a Single Charged Indium Arsenide Quantum Dot*. Doctoral thesis, University of Michigan, 2011.
- [108] David Press, Kristiaan De Greve, Peter L. McMahon, Thaddeus D. Ladd, Benedikt Friess, Christian Schneider, Martin Kamp, Sven Höfling, Alfred Forchel, and Yoshihisa Yamamoto. Ultrafast optical spin echo in a single quantum dot. *Nature Photonics*, 4(6):367–370, 2010.
- [109] William Happer. Optical pumping. *Reviews of Modern Physics*, 44:169–249, 1972.
- [110] Mete Atatüre, Jan Dreiser, Antonio Badolato, Alexander Högele, Khaled Karrai, and Atac Imamoglu. Quantum-dot spin-state preparation with near-unity fidelity. *Science*, 312(5773):551–553, 2006.
- [111] Martin Kroner, Kathrina M. Weiss, Benjamin Biedermann, Stefan Seidl, Stephan Manus, Alexander W. Holleitner, Antonio Badolato, Pierre M. Petroff, Brian D. Gerardot, and Richard J. Warburton. Optical detection of single-electron spin resonance in a quantum dot. *Physical Review Letters*, 100(15):156803, 2008.

- [112] Pochung Chen, C. Piermarocchi, L. J. Sham, D. Gammon, and D. G. Steel. Theory of quantum optical control of a single spin in a quantum dot. *Physical Review B*, 69:075320, 2004.
- [113] C. Emary and L.J. Sham. Optically controlled single-qubit rotations in self-assembled InAs quantum dots. *Journal of Physics: Condensed Matter*, 19(5):056203, 2007.
- [114] Norman F. Ramsey. A molecular beam resonance method with separated oscillating fields. *Physical Review*, 78(6):695, 1950.
- [115] Thaddeus D. Ladd, David Press, Kristiaan De Greve, Peter L. McMahon, Benedikt Friess, Christian Schneider, Martin Kamp, Sven Höfling, Alfred Forchel, and Yoshihisa Yamamoto. Pulsed nuclear pumping and spin diffusion in a single charged quantum dot. *Physical Review Letters*, 105:107401, 2010.
- [116] Von V Weisskopf and EZ Wigner. Berechnung der natürlichen linienbreite auf grund der diracschen lichttheorie. *Zeitschrift für Physik*, 63(1-2):54–73, 1930.
- [117] J.R. Schaibley and P.R. Berman. The effect of frequency-mismatched spontaneous emission on atom-field entanglement. *Journal of Physics B: Atomic, Molecular and Optical Physics*, 45(12):124020, 2012.
- [118] Marlan O. Scully and Kai Drühl. Quantum eraser: A proposed photon correlation experiment concerning observation and delayed choice in quantum mechanics. *Physical Review A*, 25(4):2208–2213, 1982.
- [119] Xiaodong Xu, Bo Sun, Paul R Berman, Duncan G. Steel, Allan S. Bracker, Dan Gammon, and Lu J. Sham. Coherent optical spectroscopy of a strongly driven quantum dot. *Science*, 317(5840):929–932, 2007.
- [120] A.N. Vamivakas, C.-Y. Lu, C. Matthiesen, Y. Zhao, S. Fält, A. Badolato, and M. Atatüre. Observation of spin-dependent quantum jumps via quantum dot resonance fluorescence. *Nature*, 467(7313):297–300, 2010.
- [121] L.-M. Duan and H.J. Kimble. Efficient engineering of multiatom entanglement through single-photon detections. *Physical Review Letters*, 90(25):253601, 2003.
- [122] L.-M. Duan, B.B. Blinov, D.L. Moehring, and C. Monroe. Scalable trapped ion quantum computation with a probabilistic ion-photon mapping. *Quantum Information and Computation*, 4(3):165–173, 2004.
- [123] L. Slodička, G. Hétet, N. Röck, P. Schindler, M. Hennrich, and R. Blatt. Atom-atom entanglement by single-photon detection. *Physical Review Letters*, 110:083603, 2013.

- [124] H. Bernien, B. Hensen, W. Pfaff, G. Koolstra, M.S. Blok, L. Robledo, T.H. Taminiau, M. Markham, D.J. Twitchen, and L. Childress. Heralded entanglement between solid-state qubits separated by three metres. *Nature*, 497(7447):86–90, 2013.
- [125] Danny Kim, Sophia E Economou, Ștefan C Bădescu, Michael Scheibner, Allan S Bracker, Mark Bashkansky, Thomas L Reinecke, and Daniel Gammon. Optical spin initialization and nondestructive measurement in a quantum dot molecule. *Physical Review Letters*, 101(23):236804, 2008.
- [126] Edo Waks and Christopher Monroe. Protocol for hybrid entanglement between a trapped atom and a quantum dot. *Physical Review A*, 80(6):062330, 2009.